



CREEP PERFORMANCE OF OXIDE CERAMIC FIBER MATERIALS AT
ELEVATED TEMPERATURE IN AIR AND IN STEAM

DISSERTATION

Clinton J. Armani, Major, USAF

AFIT/DS/ENY/11-02

DEPARTMENT OF THE AIR FORCE
AIR UNIVERSITY

Air Force Institute of Technology

Wright-Patterson Air Force Base, Ohio

APPROVED FOR PUBLIC RELEASE; DISTRIBUTION UNLIMITED

The views expressed in this dissertation are those of the author and do not reflect the official policy or position of the United States Air Force, the Department of Defense, or the United States Government. This material is declared a work of the United States Government and is not subject to copyright protection in the United States.

AFIT/DS/ENY/11-02

CREEP PERFORMANCE OF OXIDE CERAMIC FIBER MATERIALS AT
ELEVATED TEMPERATURE IN AIR AND IN STEAM

DISSERTATION

Presented to the Faculty

Graduate School of Engineering and Management

Air Force Institute of Technology

Air University

Air Education and Training Command

In Partial Fulfillment of the Requirements for the

Degree of Doctor of Philosophy

Clinton J. Armani, BS, MS

Major, USAF


March 2011


APPROVED FOR PUBLIC RELEASE; DISTRIBUTION UNLIMITED


CREEP PERFORMANCE OF OXIDE CERAMIC FIBER MATERIALS AT
ELEVATED TEMPERATURE IN AIR AND IN STEAM

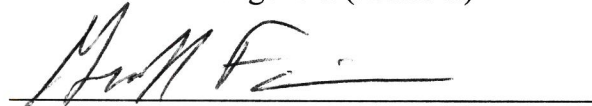
Clinton J. Armani, BS, MS
Major, USAF

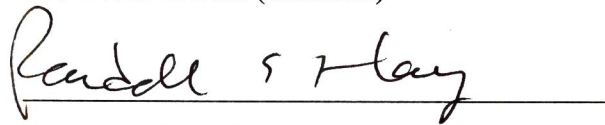
Approved:


Dr. Marina B. Ruggles-Wrenn (Chairman) 07 MAR 2011
Date

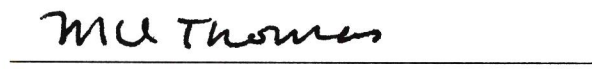

Dr. Jonathan T. Black (Member) 04 MAR 2011
Date


Dr. Robert L. Hengehold (Member) 04 Mar 2011
Date


Dr. Geoff E. Fair (Member) 04 MAR 2011
Date


Dr. Randall S. Hay (Member) 06 Mar 2011
Date

Accepted:


Dr. M. U. Thomas 14 Mar 2011
Date
Dean, Graduate School of
Engineering and Management

Abstract

Structural aerospace components that operate in severe conditions, such as extreme temperatures and detrimental environments, require structural materials that have superior long-term mechanical properties and that are thermochemically stable over a broad range of service temperatures and environments. Ceramic matrix composites (CMCs) capable of excellent mechanical performance in harsh environments are prime candidates for such applications. Oxide ceramic materials have been used as constituents in CMCs. However, recent studies have shown that high-temperature mechanical performance of oxide-oxide CMCs deteriorate in a steam-rich environment. The degradation of strength at elevated temperature in steam has been attributed to the environmentally assisted subcritical crack growth in the oxide fibers. Furthermore, oxide-oxide CMCs have shown significant increases in steady-state creep rates in steam. The present research investigated the effects of steam on the high-temperature creep and monotonic tension performance of several oxide ceramic materials. Experimental facilities were designed and configured, and experimental methods were developed to explore the influence of steam on the mechanical behaviors of ceramic fiber tows and of ceramic bulk materials under temperatures in the 1100-1300°C range.

The effects of steam on creep behavior of NextelTM 610 and NextelTM 720 fiber tows were examined. Creep rates at elevated temperatures in air and in steam were obtained for both types of fibers. Relationships between creep rates and applied stresses were modeled and underlying creep mechanisms were identified. For both types of fiber tows,

a creep life prediction analysis was performed using linear elastic fracture mechanics and a power-law crack velocity model. These results have not been previously reported and have critical design implications for CMC components operating in steam or near the recommended design limits. Predictions were assessed and validated via comparisons with experimental results. Additionally, the utility of the Monkman-Grant relationship to predicting creep-rupture life of the fiber tows at elevated temperature in air and in steam was demonstrated.

Furthermore, the effects of steam on the compressive creep performance of bulk ceramic materials were also studied. Performance of fine grained, polycrystalline alumina (Al_2O_3) was investigated at 1100 and 1300°C in air and in steam. To evaluate the effect of silica doping during material processing both undoped and silica doped polycrystalline alumina specimens were tested. Finally, compressive creep performance of yttrium aluminum garnet (YAG, $\text{Y}_3\text{Al}_5\text{O}_{12}$) was evaluated at 1300°C in air and in steam. Both undoped and silica doped YAG specimens were included in the study. YAG is being considered as the next-generation oxide fiber material. However, before considerable funding and effort are invested in a fiber development program, it is necessary to evaluate the creep performance of YAG at elevated temperature in steam. Results of this research demonstrated that both the undoped YAG and the silica doped YAG exhibited exceptional creep resistance at 1300°C in steam for grain sizes $\sim 1\text{ }\mu\text{m}$. These results supplement the other promising features of YAG that make it a strong candidate material for the next generation ceramic fiber.

AFIT/DS/ENY/11-02

In memory of my Father

Acknowledgements

For as long as I can recall, I have enjoyed learning how things work. This inquisitiveness led me to pursue engineering studies. Through science and engineering, I have been amazed time and again by God's great design. The beauty, fascination and mystery are delightful. I often say that I've been lured by infinity. Therefore, my first recognition is to God, for the entire world bears witness to his divine attributes.

This work would certainly not have been possible without a collaborative effort. My research committee has consistently provided positive guidance and supportive feedback. My advisor has been a genuine mentor. From academic coursework to research supervision, she has been a leader worthy of following. To the AFRL ceramics group, thank you for your sponsorship and assistance in this work. May these results further equip you in providing superb solutions to challenging problems.

I also acknowledge the AFIT machinists, lab support staff, fellow students, and faculty. AFIT is an excellent school with rich Air Force heritage. May we not forget that we are fighting wars on the technological forefront in order to employ this knowledge in defense of and service to our nation. Keep up the good work.

Family has been a stabilizing factor throughout my life. My parents have provided years of support and encouragement. From the beginning of our relationship, my wife has been my best friend. She completes me in many ways, works harder than anyone that I know and is unswervingly selfless. Also, my children are a steady source of joy and bless me beyond what I deserve. I would not be where I am today without all of my family. I am thankful for each one of you.

It was just over one year ago that my Father passed away. He was tenacious and fought well to the end. This work is dedicated in honor and memory of my Dad.

Table of Contents

	Page
Abstract	iv
Acknowledgements	vii
Table of Contents	viii
List of Figures	xii
List of Tables	xviii
 I. Introduction	 1
1.1 Organization of Dissertation	1
1.2 Ceramic Composite Materials.....	2
1.3 Motivation.....	8
1.4 Problem Statement	10
1.5 Material Description	12
1.6 Methodology	13
 II. Background	 15
2.1 Ceramic Matrix Composites	15
2.2 Oxide-Oxide CMCs	17
2.3 Oxide Fibers.....	18
2.4 Creep in Ceramics.....	23
2.5 Effects of Environment Conditions on the Durability of Oxide Fibers and Oxide-Oxide CMCs.....	30
2.6 YAG – High Temperature Creep and Environmental Durability	38
2.7 Implications for Current Research.....	39
 III. Experimental Methods	 41
3.1 Research Materials.....	41
3.1.1 Nextel™ 610 and Nextel™ 720 Fiber Tows	41
3.1.2 Fiber Tow Test Specimens	42

	Page
3.1.3 Monolithic Alumina (Al_2O_3) and Yttrium Aluminum Garnet (YAG, $\text{Y}_3\text{Al}_5\text{O}_{12}$) Test Materials.....	44
3.1.4 YAG and Al_2O_3 Test Specimens.....	46
3.2 Experimental Facility – Ceramic Fiber Tow Testing	50
3.2.1 Testing Facility.....	51
3.2.2 Facility Verification – Room Temperature Stress-Strain Chart	59
3.2.3 Temperature Profiles	61
3.2.4 Strain Measurement.....	64
3.3 Experimental Facility – Compression Creep Testing	73
3.3.1 Testing Facility.....	74
3.3.2 Strain Measurement.....	79
3.3.3 Single Crystal YAG – Baseline Testing for YAG Pushrods.....	82
3.4 MTS Servo-Hydraulic Testing System Control.....	85
3.4.1 Tuning – The Concept.....	85
3.4.2 Tuning – The Procedure	89
3.5 Summary of Experimental Methods	90
IV. Mechanical Behavior of Nextel™ 610 Fiber Tows at 1100°C.....	92
4.1 Influence of Loading Rate on Tensile Strength of Nextel™ 610 Fiber Tows at 1100°C in Laboratory Air and in Steam.....	92
4.1.1 Determination of Subcritical Crack Growth Parameters for Nextel™ 610 Fiber Tows at 1100°C in Steam	95
4.2 Creep of Nextel™ 610 Fiber Tows at 1100°C in Laboratory Air.....	98
4.3 Creep of Nextel™ 610 Fiber Tows at 1100°C in Steam Environment	103
4.4 Predicting Creep Lifetimes from Constant Stress Rate Test Data for Nextel™ 610 Fiber Tows at 1100°C in Steam	109
4.5 Stress Rupture of Nextel™ 610 Fiber Tow at 1100°C in Air and in Steam and Monkman-Grant Failure Relationship.....	114
4.6 Summary of the Effects of Steam on the Mechanical Behavior of Nextel™ 610 Fiber Tows at 1100°C	117

	Page
V. Mechanical Behavior of Nextel™720 Fiber Tows at 1100 and 1200°C	119
5.1 Influence of Loading Rate on Tensile Strength of Nextel™720 Fiber Tows at 1200°C in Laboratory Air and in Steam.....	119
5.1.1 Determination of Subcritical Crack Growth Parameters for Nextel™720 Fiber Tows at 1200°C in Laboratory Air and in Steam	124
5.2 Creep of Nextel™720 Fiber Tows at 1100°C and 1200°C in Laboratory Air.....	124
5.3 Predicting Creep Lifetimes from Constant Stress Rate Test Data for Nextel™720 Fiber Tows at 1200°C in Air.....	133
5.4 Creep of Nextel™720 Fiber Tows at 1100°C and 1200°C in Steam Environment	135
5.5 Predicting Creep Lifetimes from Constant Stress Rate Test Data for Nextel™720 Fiber Tows at 1200°C in Steam	143
5.6 Stress Rupture of Nextel™720 Fiber Tow at 1200°C in Air and in Steam and Monkman-Grant Failure Relationship.....	145
5.7 Summary of the Effects of Steam on the Mechanical Behavior of Nextel™720 Fiber Tows at 1100 and 1200°C	147
VI. Creep Behavior of Polycrystalline Alumina (Al ₂ O ₃) at 1100 and 1300°C.....	149
6.1 Compressive Creep of Polycrystalline Alumina at 1100°C in Laboratory Air.....	149
6.2 Compressive Creep of Polycrystalline Alumina at 1100°C in Steam	152
6.3 Effect of Silica Doping on Compressive Creep Rates of Polycrystalline Alumina at 1100°C in Air and Steam.....	156
6.4 Compressive Creep of Polycrystalline Alumina at 1300°C in Laboratory Air.....	163
6.5 Creep of Polycrystalline Al ₂ O ₃ at 1300°C in Steam.....	166
6.6 Effect of Silica Doping on Compressive Creep Rates of Polycrystalline Alumina at 1300°C in Air and Steam.....	169
6.7 Summary of the Effects of Steam on the Creep Behavior of Polycrystalline Alumina at 1100 and 1200°C	171
VII. Creep Behavior of Polycrystalline Yttrium Aluminum Garnet at 1300°C	173
7.1 Compressive Creep of Polycrystalline Yttrium Aluminum Garnet at 1300°C in Laboratory Air	173

	Page
7.2 Compressive Creep of Polycrystalline Yttrium Aluminum Garnet at 1300°C in Steam.....	176
7.3 Effect of Silica Doping on Compressive Creep Rates of Polycrystalline YAG at 1300°C in Air and Steam.....	178
7.4 Summary and Assessment of the Feasibility of YAG Fiber Development	184
VIII. Conclusions and Recommendations	188
8.1 Conclusions.....	188
8.2 Contributions.....	191
8.3 Recommendations for Future Work.....	192
Appendix.....	195
Bibliography	197

List of Figures

	Page
Figure 1. Stress-Strain Curve	5
Figure 2. Damage Tolerance Design Mechanisms: (a) Weak fiber/matrix interface and (b) Porous matrix [172]	6
Figure 3. Failure of CMC with Strong Interface Bond Lacking Crack Deflection	7
Figure 4. Microstructural Design Philosophies for Damage Tolerant CMCs [171]	17
Figure 5. Relative strength retention of single filaments as a function of temperature [159]	20
Figure 6. Single filament strength retention after heat treatment [159]	21
Figure 7. Creep rates of Nextel™ fibers (data from 3M™ reported in [60])	23
Figure 8. Typical creep curve	24
Figure 9. Steady-state creep rates for Nextel™ 610 fiber tows (experimental data) and creep rates predicted for single filaments using power-law creep equation [50]	30
Figure 10. Tab for creep testing of ceramic fiber tow	43
Figure 11. Tab for monotonic tension testing of ceramic fiber tow	44
Figure 12. Compression creep specimen	46
Figure 13. Polycrystalline YAG (left) and Polycrystalline Alumina (right) Compression Specimens	47
Figure 14. MTS Landmark™ servo-hydraulic test system	53
Figure 15. MTS 653.03A two-zone furnace used for fiber tow testing	54
Figure 16. Experimental setup for creep testing of fiber tows with susceptor and steam feeding tube	54
Figure 17. Steam Generator	55
Figure 18. Load command signal (solid line) and load feedback signal (symbols) vs. time for Nextel™ 610 fiber tow at room temperature	57

	Page
Figure 19. Load command signal (solid line) and load feedback signal (symbols) vs. time for Nextel™ 610 fiber tow at 1100°C	57
Figure 20. Fiber tow specimen mounted in the dead weight creep testing facility with hydraulic grips seen in the background	59
Figure 21. Tensile stress-strain curves for Nextel™ 610 and Nextel™ 720 fiber tows obtained at Room Temperature in laboratory air	60
Figure 22. Temperature profiles obtained at 1100°C and at 1200°C in air (positive position corresponds to the top of furnace).....	63
Figure 23. Temperature profiles obtained at 1100°C and at 1200°C in steam (positive position corresponds to the top of furnace).....	63
Figure 24. Schematic representation of the effective gauge length for the Nextel™ 610 and 720 fiber tow specimens at 1100°C in air	70
Figure 25. Schematic representation of the effective gauge length for the Nextel™ 720 fiber tow specimen at 1200°C in air	70
Figure 26. Schematic representation of the effective gauge length for the Nextel™ 610 fiber tow specimen at 1100°C in steam. Steam port is located at the vertical midpoint of the susceptor.....	71
Figure 27. Schematic representation of the effective gauge length for the Nextel™ 610 and 720 fiber tow specimens at 1100°C in steam. Steam port is located at the bottom of the susceptor.	71
Figure 28. Schematic representation of the effective gauge length for the Nextel™ 720 fiber tow specimen at 1200°C in steam. Steam port is located at the bottom of the susceptor.....	72
Figure 29. MTS 810 servo-hydraulic test system.....	75
Figure 30. Compression test setup showing the susceptor	77
Figure 31. Compression creep test set-up for polycrystalline YAG and polycrystalline alumina specimens	79
Figure 32. Single Crystal YAG Specimen mounted for compression creep testing	84
Figure 33. Creep strain vs. time curve for single crystal YAG obtained at 200 MPa at 1300°C in steam	84

	Page
Figure 34. Poorly tuned servo-hydraulic system.....	88
Figure 35. Properly tuned servo-hydraulic system.....	88
Figure 36. Tensile strength as a function of stress rate for Nextel™ 610 fiber tow at 1100°C in steam. Effect of loading rate on ultimate tensile strength is evident.....	94
Figure 37. Creep strain vs. time curves for Nextel™ 610 fiber tows at 1100°C in laboratory air: (a) scale 0-20%, 0-50 h, (b) 0-10%, 0-10 h.....	100
Figure 38. Steady-state creep rate as a function of applied stress for Nextel™ 610 at 1100°C in laboratory air.....	101
Figure 39. Creep stress vs. time to rupture for Nextel™ 610 fiber tows at 1100°C in laboratory air. Arrow indicates that failure of specimen did not occur when the test was terminated.	102
Figure 40. Creep strain vs. time curves for Nextel™ 610 fiber tows at 1100°C in steam: (a) scale 0-20%, 0-10 h, (b) 0-10%, 0-2 h.....	106
Figure 41. Steady-state creep rate as a function of applied stress for Nextel™ 610 fiber tows at 1100°C in laboratory air and in steam	107
Figure 42. Creep stress vs. time to rupture for Nextel™ 610 fiber tows at 1100°C in laboratory air and in steam. Arrow indicates that failure of specimen did not occur when test was terminated.	109
Figure 43. Creep stress vs. time to rupture for Nextel™ 610 fiber tows at 1100°C in laboratory air and in steam. Arrow indicates that failure of specimens did not occur when the test was terminated.	113
Figure 44. Monkman-Grant plot of creep lifetime vs. steady-state strain rate for Nextel™ 610 and CMCs utilizing Nextel™ 610 at 1100°C in laboratory air and in steam	116
Figure 45. Tensile strength as a function of stress rate for Nextel™ 720 at 1200°C in laboratory air. Effect of loading rate on ultimate tensile strength is evident.....	120
Figure 46. Tensile strength as a function of stress rate for Nextel™ 720 fiber tow at 1200°C in steam. Effect of loading rate on ultimate tensile strength is evident.....	123

Figure 47.	Creep strain vs. time curves for Nextel™720 fiber tows at 1100°C in laboratory air	127
Figure 48.	Creep strain vs. time curves for Nextel™720 fiber tows at 1200°C in laboratory air: (a) scale 0-3%, 0-70 h, (b) 0-1%, 0-10 h.....	129
Figure 49.	Steady-state creep rate as a function of applied stress for Nextel™720 at 1100°C and 1200°C in laboratory air.....	130
Figure 50.	Creep stress vs. time to rupture for Nextel™720 fiber tows at 1100 and 1200°C in laboratory air. Arrows indicates that failure of specimens did not occur when the test was terminated.	132
Figure 51.	Creep lifetime data compared subcritical crack growth predictions for Nextel™720 tows in air at 1200°C	134
Figure 52.	Creep strain vs. time curves for Nextel™720 fiber tows at 1100°C in steam	137
Figure 53.	Creep strain vs. time curves for Nextel™720 fiber tows at 1200°C in steam	138
Figure 54.	Steady-state creep rate as a function of applied stress for Nextel™720 fiber tows at 1100°C and 1200°C in air and in steam.....	139
Figure 55.	Creep stress vs. time to rupture for Nextel™720 fiber tows at 1100 and 1200°C in laboratory air and steam. Arrows indicates that failure of specimens did not occur when the test was terminated.	142
Figure 56.	Creep lifetime data compared subcritical crack growth predictions for Nextel™720 tows in steam	144
Figure 57.	Monkman-Grant plot of creep lifetime vs. steady-state strain rate for Nextel™720 at 1200°C in laboratory air, steam and argon	146
Figure 58.	Creep strain vs. time curves for polycrystalline alumina at 1100°C in laboratory air	151
Figure 59.	Creep strain vs. time curves for silica doped polycrystalline alumina at 1100°C in laboratory air.....	151
Figure 60.	Creep strain vs. time curves for polycrystalline alumina at 1100°C in steam	153

	Page
Figure 61. Creep strain vs. time curves for silica doped polycrystalline alumina at 1100°C in steam.....	153
Figure 62. Steady-state creep rate as a function of applied stress for polycrystalline alumina and for silica doped polycrystalline alumina at 1100°C in laboratory air and in steam	154
Figure 63. Steady-state creep rates as functions of applied stress of polycrystalline alumina and of Nextel TM 610 fiber tow at 1100°C in laboratory air and in steam	155
Figure 64. Optical micrographs showing the grain structure of the undoped polycrystalline alumina (micrographs taken before creep testing)	158
Figure 65. Optical micrographs showing the grain structure of the silica doped polycrystalline alumina (micrographs taken before creep testing)	159
Figure 66. Normalized steady-state creep rates as functions of applied stress for polycrystalline alumina and for the Nextel TM 610 fiber tows at 1100°C in laboratory air and in steam.....	162
Figure 67. Creep strain vs. time curves for polycrystalline alumina at 1300°C in laboratory air	165
Figure 68. Creep strain vs. time curves for silica doped polycrystalline alumina at 1300°C in laboratory air.....	165
Figure 69. Creep strain vs. time curves for polycrystalline alumina at 1300°C in steam	167
Figure 70. Creep strain vs. time curves for silica doped polycrystalline alumina at 1300°C in steam.....	167
Figure 71. Steady-state creep rate as a function of applied stress for polycrystalline alumina and silica doped polycrystalline alumina at 1300°C in laboratory air and in steam	168
Figure 72. Normalized steady-state creep rate as a function of applied stress for polycrystalline alumina at 1300°C in laboratory air and in steam.....	170
Figure 73. Creep strain vs. time curves for polycrystalline YAG at 1300°C in laboratory air	174

	Page
Figure 74. Creep strain vs. time curves for silica doped polycrystalline YAG at 1300°C in laboratory air.....	174
Figure 75. Creep strain vs. time curves for polycrystalline YAG at 1300°C in steam	177
Figure 76. Creep strain vs. time curves for silica doped polycrystalline YAG at 1300°C in steam.....	177
Figure 77. Steady-state creep rate as a function of applied stress for polycrystalline YAG and for silica doped polycrystalline YAG at 1300°C in laboratory air and in steam	179
Figure 78. Optical micrographs showing the grain structure of: (a) silica doped polycrystalline YAG and (b) polycrystalline YAG.	180
Figure 79. TEM micrographs showing the grain structure of: (a) silica doped polycrystalline YAG and (b) polycrystalline YAG	181
Figure 80. Normalized steady-state creep rate as a function of applied stress for fine-grained polycrystalline YAG at 1300°C in laboratory air and in steam	183

List of Tables

	Page
Table 1. CMC Applications [2].....	4
Table 2. Nextel™ 610 and 720 Ceramic Fiber Properties	13
Table 3. Creep mechanisms in fine grain ceramic polycrystals.....	26
Table 4. Stress exponents for Nextel™ 610 fibers [49, 162]	29
Table 5. Creep activation energy for Nextel™ 610 fibers [49, 162].....	29
Table 6. Manufacturing Specifications for Nextel™ 610 and Nextel™ 720 Fiber Tows.....	42
Table 7. YAG Specimen Details.....	48
Table 8. Al ₂ O ₃ Specimens Details	49
Table 9. Tensile strength values obtained at various constant stress rates for Nextel™ 610 fiber tows at 1100°C in steam environment	94
Table 10. Summary of creep-rupture results for the Nextel™ 610 fiber tows at 1100°C in laboratory air.....	99
Table 11. Summary of creep-rupture results for the Nextel™ 610 fiber tows at 1100°C in steam.....	105
Table 12. Creep lifetime predicted from constant stress-rate data for Nextel™ 610 fiber tows at 1100°C in steam.....	112
Table 13. Tensile strength values obtained at various constant stress rates for Nextel™ 720 fiber tows at 1200°C in laboratory air	120
Table 14. Tensile strength values obtained at various constant stress rates for Nextel™ 720 fiber tows at 1200°C in steam environment	123
Table 15. Summary of creep-rupture results for the Nextel™ 720 fiber tows at 1100°C in laboratory air.....	126
Table 16. Summary of creep-rupture results for the Nextel™ 720 fiber tows at 1200°C in laboratory air.....	128

	Page
Table 17. Creep lifetime predicted from constant stress-rate data for Nextel™720 fiber tows at 1200°C in air	133
Table 18. Summary of creep-rupture results for the Nextel™720 fiber tows at 1100°C in steam	136
Table 19. Summary of creep-rupture results for the Nextel™720 fiber tows at 1200°C in steam	138
Table 20. Creep lifetime predicted from constant stress-rate data for Nextel™720 fiber tows at 1200°C in steam	143
Table 21. Summary of creep results for polycrystalline alumina at 1100°C in laboratory air	150
Table 22. Summary of creep results for polycrystalline alumina at 1100°C in steam	152
Table 23. Summary of creep results for polycrystalline alumina at 1300°C in laboratory air	164
Table 24. Summary of creep results for polycrystalline alumina at 1300°C in steam	166
Table 25. Summary of creep results for polycrystalline YAG at 1300°C in laboratory air	175
Table 26. Summary of creep results for polycrystalline YAG at 1300°C in steam....	176

CREEP PERFORMANCE OF OXIDE CERAMIC FIBER MATERIALS AT ELEVATED TEMPERATURE IN AIR AND IN STEAM

I. Introduction

1.1 Organization of Dissertation

The first chapter of this dissertation begins with an overview of the engineering field of ceramic composite materials. The motivation behind the present research is presented, followed by the research problem statement. Material descriptions and experimental methodologies are then discussed.

A general background and previous research efforts in the area of engineered ceramic composites are detailed in the second chapter. The third chapter provides an in-depth explanation of the experimental methods and facility designs for this research effort. Experimental results and analysis of the two ceramic fiber tow materials, Nextel™ 610 and 720, are presented in the fourth and fifth chapters, respectively. The sixth chapter provides experimental results and analysis of polycrystalline alumina (Al_2O_3). The seventh chapter provides experimental results and analysis of polycrystalline yttrium aluminum garnet (YAG, $\text{Y}_3\text{Al}_5\text{O}_{12}$), as well as an assessment of YAG for the next generation ceramic fiber. Chapter eight contains the conclusions and recommendations, followed by an appendix and bibliography.

1.2 Ceramic Composite Materials

Ceramic materials, even composite materials, have been used in their most basic form as far back as the ancient Egyptians (see Exodus 5 [1]). In the process of making structural bricks, straw was used by the Israelites living in ancient Egypt to strengthen the bricks [106, 143]. During this period, Egypt was deforested and relied heavily upon imported wood, which made firewood-kiln drying costly and time consuming [120]. Therefore, the straw was used to strengthen the bricks, making sun-drying possible rather than kiln-drying [120, 145]. Some four millennia later, several ancient Egyptian structures still exist. Archaeological efforts have revealed that much of the art and practice of brick making by the ancients has not significantly differed from common practices used today [106, 143].

Even though composite materials have been used in various ways throughout history, much of the advancement in research and development of composite materials for use in engineering applications has grown exponentially since the turn of the 20th century. In the 1930s and 1940s, honeycomb structures, compressed metal powders, and plastic with glass reinforcement were the forthcoming structural material technologies. Continuous glass fibers were produced commercially in 1939 [151]. Advanced fibers such as boron and carbon were developed in the 1950's and 1960's [54]. It was estimated in 1973 that 80% of all research and development efforts in composite materials have occurred since 1965, when the United States Air Force led the effort to bring high performance fiber composites to practical applications [26]. Today, engineered materials are finding more and more applications in space, aeronautics, energy, automotive, and other industries. In particular, engineered ceramic materials

were developed for operational use in harsh environments, like gas turbine combustors [89, 113, 116, 150], exhaust nozzle flaps and seals [167, 169], space transportation [137], nuclear power plant components [104], as well as for advanced automotive and biomedical applications [45].

Since the late 20th century, many active material science and engineering research efforts have been in the field of ceramic matrix composites (CMC). CMCs are designed to withstand high temperatures and provide environmental resistance, while remaining a vital load carrying members of a structure as opposed to a non-load bearing thermal or environmental coating. Structural components for hypersonic vehicles, rockets, jet engines, power plants, space vehicles, and furnaces are prime uses of CMCs [105]. Application of CMCs in combustors, for instance, will allow for higher operating temperatures, which in turn will reduce the need for cooling, reduce emissions, and increase efficiencies [66]. This high temperature performance of CMCs is a clear improvement over conventional nickel-based superalloys. Table 1 provides additional examples of military and commercial applications of CMCs.

Attempts to harness the favorable properties while minimizing the undesirable properties of ceramic materials led to significant developments in the area of CMCs. One of the inherent limitations of ceramic materials is their brittle nature. Monolithic ceramics tend to have linear stress-strain curves and unanticipated catastrophic failure. Thus, in order to use ceramic materials in structural applications, engineers and material scientists in the latter half of the 20th century began the development of CMCs. The goal of CMC development was to maintain the desirable mechanical, thermal, and environmental properties of ceramics while providing a mechanism for a more graceful

failure. CMCs had to be capable of providing both high strength and fracture toughness at high temperatures to be useful for engineering applications. Hence, the key advantage of CMCs over monolithic ceramics is their superior toughness, tolerance to the presence of defects and cracks, and non-catastrophic failure mode. Figure 1 shows typical tensile stress-strain curves for a monolithic ceramic material and for a CMC.

Table 1. CMC Applications [2]

Applications Sectors	Continuous Fiber CMCs			
MILITARY	<ul style="list-style-type: none">• F414 and F110 Nozzle Flaps and Seals• F117 Aft Deck Heat Shields• Engine Vanes• Flame Holders	<ul style="list-style-type: none">• Orbital Transfer Engine Thrusters• Low Cost Large Rocket Thruster (Million Pound) Heavy Lift Launch• Tactical Missile Combustors, Rotors• Divert and Attitude Control Thrusters	<ul style="list-style-type: none">• Turboramjet Variable Area Nozzles• Surveillance OTV Thrusters• Hypersonic Leading Edges, Inlet Cowlings and Nozzles• Linear Aerospike Engine, Thrust Cells and Ramp	
Commercial/Dual Use	<ul style="list-style-type: none">• Heat Exchangers• Radiant Burner Tubes• Land-Based Gas Turbines• Candle Filters	<ul style="list-style-type: none">• MDH Air Preheater Tubes• Immersion Heaters• Seal-less Magnetic Pumps• Motorcycle Brakes	<ul style="list-style-type: none">• Diesel Components• Valve Guides• Pistons• Turbocharger Rotors	

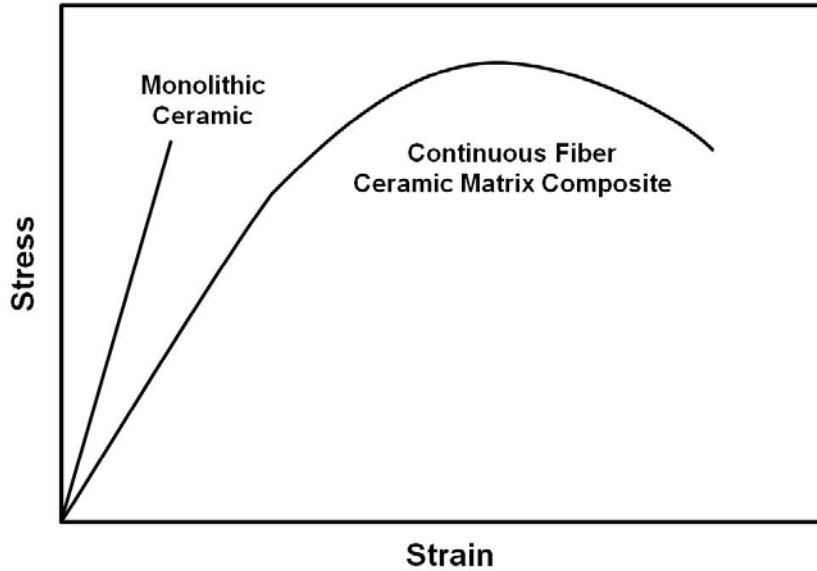


Figure 1. Stress-Strain Curve

In order to improve the fracture toughness of a CMC, cracks must be allowed to propagate within the material before catastrophic failure. Propagating matrix cracks must be deflected at the fiber-matrix interface while allowing the fiber to bear load in order to avoid brittle failure in a CMC. The improved fracture toughness of a CMC leads to the fiber bridging matrix cracks, uncorrelated fiber and matrix fracture, and subsequent fiber pullout and frictional sliding as loads are progressively transferred to fibers [40, 70]. Two major microstructural design philosophies emerged that enabled damage tolerance while maintaining structural integrity.

The first design philosophy relies on a weak fiber/matrix interface provided by a discreet compliant coating, which bonds poorly to the fiber and or matrix. In this composite system, the matrix material can remain dense. However, a fiber coating between the matrix and fibers redirects the cracks around the fibers into the matrix.

Therefore, the fibers are able to maintain load-carrying capability upon matrix cracking before the entire system gradually fails. Figure 2(a) demonstrates a propagating crack deflecting around fiber before fiber fracture. The disadvantages of this design philosophy include the difficulties and costs associated with coating fibers and the degradation of coating by oxidation of application temperatures in service environments.

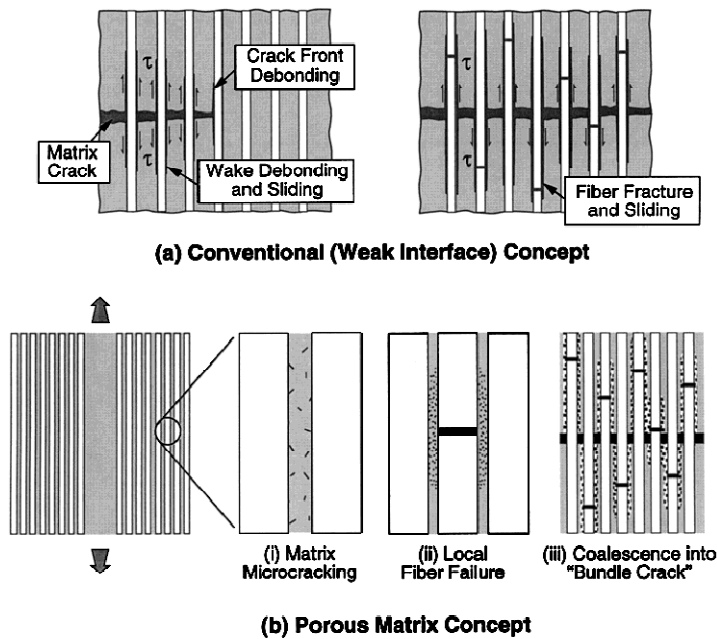


Figure 2. Damage Tolerance Design Mechanisms: (a) Weak fiber/matrix interface and (b) Porous matrix [172]

Another microstructural design philosophy relies on a porous matrix. In traditional composite systems, a dense matrix is desired in order to transfer load between matrix and reinforcement. However, in a dense matrix CMC with strong fiber/matrix interface bonding, a crack has the tendency to propagate quickly through both matrix and fibers, resulting in catastrophic failure similar to a monolithic ceramic. A brittle failure of a CMC with a strong interface is illustrated in Figure 3. However, when designed

properly, the porous matrix compromises the load transfer between matrix and fibers in order to provide paths for crack deflections. In this material system, microcracks propagate around the fibers and through the porous matrix. Once the crack impinges on the matrix-fiber interface, the crack requires less energy to propagate through the weak porous matrix around the fiber, leaving the fiber intact and able to carry load. Figure 2(b) demonstrates matrix microcracking prior to fiber failure and ultimate failure in a porous matrix CMC. One challenge of the porous matrix design philosophy is to provide a matrix that is weak enough for crack deflection, yet strong enough to transfer load to the fiber, especially under off-axis loading conditions.

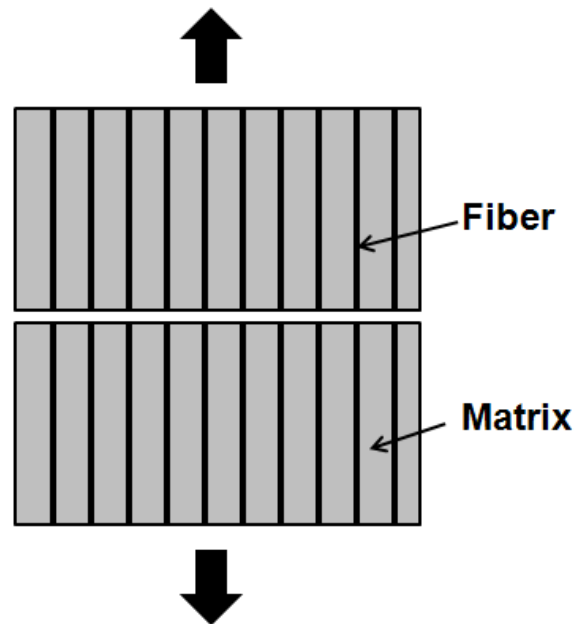


Figure 3. Failure of CMC with Strong Interface Bond Lacking Crack Deflection

While CMCs offer increased toughness and excellent high temperature properties, these materials must operate in aggressive environments. Because in engineering applications the CMCs are exposed to oxidizing environments at high temperatures, the thermodynamic stability and oxidation resistance of CMCs are vital issues. As CMCs emerged, one of the limitations of the non-oxide materials, like SiC, was degradation by oxidation. Oxidation of these materials severely degrades the mechanical properties and performance. In order to use CMCs in combustion environments, like jet engines, environmental resistance and mechanical performance in such environment must be addressed. The need for thermochemical stability led researchers toward the development of CMCs based on oxide constituents like alumina (Al_2O_3) [76, 95, 103, 142, 146, 149].

1.3 Motivation

The excellent high-temperature properties of the CMCs are directly related to the mechanical properties of the constituent fiber and matrix materials. Non-oxide ceramic materials offer very good high temperature mechanical properties. However, as previously mentioned, they are prone to oxidation. Oxide materials are by nature oxidation resistant and have displayed good high temperature mechanical properties.

Nevertheless, recent studies revealed dramatic degradation of mechanical performance of oxide-oxide CMCs subjected to mechanical loading at elevated temperature in steam environment [90, 125-131, 134-136]. When a CMC is subjected to mechanical loading at elevated temperature in steam environment, multiple degradation

and failure mechanisms operate simultaneously. Such mechanisms may include environmentally assisted (subcritical) crack growth, changes in the grain structure of the fibers and/or matrix, loss of matrix material, depletion of a particular phase in the fiber, matrix densification, etc. The majority of the aforementioned studies [90, 125, 126, 128, 129, 135, 136] investigated the behavior of the oxide-oxide CMC with 0°/90° fiber orientation. Because the mechanical performance of the composite with 0°/90° fiber orientation is dominated by the fibers, fiber degradation is a likely source of the composite degradation. Hence, it was suggested that environmentally-assisted subcritical crack growth in the Nextel™720 fibers may be the failure mechanism behind reduced creep lifetime of the Nextel™720/ Alumina composite at elevated temperature in steam.

In order for CMCs to be safely used in advanced aerospace applications such as jet engines, their environmental durability at elevated temperatures must be assured. Therefore, a thorough understanding of degradation and failure mechanisms operating in oxide fibers under these conditions is required. No studies evaluating mechanical performance of oxide fibers under these conditions have been published to-date. The present effort aimed to fill this knowledge gap. The mechanical performance of two oxide fiber materials in fiber form (Nextel™610 Al₂O₃ fiber, Nextel™720 Al₂O₃-SiO₂ fiber) were evaluated under static and monotonic loading at elevated temperature in air and in steam. Damage and failure mechanisms were elucidated.

In addition to investigating the effects of environment on high-temperature performance of two existing oxide fibers, a potential fiber material was also evaluated. Polycrystalline yttrium aluminum garnet (YAG, Y₃Al₅O₁₂) has been shown to exhibit low creep rates and low grain growth rates in a vacuum and in air. Additionally, YAG is very

corrosion resistant and has cubic lattice structure, which results in low residual stresses. These properties make YAG a viable candidate for a future fiber material. A YAG fiber would enable fabrication of superior creep and oxidation resistant CMCs capable of operating at temperatures in the 1400°C range. However, before embarking on costly YAG fiber development program, creep rates and degradation and failure mechanisms operating in YAG in combustion environments, specifically in steam, should be determined to assess mechanical properties under such conditions. If polycrystalline YAG exhibits creep rates in steam comparable to the Nextel™ fibers, this may obviate the need for YAG fiber development. This research effort aimed to qualitatively answer the following question: *Does steam have a dramatic effect on creep in YAG, and is the effect intrinsic to the material?*

1.4 Problem Statement

The aforementioned studies [90, 125-131, 134-136] that revealed remarkable deterioration of the mechanical performance of oxide-oxide CMCs at elevated temperature in steam are puzzling. The deleterious effects of steam on mechanical behavior of oxide-oxide CMCs must be better understood for further development and application of these materials in aerospace components.

The main objective of the research effort was two-fold. First, the effect of steam on mechanical performance of oxide fibers at elevated temperature was studied. An experimental facility was designed and a test method was developed that permits testing of fiber tows at temperatures of 1100 and 1200°C in air and in steam environments. The developed test method permitted accurate load control and, most importantly, accurate

strain measurement. Creep rates were determined and microstructural degradation and failure mechanisms operating in oxide fibers in combustion environments, specifically in steam, were assessed. This research effort constitutes a significant contribution towards understanding the mechanisms behind the poor performance of oxide materials at elevated temperature in steam and, consequently, towards improving the environmental durability of existing oxide fibers.

In addition to investigating the high-temperature mechanical performance in harsh environment of existing oxide fibers, the effects of steam environment on mechanical behavior of a candidate oxide fiber material was evaluated. Creep responses of polycrystalline YAG at elevated temperature in air and in steam were studied. An experimental facility was designed and a method was developed for testing high-purity polycrystalline YAG specimens in compression at 1300°C in air and steam environments. The developed test method permitted accurate strain measurement. Creep rates were determined. Additionally, compression tests of high purity, bulk polycrystalline alumina cubes were performed in air and steam at 1100 and 1300°C. Both the bulk alumina and YAG specimens were processed in two forms: with silica doping and without silica doping. These experiments were conducted to aid in understanding the effects of silica doping on the fiber materials. The alumina experiments at 1300°C were also used as a comparison to the YAG specimens. Microstructural degradation and creep mechanisms operating in YAG in combustion environments, specifically in steam, were assessed. Based on the results of this experimental study, the feasibility of the development of YAG fibers was assessed.

The objectives of this research can be summarized in the following problem statement:

Develop a test method for creep and creep-rupture of fiber tows under tensile loading at elevated temperatures in air and steam. Determine the effects of steam on creep performance of Nextel™ 610 and Nextel™ 720 oxide fibers at maximum operating temperatures of 1100 and 1200°C, respectively. Develop a test method for creep and creep-rupture of high-purity, polycrystalline YAG under compressive loading at 1300°C in air and steam. Determine the effects of steam on creep performance of YAG at 1300°C. Assess the feasibility of the development of YAG fibers. Identify the effects of silica doping on the creep performance of oxide fiber materials, specifically alumina and YAG, at elevated temperature in air and in steam.

1.5 Material Description

This research endeavor focused on two commercially available oxide fiber tows manufactured by 3M™ Corporation: Nextel™ 610 and Nextel™ 720. The Nextel™ 610 alumina fiber is composed of > 99% Al₂O₃. Additionally, the Nextel™ 610 fibers have been reported to contain approximately 0.35 wt% of SiO₂, which inhibits grain growth and aids in densification [12, 139, 162]. The Nextel™ 720 alumina-mullite fiber is composed of 85% Al₂O₃ and 15% SiO₂ by weight. Each fiber tow contains 400 individual filaments with a diameter of 12 μm. From this data, a cross sectional area of 4.52x10⁻⁸ m² was used for all engineering stress calculations. Table 2 below provides basic fiber properties from the manufacturer [3].

Additionally, high-purity single crystal and polycrystalline YAG and polycrystalline Al_2O_3 specimens were processed by the Air Force Research Laboratory, Materials and Manufacturing Directorate. For both YAG and Al_2O_3 , two processing batches were studied. One batch of each material was doped with 0.14 wt. % SiO_2 as a sintering agent. The other undoped batches of each material did not contain SiO_2 .

Table 2. Nextel™ 610 and 720 Ceramic Fiber Properties

	Nextel™ 610	Nextel™ 720
Composition, wt %	> 99% Al_2O_3	85% Al_2O_3 , 15% SiO_2
Denier/Filament Count	1500/400	1500/400
Crystal Size	< 500 nm	< 500 nm
Crystal Phase	α - Al_2O_3	α - Al_2O_3 + mullite

1.6 Methodology

The key objectives outlined in the problem statement were accomplished by the following tasks:

1. Designed an experimental facility for testing fiber tows at elevated temperatures (up to 1200°C) in air and in steam environments.
2. Developed the method for testing fiber tows under sustained loading at elevated temperature in air and in steam environment. Ensured accurate load control and provided for accurate strain measurement.

3. Investigated the effect of steam environment on creep performance of oxide fibers at elevated temperature.
 - a. Performed monotonic tension test. Investigated the effects of rate dependency for insight into slow crack growth as a dominant failure mechanism.
 - b. Performed creep testing. Evaluated the data obtained in mechanical tests.
4. Designed an experimental facility for testing high-purity polycrystalline YAG and Al_2O_3 specimens in compression at elevated temperatures (up to 1300°C) in air and in steam environments.
5. Developed the method for testing high-purity polycrystalline YAG and Al_2O_3 specimens in compression at 1300°C in air and in steam environments.
Ensured accurate load control and provided for accurate strain measurement.
6. Examined the effects of steam environment on creep performance of polycrystalline YAG at elevated temperature.
 - a. Performed creep testing. Evaluated the data obtained in mechanical tests.
7. Identified the effects of silica doping on the creep performance of oxide fiber materials, specifically alumina and YAG, at elevated temperature in air and in steam.
8. Assessed the feasibility of YAG as a candidate oxide fiber material for next-generation high-temperature CMCs.

II. Background

Aerospace applications demand structural materials that are tough, damage tolerant, oxidation resistant, and stable at high temperatures. Such materials must be able to withstand numerous service cycles before requiring repair or replacement. Due to the attractive properties of ceramic materials, such as high strength and stiffness, low density, and high melting temperatures, ceramics have been the top candidate materials for the most aggressive engineering applications. The use of ceramic materials in lieu of superalloys is not only expected to yield significant weight saving, but also to increase efficiencies and performance.

However, the major drawback of ceramic materials is their brittle nature and sensitivity to flaws and cracks, which leads to unpredictable catastrophic failure. Ceramic matrix composites (CMCs) have been developed to overcome the intrinsically low damage tolerance of monolithic ceramics. Therefore, CMCs are the revolutionary answer to the demands of the next generation aerospace structural components designed for service in severe environments.

2.1 Ceramic Matrix Composites

The main advantage of CMCs over monolithic ceramics is their superior toughness, tolerance to the presence of cracks and defects, and non-catastrophic mode of failure. The key to harnessing the desirable properties of ceramic materials in a CMC for structural application is designing the composite system that is damage tolerant. Two main microstructural design philosophies have emerged that promote the uncorrelated

fiber failure resulting in high fiber bundle strength and energy dissipation during subsequent fiber pullout [171]. It is now well recognized that CMCs can be designed to exhibit non-brittle fracture behavior and improved damage tolerance by introducing a weak fiber/matrix interface, which serves to deflect matrix cracks and to allow subsequent fiber pull-out [40, 68, 71]. It has been demonstrated that similar crack-deflecting behavior can also be achieved by means of a finely distributed porosity in the matrix instead of a separate interface between matrix and fibers [81]. This microstructural design philosophy implicitly accepts the formation of strong interfaces. It builds on the experience of porous debond fiber coating layers as crack deflection paths [31, 85] and extends the concept to utilize a porous matrix as a surrogate. The concept has been successfully demonstrated for oxide-oxide composites [37, 53, 76, 83, 146, 149, 166, 168]. Resulting oxide/oxide CMCs exhibit damage tolerance combined with inherent oxidation resistance. An extensive review of the mechanisms and mechanical properties of porous-matrix CMCs is given in [171, 172].

Figure 4 illustrates the two microstructural design approaches. First, fiber coating creates a weak interface between the fiber and matrix materials. The coating redirects impending cracks around the fiber and into the matrix. The second microstructural design approach is that of a porous matrix. In this system, the amount of energy necessary for cracks to propagate through the matrix is less than through the fiber. Therefore, a crack is diverted away from the fiber, and its energy is dissipated in the matrix material. Each design philosophy has inherent strengths and weaknesses. Nonetheless, the one factor common to all design approaches is the presence of fibers that must carry the loads at operational temperatures in service environments.

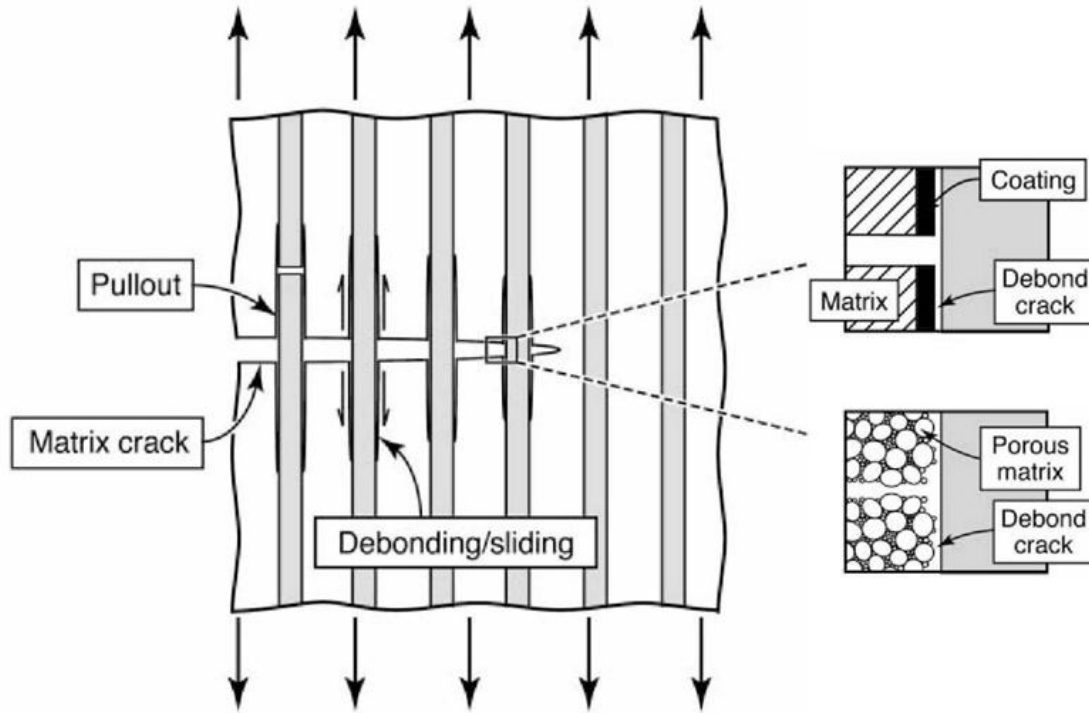


Figure 4. Microstructural Design Philosophies for Damage Tolerant CMCs [171]

2.2 Oxide-Oxide CMCs

Regardless of the microstructural design philosophy used in a CMC, the environmental effects on the constituent fiber and matrix are critically important to the mechanical performance of the CMC. Most of the current and anticipated applications of CMCs require operation in aggressive oxidation environments. Kerans et al. stated that the critical issue for improved CMC performance is combating environmental degradation [69].

Nonoxide fiber/nonoxide matrix composites generally show poor oxidation resistance [87, 119]. The degradation involves oxidation of fibers and fiber coatings, and is accelerated by the presence of moisture [41, 96, 98]. Numerous studies addressed

oxidation of SiC in moist environments [52, 62, 109-112]. Opila and Hann [112] and Opila [110, 111] reported that the presence of water vapor increased the rate of SiO₂ growth on SiC at high temperature, which led to accelerated rates of SiC recession. Degradation of boron nitride fiber coatings in moist environments has also been a subject of extensive research [27, 61, 63, 88, 97, 101, 108]. Nonoxide fiber/oxide matrix composites or oxide fiber/nonoxide matrix composites do not exhibit high oxidation resistance either. For these materials, the high permeability constant for the diffusion of oxygen results in rapid oxygen permeation through the oxide matrix [55]. These considerations motivated the development of continuous fiber CMCs based on thermochemically stable oxide constituents [76, 82, 84, 95, 99, 103, 142, 146, 149].

2.3 Oxide Fibers

Oxide fibers, specifically combination alumina-silica fibers, were first manufactured in the 1970s for high-temperature insulation [12]. Silica was added to maintain the transitional forms of alumina and inhibit growth of large and porous α -alumina grains. However, the presence of silica results in a reduced Young's modulus and poor creep resistance. To achieve high creep resistance nearly pure α -alumina fibers had to be produced. A dense, continuous α -alumina fiber, with a diameter of 10-12 μm , called NextelTM 610 was developed by 3MTM in the 1990s [162]. It is composed of ~99% α -alumina, although a detailed chemical analysis reveals 1.15% impurities, which include 0.67% Fe₂O₃ (a nucleating agent) and 0.35% SiO₂ (a grain growth inhibitor) [12]. In the mid 1990s, 3MTM also introduced a continuous α -alumina fiber containing a second phase

– the Nextel™720 alumina-mullite fiber. The Nextel™720 consists of ~85 wt. % Al_2O_3 and 15 wt. % SiO_2 [161] and has a diameter of 10-12 μm .

The oxide fibers of interest in the current research are Nextel™610 and Nextel™720 fibers. The development of the Nextel™610 fiber ushered a capability of tensile strengths greater than 3 GPa, which had previously only been achieved by SiC fibers [160]. Nextel™610 offers the highest room temperature tensile strength and the highest modulus among the Nextel™ fibers. The room temperature strength of Nextel™610 and 720 fibers at 25.4 mm gauge length are 3.1 and 2.1 GPa, respectively. However, the strength of the Nextel™610 fiber rapidly decreases at higher temperatures due to grain growth of its single phase composition [3]. Figure 5 presents the high temperature strength of a single filament for Nextel™610 and 720 fibers. The high-temperature strength data in Figure 5 is shown as percentage of room-temperature strength. Note that while the Nextel™610 fibers retained 70% of their room temperature strength up to 1000°C, the Nextel™720 fibers retained 70% of their room temperature strength up to 1300°C. The single filament data in Figure 5 suggest an improvement in temperature capability for Nextel™720 fibers relative to Nextel™610 fibers.

Because the processing temperatures of the oxide-oxide composites are typically higher than the application temperatures [31, 81], retention of fiber tensile strength after processing in the 1000-1300°C range is of particular interest. Figure 6 presents the room temperature tensile strength obtained for Nextel™610 and 720 fibers after 100-hour heat treatment at temperatures ranging from 1000 to 1400°C. It is seen that after heat treatment at 1300°C the strength of these fibers remains ≥ 2 GPa. The Nextel™720 fibers exhibit the least strength reduction, retaining about 85% of its room temperature strength

after 100 hours at 1300°C. Conversely, Nextel™ 610 fiber retains 80% of its room temperature strength after 100 hours at 1200°C.

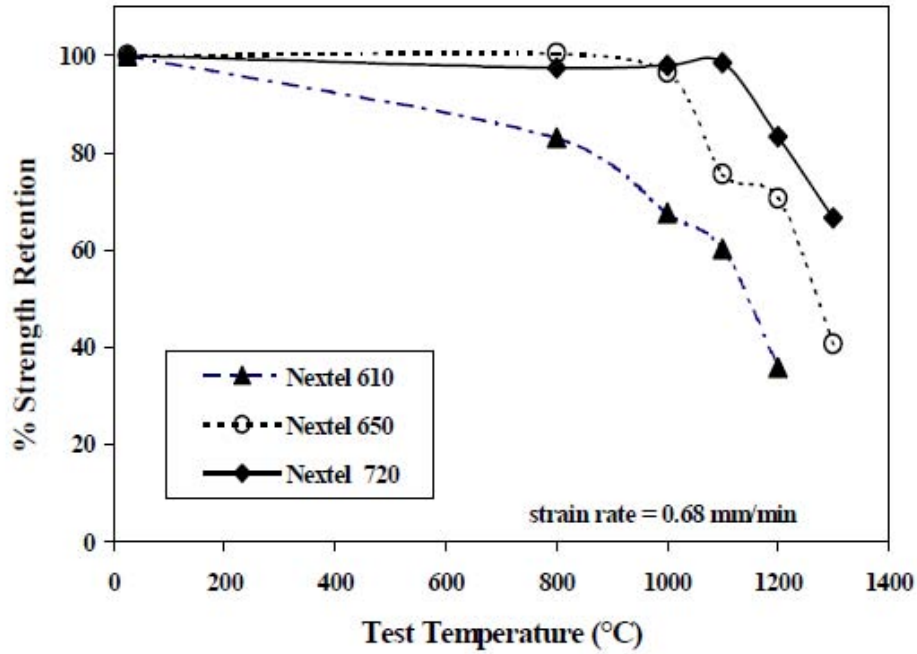


Figure 5. Relative strength retention of single filaments as a function of temperature [159]

Investigations of the response of the Nextel™ 720 fibers to thermal exposure are somewhat conflicting. Deléglise et al. [33] conducted a detailed analysis of the microstructural stability and room temperature properties of Nextel™ 720 fibers. Significant strength degradation was observed only above 1400°C for 5 hours exposure times. Milz et al. [92] observed catastrophic degradation after 2 hours at 1300°C. This severe degradation was attributed to locally enriched impurities and bulk fiber grain growth. Petry and Mah [117] reported that Nextel™ 720 filaments retained 75% of their room-temperature strength after 2 hours at 1300°C. A 9% loss in strength was seen after

2 hour exposure at 1100°C in air. Surface grooving, grain growth, or annealing of the subgrain boundaries were suggested as the possible causes of degradation. Schmücker et al. [140, 141] studied grain growth in Nextel™720 fiber due to thermal exposure. Little change in mullite grain size was seen after heat treatment at temperatures up to 1500°C, but rather high grain coarsening was observed after exposure at temperatures above 1600°C. Hay et al. [51] observed alumina grain growth in Nextel™720 fiber above 1250°C, whereas mullite grains did not grow as much as the alumina grains. At $\leq 1300^\circ\text{C}$, strength decrease with time at temperature was not associated with grain growth but was attributed to stress corrosion and/or boundary grooving.

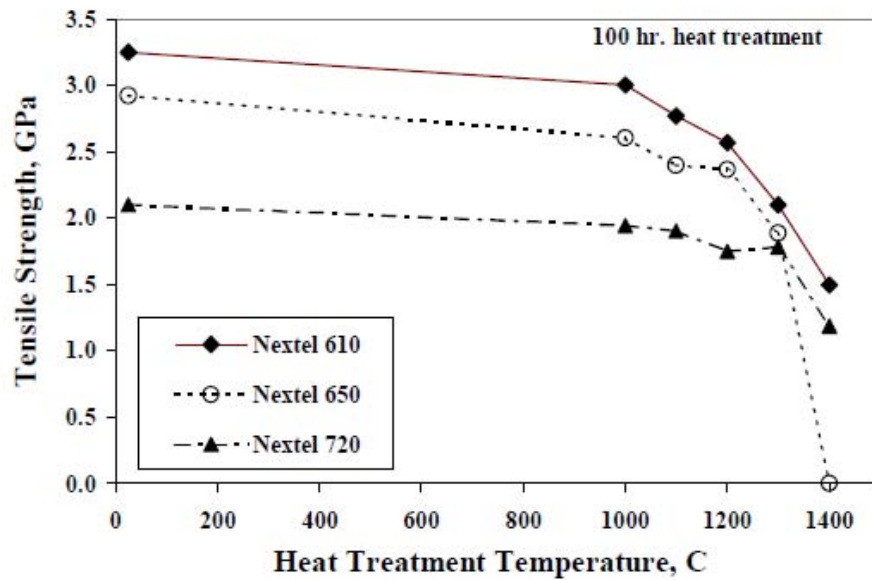


Figure 6. Single filament strength retention after heat treatment [159]

Wilson et al. [161] evaluated creep performance of Nextel™610 and Nextel™720 fibers in the 1000-1200°C temperature range by performing single filament, dead weight creep testing. Results are presented in Figure 7. It is seen that at a given temperature the

creep rates of Nextel™720 were three orders of magnitude lower than those of Nextel™610 fiber. Fitting the Nextel™610 and the Nextel™720 creep results with a temperature-independent Norton-Bailey equation of the form $\dot{\epsilon} = A \sigma^n$ yielded a stress exponent $n \approx 3$ for both Nextel™610 and Nextel™720 fibers. (Here $\dot{\epsilon}$ is the minimum creep rate, A is a temperature-dependent coefficient that accounts for the activation energy and other variables in the full form of the power-law, and σ is the applied stress). Bunsell et al. [12] also report the stress exponent of $n \approx 3$ for Nextel™610 fiber at temperatures between 1000 and 1200°C with an apparent creep activation energy of 660 kJ/mol.

The Nextel™720 fiber has the highest creep resistance of any commercially available oxide fiber. The Nextel™720 fiber is composed of mosaic grains of mullite with irregular contours and an average size of 500 nm, which in turn consist of clusters of smaller mullite subgrains. These clusters of slightly mutually disoriented mullite grains enclose some round or elongated grains of α -alumina with an average size between 50 and 100 nm. The improved creep performance of Nextel™720 fiber is attributed to the inherent creep resistance of mullite and to the gradual evolution of its microstructure toward elongated alumina grains oriented along the load direction [32]. However, the same microstructural factors that improve creep resistance leads to reduced strength [163]. Bunsell et al. [12] reported creep rates on the order of 10^{-6} s^{-1} for Nextel™720 fiber at 1400°C. Improved creep resistance was attributed to mullite microstructure. At 1200°C, Nextel™720 has two orders of magnitude reduced creep rate than any other commercially produced oxide fiber. It was also observed that failure frequently occurred via coalescence of cavities into large cracks over the whole gauge length. Local

cavitations and necking around heterogeneities were also found to induce failure sometimes. Deléglise et al. [32] also investigated the microstructural evolution of Nextel™ 720 fibers under load at high temperature. The fibers exhibited excellent creep resistance up to 1500°C. Deformation was attributed to grain boundary sliding through a thin aluminosilicate liquid phase and by preferential grain growth of load oriented grains.

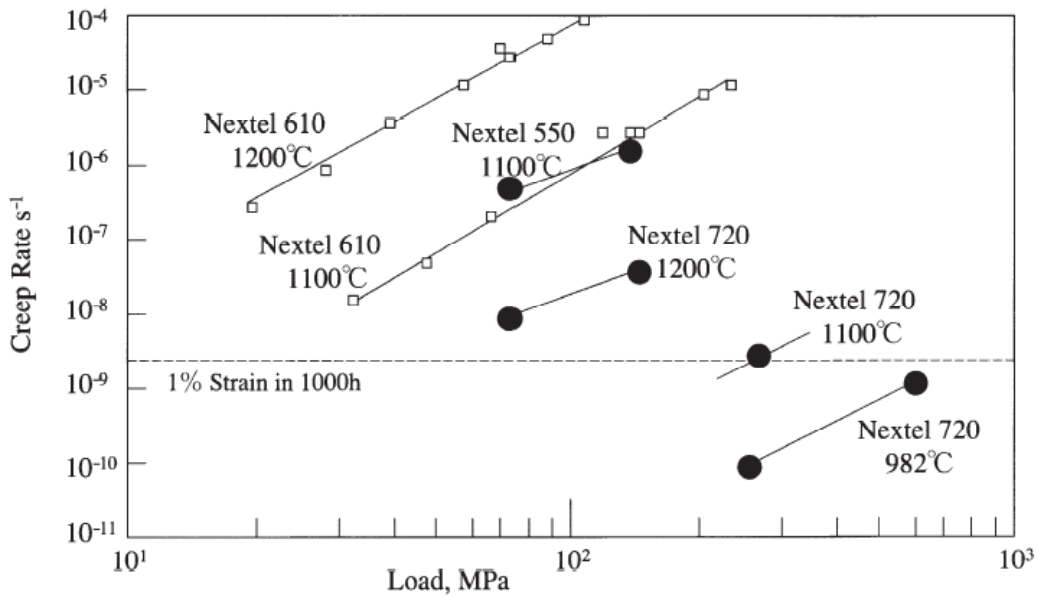


Figure 7. Creep rates of Nextel™ fibers (data from 3M™ reported in [60])

2.4 Creep in Ceramics

Considering the experimental results pertaining to creep of oxide fibers, it is instructive to review creep and its mechanisms. Creep can be simply described as the phenomenon of continuing plastic deformation under constant subcritical stress [152]. A typical creep curve is schematically shown in Figure 8. The creep curve is divided into

three regions: primary, secondary, and tertiary. Primary creep region is characterized by decreasing strain rate and is usually associated with changes in structure (like grain size, dislocation density) or with the redistribution of stresses. Secondary creep (also called steady-state creep) is the region where the strain rate is constant. In this case, creep is considered a result of deformation of an invariant microstructure. Tertiary creep is the region where strain rate is increasing. This stage is associated with failure initiation, namely formation of voids or cracks. In ceramics, tertiary is typically very short or can be non-existent [47].

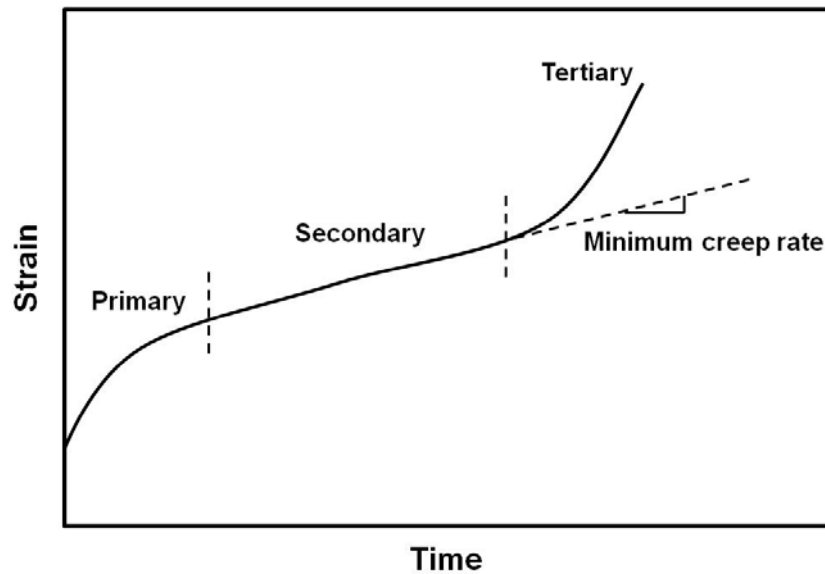


Figure 8. Typical creep curve

In creep studies of ceramics, attention is focused mainly on steady-state creep. At high temperature, steady-state creep in fine polycrystalline solids proceeds by grain-boundary sliding, diffusional creep (transport of matter and vacancies), or dislocation creep (movement of linear defects within a crystal structure). Depending on which

mechanism controls the greater amount of strain, one may speak primarily of grain boundary sliding, diffusion creep, or dislocation creep but these mechanisms are never completely dissociated, rather they are often coupled.

Diffusion creep by transport of vacancies and matter through the grains (lattice diffusion) is called Nabarro-Herring creep. If the transport occurs by diffusion along the grain boundary, it is termed Coble creep. In addition to diffusional mechanisms, grain boundary sliding can occur when a grain boundary glassy phase, used to aid densification in fabrication, softens at high temperature allowing creep to occur. The softening of this phase permits the grain boundary sliding. It is the glassy phase viscosity that controls the creep. Dislocation creep can be divided into dislocation glide or climb. Dislocation glide is also referred to as slip. In dislocation glide, lattice planes move in a shear direction over one another. In dislocation climb, the movement of a dislocation is perpendicular to its glide plane. Movement of vacancies through the lattice to an adjacent position on the edge of the dislocation causes the dislocation to “climb.”

It is widely recognized that the creep rate of materials can be expressed by the following form of the Arrhenius rate equation:

$$\dot{\epsilon} = \frac{AD\mu b}{kT} \left(\frac{b}{d} \right)^m \left(\frac{\sigma}{\mu} \right)^n \quad (1)$$

where $\dot{\epsilon}$ is the steady-state creep rate, A is a dimensionless constant, D is the diffusion coefficient or diffusivity, μ is the shear modulus, b is the Burgers vector, d is the grain size, k is the Boltzmann constant, T is the absolute temperature, σ is the applied stress, m is the grain size exponent and n is the stress exponent. Furthermore, the diffusion

coefficient, D , is given by:

$$D = D_o \exp\left(\frac{-Q}{RT}\right) \quad (2)$$

where D_o is a frequency factor, Q is the creep activation energy, and R is the universal gas constant.

Attempts to describe the different creep mechanisms have been correlated to different values of exponents m and n . The values of m and n can be obtained from the experimental creep data. Hence, in principle, the predominant creep mechanism can be identified from the analysis of creep data. Table 3 provides a summary of predominant creep mechanisms for fine grain ceramic polycrystals [11, 47].

Table 3. Creep mechanisms in fine grain ceramic polycrystals

n stress exponent	m grain size exponent	Mechanism
1	2	Diffusional creep through lattice (Nabarro-Herring creep)
1	3	Diffusional creep along grain boundaries (Coble creep)
2	1	Grain boundary sliding and interface-reaction controlled creep
4	3	GBS and cavity growth
3-5	0	Dislocation creep: 3 –glide controlled, 5 –climb controlled
>5		Cavity growth controlled creep

The theoretical analysis of Nabarro-Herring creep yields the grain size exponent $m = 2$; whereas, the analysis of Coble creep yields $m = 3$. Because of the inverse cubic dependence on grain size, Coble creep is dominant over Nabarro-Herring creep at very small grain sizes [152]. Furthermore, because the activation energy for grain-boundary diffusion is smaller than that for lattice diffusion, Coble creep typically dominates over Nabarro-Herring creep at lower temperatures [118].

For both Coble creep and Nabarro-Herring creep, grain boundaries are assumed to be perfect sources or sinks for vacancies. These classical treatments of diffusional flow of polycrystals are adequate for explaining many experimental observations. However, when the sources and sinks become small, these processes may be controlled by a reaction at the interface, leading to an interface-reaction controlled diffusional creep mechanism. In interface controlled creep, either the lattice diffusion or the grain boundary diffusion is so rapid that creation and annihilation of point defects at grain boundaries is the rate-controlling process [6, 15, 47].

As previously mentioned, Wilson et al. [161] found a stress exponent of approximately 3 for both NextelTM610 and NextelTM720 fibers. The creep deformation mechanism was attributed to interface-reaction controlled diffusion. Identifying additional details of the deformation process in NextelTM720 was difficult due to the complex microstructure. The mosaic crystal microstructure contains low angle grain boundaries between subgrains, which act as imperfect locations for creation and annihilation of defects supporting interface-reaction controlled diffusion. Additionally, it was noted that grain boundary sliding would be reduced due to the large mosaic crystals.

Cannon et al. [15, 17] studied plastic deformation of polycrystalline alumina (grain size: 1-15 μm). The results suggest that diffusional creep dominates and quickly becomes interface-reaction controlled, explaining the often reported non-Newtonian creep behavior of fine-grained alumina. Pysher et al. [123, 124] studied creep of alumina and alumina-zirconia polycrystalline fibers and also reported results consistent with the interface controlled diffusion mechanism.

Hammond et al. [50] compared creep response of Nextel™ 610 fiber tows to that of Nextel™ 610 single filaments. It was concluded that the governing creep mechanism for both fiber tows and single filaments was the interface-reaction controlled creep. The creep response of fiber tows compared well to that of single filaments at 1000°C and 1100°C. However, brief exposures to sintering temperatures (1400°C) led to significant reductions in the steady-state creep rate of the fiber tows due to the formation of filament clusters. Figure 9 shows a comparison between the experimental creep rates for the as-received Nextel™ 610 fiber tows and the creep rates predicted for the single filaments by the standard power-law creep relation:

$$\dot{\epsilon} = A\sigma^n \exp\left(\frac{-Q}{RT}\right) \quad (3)$$

where $\dot{\epsilon}$ is the steady-state creep rate, A is a dimensionless constant, σ is the applied stress, n is the stress exponent, Q is the creep activation energy, R is the universal gas constant, and T is the absolute temperature. Additional steady-state creep rate data for Nextel™ 610 fiber tows and for Nextel™ 610 single filaments is provided in Table 4 and Table 5. Hammond et al. concluded that, even though the fiber tows are known to have less ultimate tensile strength than a single filament, the steady-state creep rate of alumina

fiber tows can be accurately predicted from the experimental data obtained for single filaments. It was also emphasized that because composites utilize fiber tows, the tests conducted on tows were more representative of the actual service conditions than those conducted on single filaments.

Table 4. Stress exponents for Nextel™ 610 fibers [49, 162]

Fiber	Stress Exponent at 1000°C	Stress Exponent at 1100°C
Nextel™ 610 single filament	2.8	3.1
Nextel™ 610 tow, as received	4.2	2.9
Nextel™ 610 tow, 1400°C/60s	N/A	4.7

Table 5. Creep activation energy for Nextel™ 610 fibers [49, 162]

Fiber	Creep activation energy (kJ/mol)
Nextel™ 610 single filament	660
Nextel™ 610 tow, as received	644
Nextel™ 610 tow, 1400°C/60s	662

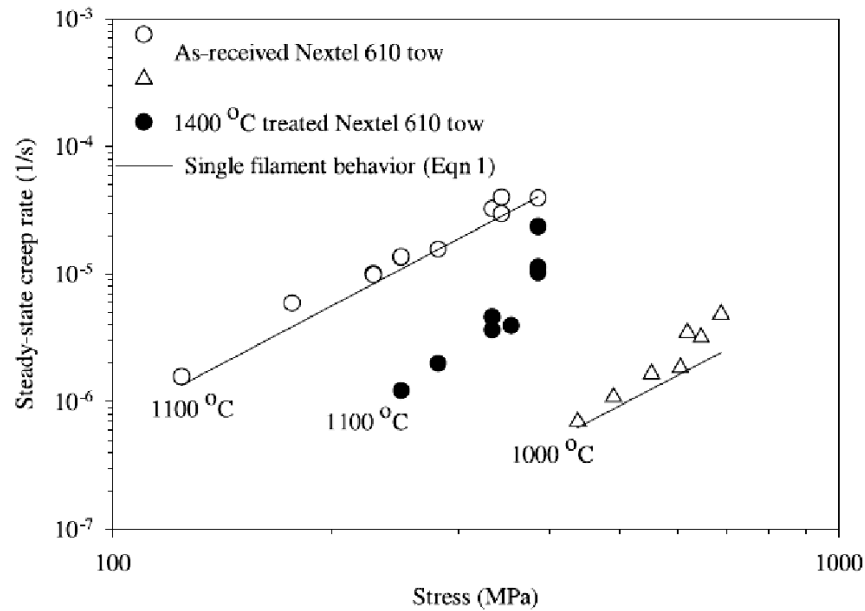


Figure 9. Steady-state creep rates for Nextel™ 610 fiber tows (experimental data) and creep rates predicted for single filaments using power-law creep equation [50]

2.5 Effects of Environment Conditions on the Durability of Oxide Fibers and Oxide-Oxide CMCs

The need for thermochemically stable composites motivated the development of CMCs based on oxide constituents. Oxide materials chosen as CMC constituents are inherently stable in oxidizing environments. However, these materials are not entirely resistant to the environmental degradation. Even though alumina, mullite, and YAG are thermodynamically stable and oxidation resistant under one set of conditions, they may be vulnerable to other environmental effects under extreme conditions.

Before reviewing the experimental results pertaining to environmental durability of the CMCs, it would be useful to review the concept of fracture toughness and the phenomenon of subcritical crack growth. Fracture toughness refers to the ability of a

material containing cracks, flaws, and/or voids to resist fracture. Generally, a material will fail when the stress intensity factor for a particular flaw reaches the critical value, namely its fracture toughness. However, subcritical crack growth in a material can occur when the stress intensity factor is below the fracture toughness of the material. Several mechanisms can lead to subcritical crack growth, but it is most commonly attributed to environmentally assisted crack growth (aka stress corrosion) [47].

Effects of the environment on crack growth can be profound. Typically, the environmental species must be transported along a crack interface before any interaction can take place at the crack front. Environmental species then interact with the chemical bonds in the vicinity of the crack tip, resulting in less energy required to break the chemical bonds at the crack tip and facilitates crack growth under loads that produce stress intensity factor below the material's fracture toughness. This process is called environmentally assisted (subcritical) crack growth. Since this process requires the movement of the environmental species to the crack tip region, it may become limited by the rate of transport, which leads to time dependent crack growth [78].

In many ceramic materials, cracks grow slowly under applied stress that gives rise to the stress intensity factor well below the critical value. At room temperature, the primary subcritical crack growth mechanism in ceramics involves a stress-assisted reaction with the environment. The rate of crack growth is determined by the rate of transport of the environmental species to the crack tip [152], and by the rate of reaction of the environmental species with the material bonds at the crack tip [156]. Thus, subcritical crack growth is extremely sensitive to applied loads, concentration of environmental species, and temperature.

A number of researchers explored the subcritical crack growth in oxide ceramics. Cao et al. [18] studied the environmentally assisted crack growth in fine-grained alumina at temperatures in the 1300-1400°C range. Silicate glass drops were applied to the alumina surface. Premature cracking was attributed to stress-enhanced corrosion due to the penetration of the amorphous glass into the grain boundaries. The presence of the glass phase in the grain boundaries created local embrittlement and reduced the strength.

Oda et al. [107] examined the corrosion behavior of high purity bulk alumina in water at 300°C and 8.6 MPa. Weight loss due to corrosion was attributed to dissolution of silicon dioxide and sodium oxide grain boundary impurities. As expected, fracture strength of corroded specimens was correlated to impurity content.

Two related studies [44, 72] investigated corrosion resistance of various oxide and non-oxide ceramics in a hot (1200-1500°C) gas environment including water vapor. At temperatures above 1300°C in the presence of water vapor, alumina and mullite exhibited degradation that was attributed to the formation of and evaporation of volatile hydroxides ($\text{Al}(\text{OH})_3$ and $\text{Si}(\text{OH})_4$). Surface etching of alumina was observed and was viewed as the result of attack of water vapor on the grain boundaries where the impurities accumulate. However, the cross-section of the alumina sample did not show a corrosion layer. Conversely, a porous layer of alumina was formed on the surface of the mullite sample at the conclusion of the corrosion test. Additionally, silicon leached out of the surface with time and reacted with water vapor. The porous corrosion layer on the surface of the mullite sample did not protect the bulk material underneath from corrosion. It was also concluded that mullite exhibited a higher recession rate than alumina. YAG displayed remarkable stability in the corrosive environment as compared with alumina and mullite.

With increasing time, the corrosion rate was reduced due to the formation of a dense surface layer containing Y_2SiO_5 , and $\text{Y}_4\text{Al}_2\text{O}_9$, which protected the material from further corrosion.

Previous exposure to steam and high temperature argon environments have been observed to cause decrease in strength of high purity alumina. Tai et al. [147] reported grain growth and grain boundary etching of high purity alumina exposed for 10 hours to argon and argon/steam environments at temperatures ranging from 1300°C to 1700°C. Flexural strength remained constant after exposure at temperatures of 1300°-1600°C. However, the microstructure, flexural strength, and volume were significantly affected by exposure to Ar/H₂O environment at 1700°C. Severe grain boundary etching was observed that was attributed to the formation of gaseous $\text{Al}(\text{OH})_3$ and $\text{Al}(\text{OH})_2$ in the grain boundaries. Furthermore, substantial grain growth was noted near the specimen surface. The decrease in flexural strength at 1700°C was attributed to the grain growth and grain boundary etching.

Kronenberg et al. [74] and Castaing et al. [19] characterized the hydrogen impurities in hydrothermally annealed ceramics and evaluated the reduction in strength in $\alpha\text{-Al}_2\text{O}_3$ and sapphire ceramics associated with the hydrogen incorporation. Single crystal $\alpha\text{-Al}_2\text{O}_3$ specimens and polycrystalline $\alpha\text{-Al}_2\text{O}_3$ (3-5 μm and 30-50 μm grain size) specimens were annealed in water at temperatures ranging from 850 to 1025°C, under high pressure (1500-2000 MPa) to promote hydrogen penetration. The uptake of water by the polycrystalline alumina was reported to be ~100 times greater than that taken up by the single crystal sapphire subjected to the same hydrothermal treatment. This result suggests that the grain boundaries served as rapid transport pathways or hydrogen traps in

the ceramic. The SEM micrographs of the fracture surfaces were utilized to characterize the nature of grain boundary alterations resulting from the annealing process. Untreated ceramics showed trans-granular fracture, whereas, the hydrothermally treated specimens showed intergranular fracture, demonstrating the weakening of the grain boundaries. The grain boundaries of the untreated specimens were tight solid-solid interfaces. In contrast, the grain boundaries of the hydrothermally treated specimens became permeable open structures due to annealing treatment. Hydrothermal corrosion of alumina was attributed to the severely damaged grain boundaries, suggesting that grain boundaries react strongly with water at high pressures and moderate temperatures (850-1025°C). Grain boundaries and impurities provided a short-circuit diffusion paths for incorporation of hydrogen defects. The presence of the hydrogen impurities significantly reduced the material strength. The yield stress of sapphire and large grain (30-50 μm) polycrystalline alumina were reduced by a factor of two in the presence of water. This was attributed to enhanced dislocation glide. The yield stress of small grain (3-5 μm grain size) polycrystalline alumina was reduced by a factor of six in the presence of water. This result was attributed to the mechanism change from dislocation glide to grain boundary sliding. Korinek et al. [73] performed a TEM examination of the alumina specimens tested by Castaing et al. [19]. In general, the study concluded that small grain size promotes the activation of grain boundary sliding. Additionally, the presence of hydrogen induced a hydrothermal softening and changed the deformation mechanisms. The relevance of these studies to the present work is lacking due to the very high test pressures. However, these effects may be important for applications that must operate in high pressure, steam-rich environments.

Kruzic et al. [75] studied the fracture toughness of high purity alumina in both dry and moist environments at room temperature. Fracture toughness was reported to be 30% lower in moist air than in dry nitrogen environment.

Schmücker et al. [138] examined water vapor corrosion of single crystal and polycrystalline mullite at 1200°C. The polycrystalline mullite displayed non-isotropic corrosive formation of α -Al₂O₃, whereas the α -Al₂O₃ formation did not depend on orientation in the single crystal mullite.

Göring et al. [46] investigated creep and subcritical crack growth at 1000°C in air of Nextel™720 single filaments, which were subjected to a 2 hour heat treatment at 1300°C to simulate composite processing conditions. The authors concluded that creep deformation controlled the long term behavior, while the subcritical crack growth played only a minor part. In a subsequent study, Milz et al. [92] evaluated the thermal stability of Nextel™720 fibers by conducting tensile tests at various temperatures on single filaments subjected to prior heat treatment at temperatures up to 1300°C. Bulk fiber grain growth was detected after heat treatment at temperatures above 1200°C. Furthermore, severe degradation of the fiber material occurred during heat treatment at 1300°C, which was caused by local impurities. Milz et al. reported no subcritical crack growth occurred at 900°C. However, intense subcritical crack growth was observed at temperatures $\geq 1000^\circ\text{C}$. At 1200°C, nonlinear elastic deformation occurred, indicating that the fracture behavior was controlled by creep damage.

Deléglise et al. [32] studied tensile and creep behaviors of the Nextel™720 fibers at elevated temperatures. At temperatures $\geq 1000^\circ\text{C}$, cracks were observed to nucleate around surface flaws. Additionally, the dissolution of mullite into a liquid phase and

alumina grain growth occurred around the crack tip providing the necessary conditions for subcritical crack growth. Under sustained loading, mullite progressively dissolved to form an alumino-silicate phase. Creep deformation was reported to occur by grain boundary sliding through the liquid phase and by preferential growth of elongated alumina particles. In creep, provided grain growth is restricted, damage could be accumulated by the coalescence of several intergranular microcracks, ultimately leading to failure. Alternatively, creep failure could occur catastrophically due to the growth of large grains or cavities.

Wannaparhun et al. [153] reported that exposure of a Nextel™720/Al₂O₃ CMC to water vapor at 1100°C resulted in depletion of mullite phase and increase in the alumina content in the Nextel™720 fiber. Because the superior high-temperature creep performance of the Nextel™720 fibers is due in part to the mullite, the authors speculate that the leaching of SiO₂ from the fiber could be responsible for a loss of creep resistance at 1100°C in water-vapor environments. However, the percent change on the surface of the fibers to the whole may not be significant to the overall creep resistance of the fiber. Nevertheless, Campbell et al. [14] observed an approximately 15% reduction in strength of Nextel™720/Al₂O₃ CMC after a 1000-hour exposure to water vapor at 1200°C.

Research efforts led by the Air Force Research Laboratory demonstrated superior high temperature durability of oxide fiber CMCs over SiC CMCs in terms of moisture resistance [170]. Three SiC containing CMCs and two oxide-oxide CMCs were subjected to alternating fatigue loading and exposure to salt water fog environment. The oxide-oxide CMCs were reinforced with Nextel™610 and Nextel™720 fibers. The CMCs containing SiC fibers exhibited a significant decrease in fatigue life due to salt water fog

exposure. However, both oxide-oxide CMCs showed no loss in fatigue performance or retained strength due to moisture exposure or due to salt water fog exposure.

An additional effort by the Air Force Research Laboratory further studied the effects of exposure to salt water with different concentrations of salt (1 and 5 wt%) at various temperatures (900-1200°C) on the strength and microstructure of Nextel™ 720 fibers and Nextel™ 720/-aluminosilicate composite [114]. Exposure in 1 wt% NaCl salt water solution caused no degradation of fiber strength. However, significant degradation of fiber strength was observed after exposure in 5 wt% salt water solution at temperatures between 900-1150°C. Surprisingly, no degradation in fiber strength was observed after exposure in 5 wt% NaCl salt water solution at 1200°C. Flaw healing or rapid water evaporation was assumed to be responsible for the results obtained at 1200°C. Additionally, this study concluded that the relative contribution of fiber strength to the total composite strength was approximately 50%, indicating that both fiber and matrix were degraded due to exposure to salt water solution.

Recent studies at the Air Force Institute of Technology have revealed the degradation of mechanical performance of oxide-oxide CMCs in the presence of steam at elevated temperatures [90, 125-131, 134-136]. Several studies by Ruggles-Wrenn et al., investigated creep behavior of oxide-oxide CMCs in tension [125, 126, 128, 129, 131, 134, 136], compression [135], and interlaminar shear [130]. Experiments were performed at elevated temperature in air and in steam environment. Results revealed that reduced creep lifetimes and accelerated creep rates were produced in the presence of steam. Additionally, the presence of steam was reported to significantly degrade fatigue performance of an oxide-oxide CMC [90, 127].

2.6 YAG – High Temperature Creep and Environmental Durability

As mentioned, the Nextel™ 720 fiber has the best creep performance of any commercially available polycrystalline oxide fiber. However, further improvements in creep resistance of the ceramic fibers are desirable. YAG is recognized as the most creep resistant polycrystalline oxide and also exhibits very slow grain growth [43, 163].

However, a commercially available YAG fiber is yet to be developed.

Parthasarathy et al. [115] studied the creep behavior of fine grained YAG at temperatures ranging from 1400°C to 1610°C in a vacuum. The creep stress exponent was determined as 1.24 and the activation energy as 584 kJ/mol. TEM examination of the YAG specimens and comparison of the creep rates produced by the fine grained (~3µm) YAG specimens with those produced by the single crystal YAG specimens suggest that polycrystalline YAG creeps by the Nabarro-Herring mechanism.

Experimental polycrystalline YAG fibers were produced and studied by Morscher et al. [102]. The 95% dense YAG fibers measured 15-30 µm in diameter and were composed of 1 µm grains. The creep activation energy was 744 kJ/mol and the tensile strength was ~ 1 GPa. Increased relaxation resistance at temperatures ranging from 1000 to 1400°C was evaluated by Bend Stress Relaxation technique. The increased relaxation resistance of YAG over other polycrystalline oxide fibers suggested improved creep-limited use temperatures of the YAG fibers over current polycrystalline oxide fibers.

Pullar et al. [122] produced and studied another experimental polycrystalline YAG fiber. A continuous, 98.5% dense YAG fiber with a 5.5 µm diameter and 1 µm grain size was produced from an aqueous sol-gel precursor. Creep resistance was measured by Bend Stress Relaxation technique at temperatures ranging from 1000 to

1300°C in air. Creep properties were reported to improve with increased processing temperature, and creep rates were suspected to be affected by grain boundary impurities, especially sodium contamination. In a subsequent study, sodium-free gel precursor fibers were used to form pure phase YAG fibers [121]. These YAG fibers exhibited superior creep resistance than the earlier generation YAG fibers, demonstrating that sodium contamination is detrimental to creep performance of YAG.

Previously mentioned work by Klemm et al. [72] and Fritsch et al. [44] studied the corrosion resistance of various ceramics in a hot gas flow including water vapor. The corrosion resistance of YAG in a corrosive environment was found to be superior to that exhibited by alumina and mullite. The corrosion rate of YAG was reduced as a formation of a dense surface layer containing Y_2SiO_5 and $\text{Y}_4\text{Al}_2\text{O}_9$ protected the material from further corrosion.

2.7 Implications for Current Research

Results of the aforementioned studies on oxide fiber materials and oxide-oxide CMCs reveal the degrading effect of steam on the creep performance of oxide-oxide CMCs. The mechanical behavior of a composite with 0°/90° fiber orientation under tensile loading is fiber-dominated. Therefore, fiber degradation is a likely source of composite degradation. It is recognized that the Nextel™720 fiber has the highest creep resistance of any commercially available oxide fiber. The superior creep performance of the Nextel™720 fiber is due to larger grain sizes, complex grain morphology and to the presence of mullite, which has better creep resistance than alumina. However, degradation of the creep performance of Nextel™720 fibers in the presence of steam may

be the primary cause of the degraded creep performance of the NextelTM720-reinforced CMCs in steam environment. Hence a thorough understanding of creep performance of this and other oxide fibers in the presence of steam is key to understanding the mechanisms behind the detrimental effect of steam on creep resistance of oxide-oxide CMCs. Therefore, investigation of the creep behavior, determination of the creep rates and of the underlying microstructural creep mechanisms acting in the oxide fiber materials in the presence of steam at elevated temperature are critical to improving the creep performance of oxide fibers and of oxide-oxide CMCs.

Results from prior investigations demonstrate that polycrystalline YAG is a very promising candidate material for the next generation fiber. However, as the review of published literature reveals, the effects of a steam environment on the creep performance of polycrystalline YAG have not been studied. The question remains: *Does the presence of steam have a similar detrimental effect on the creep behavior of YAG as it does on the creep resistance of alumina and that of mullite?* This question must be answered before a costly effort to develop YAG fibers is undertaken.

III. Experimental Methods

This chapter describes in further detail the test materials, specimen preparation, and experimental methods developed in this research. This chapter specifically addresses the following objectives:

- *Develop a test method for creep and creep-rupture of fiber tows under tensile loading at elevated temperatures in air and in steam*
- *Develop a test method for creep and creep-rupture of high-purity, polycrystalline YAG under compressive loading at 1300°C in air and in steam*

Accomplishment of these two objectives was critical to the completion of the remaining objectives of this research.

3.1 Research Materials

3.1.1 Nextel™ 610 and Nextel™ 720 Fiber Tows

The two types of fiber tows studied in this research, Nextel™ 610 and Nextel™ 720, were manufactured by 3M™ Corporation. Nextel™ 610 fiber is composed of >99% alumina (Al_2O_3). The Nextel™ 610 fibers have been reported to contain approximately 0.35 wt% of SiO_2 , which inhibits grain growth [12, 139, 162]. Nextel™ 720 alumina-mullite fiber is composed of 85% alumina (Al_2O_3) and 15% silica (SiO_2) by weight. Each fiber tow contains 400 individual filaments with a diameter of 12 μm . From this data, a cross sectional area of $4.52 \times 10^{-8} \text{ m}^2$ was used for all engineering stress calculations. Both fiber tows were received on spools from the Air Force Research

Laboratory, Materials and Manufacturing Directorate. The specifications provided by the manufacturer are given in Table 6.

Table 6. Manufacturing Specifications for Nextel™ 610 and Nextel™ 720 Fiber Tows

	Nextel™ 610	Nextel™ 720
Denier	1500	1500
Sizing (organic coating)	324	299
Manufacturing date	3/14/2005	2/2/2006

Note that the organic sizing, which was applied to the fibers in order to keep the filaments of the tow together for handling purposes, was burned off of the gauge section of the fiber tow specimens during high-temperature testing.

3.1.2 Fiber Tow Test Specimens

In preparing the fiber tows for testing, excess lengths of tow were taken from the manufacturer's spool. Areas of the tow that contained obvious damage, to include broken filaments and spool edge sections, were discarded. Tows were then hung vertically from laboratory stands and soaked with alcohol in order to assist in straightening the tow. Once the alcohol was dry, each tow section was taped onto a cutting board utilizing grid lines for alignment. Fiberglass tabs were prepositioned seven inches apart on the grid section. A two part epoxy (Hardman Double Bubble Epoxy, 04001) or strain gage adhesive (M-Bond 200, Vishey) was then applied to the tow section

on top of the underlying tab, and a second fiberglass tab was applied in order to sandwich the tow and the epoxy between the fiberglass tabs. The two part epoxy was the preferred and predominantly used adhesive due to the durability and thickness of the epoxy. Once the adhesive was dry, the excess tow protruding beyond the tabs was trimmed. The final tow length measured between tabs was seven inches for all experiments.

For creep testing of the fiber tows, a centerline hole was punched in the fiberglass tabs to permit hanging the fiber tow specimen on the hook fixtures. The overall tab dimensions were 1.5 in. x 0.75 in. with the smaller sandwiching tab having dimensions of 0.75 in. x 0.75 in. Figure 10 depicts a tab end of a ceramic fiber tow specimen prepared for creep testing.

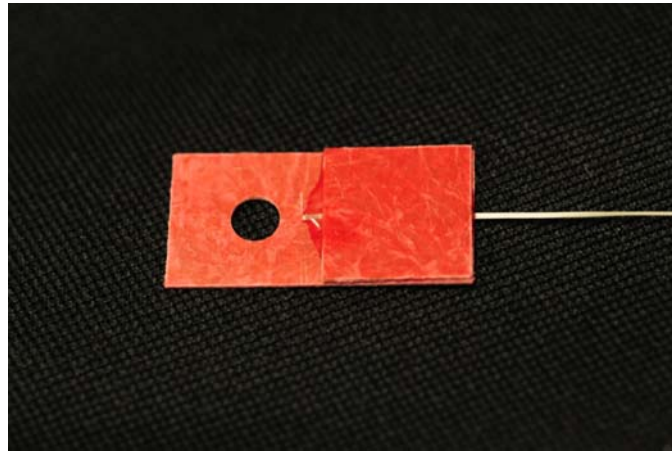


Figure 10. Tab for creep testing of ceramic fiber tow

For monotonic tension tests, fiberglass tabs were also used but the configuration and dimensions were different. Alignment shoulders on the hydraulic wedge grips were utilized for consistent specimen placement. Vertical lines were drawn on the fiberglass tabs at 5 mm from the edge to also assist in consistent alignment and to ensure that the

tow was positioned on the horizontal centerline of the hydraulic wedge grips. To facilitate specimen handling and the test set-up in the case of monotonic tension tests, larger fiberglass tabs were used for monotonic tensile test specimens. The horizontal dimension of the tabs for the monotonic tensile test specimens was 1.5 in., while the vertical dimension was 1.0 in. The smaller sandwiching tab was 1.0 in. x 1.0 in. Figure 11 depicts one tab end of a ceramic fiber tow specimen prepared for monotonic tension testing.

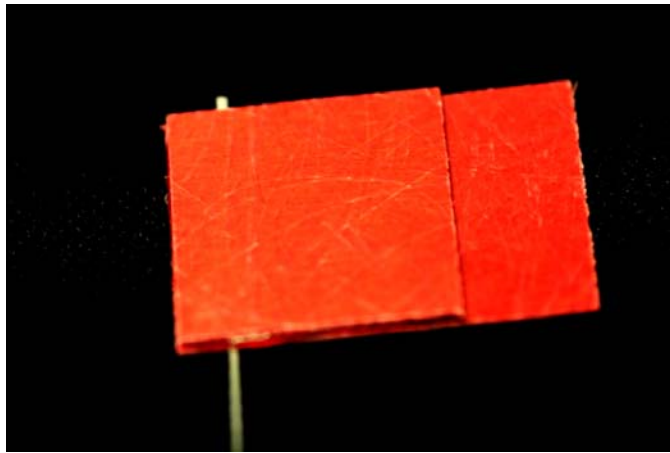


Figure 11. Tab for monotonic tension testing of ceramic fiber tow

3.1.3 Monolithic Alumina (Al_2O_3) and Yttrium Aluminum Garnet (YAG, $\text{Y}_3\text{Al}_5\text{O}_{12}$) Test Materials

High-purity polycrystalline yttrium aluminum garnet (YAG, $\text{Y}_3\text{Al}_5\text{O}_{12}$) and polycrystalline alumina (Al_2O_3) bulk specimens were processed by the Air Force Research Laboratory, Materials and Manufacturing Directorate.

The polycrystalline alumina billets were fabricated using commercially available alumina powder (AKP-53, Sumitomo, Inc.). Both the undoped alumina powder and the alumina powder with the addition of 0.14% SiO₂ were used. A spark plasma sintering unit was used to consolidate the powders into translucent billets. To achieve near theoretical density the powders were subjected to the processing conditions of 1300-1400°C/20 min./10-15 kN.

Polycrystalline YAG billets were fabricated using high purity (> 99.99%), nanosized YAG powder. Powders of YAG and of silica doped (0.14% SiO₂) YAG were produced by UES, Inc. using combustion synthesis process [80]. The powders were cold pressed into billets and then subjected to a sinter-hot isostatic press (HIP) process to consolidate the material to ~100% theoretical density [79]. The hot isostatic press process was conducted at 1500-1600°C under 30 ksi argon pressure and lasted 5-10 hours.

The fabricated billets were sectioned into test specimens using a diamond-impregnated blade. The specimen drawing is shown in Figure 12. After machining, the samples were mounted and lightly ground to ensure that the top and bottom faces of the rectangular prisms were parallel.

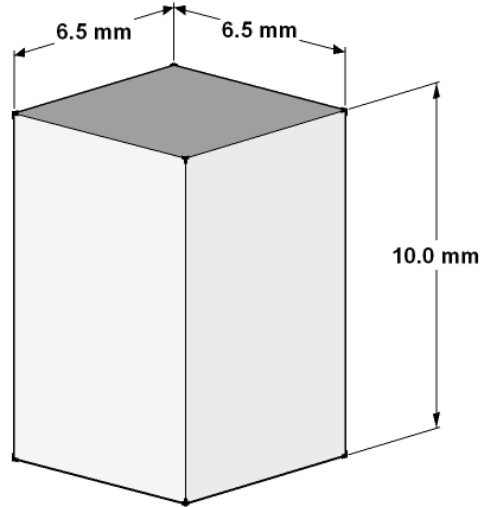


Figure 12. Compression creep specimen

3.1.4 YAG and Al_2O_3 Test Specimens

The high-purity single crystal YAG, polycrystalline YAG, and polycrystalline alumina specimens were machined for compression creep testing. Figure 13 depicts a polycrystalline YAG specimen (left) and a polycrystalline alumina specimen (right). The polycrystalline YAG specimens were grey whereas the polycrystalline alumina specimens were near white in appearance. Two batches each of polycrystalline YAG and polycrystalline alumina were processed for this study. One batch contained 0.14% SiO_2 as a sintering agent. These specimens will be referred to as silica doped specimens. The other batch was processed without SiO_2 . These specimens will be referred to as undoped specimens. The dimensions of the YAG and alumina test specimens are listed in Table 7 and Table 8, respectively. In the compression tests conducted on polycrystalline YAG and on polycrystalline alumina specimens the strain measurement had to be made by placing the extensometer rods not on the actual polycrystalline YAG and on

polycrystalline alumina specimens, but on the single crystal YAG pushrods. Therefore a strain ratio was calculated to correct for measuring strain off of the test specimen. This is discussed in detail in Section 3.3.2 yet is included in Table 7 and Table 8 for each specimen.

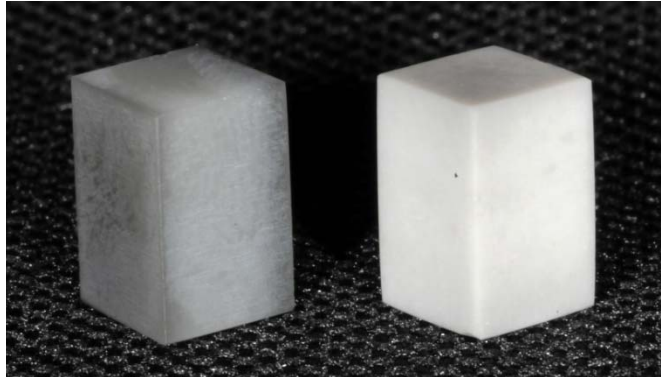


Figure 13. Polycrystalline YAG (left) and Polycrystalline Alumina (right)
Compression Specimens

Table 7. YAG Specimen Details

Specimen	Height (mm)	Width (mm)	Depth (mm)	Strain Ratio	Test Number	Notes
Single crystal YAG	19.56	6.63	6.40	N/A	Baseline Steam; 1300°C	
Polycrystalline YAG, SiO ₂ doped specimen 1	10.08	6.48	6.49	1.260	Test #1 Steam, 1300°C	
Polycrystalline YAG, SiO ₂ doped specimen 2	10.08	6.49	6.49	1.260	Test #2 Air, 1300°C	
Polycrystalline YAG, undoped specimen 3	10.03	6.50	6.51	1.266	Test #3 and #4 Steam, 1300°C	Test #3: heater failure
Polycrystalline YAG, undoped specimen 5	10.03	6.50	6.51	1.266	Test #5 Air, 1300°C	
Polycrystalline YAG, SiO ₂ doped specimen 6	10.10	6.52	6.48	1.257	Test #6 Steam, 1300°C	Test #6: heater failure
Polycrystalline YAG, undoped specimen 7	10.03	6.52	6.51	1.266	Test #7 Steam, 1300°C	
Polycrystalline YAG, SiO ₂ doped specimen 8	10.10	6.52	6.50	1.257	Test #8 Air, 1300°C	
Polycrystalline YAG, undoped specimen 9	10.03	6.50	6.51	1.266	Test #9 Air, 1300°C	
Polycrystalline YAG, SiO ₂ doped specimen 10	10.08	6.50	6.48	1.260	Test #10 Steam, 1300°C	

Table 8. Al₂O₃ Specimens Details

Specimen	Height (mm)	Width (mm)	Depth (mm)	Strain Ratio	Test Number	Notes
Dummy Al ₂ O ₃	10.15	7.04	7.72	1.252	Setup verification Steam; 1300°C	Specimen failed at 150 MPa
Polycrystalline Al ₂ O ₃ , undoped specimen 1	10.12	6.49	6.49	1.255	Test #1 Air, 1300°C	Lot A1 heater failure
Polycrystalline Al ₂ O ₃ , undoped specimen 2	10.12	6.49	6.49	1.255	Test #2 Air, 1300°C	Lot A1
Polycrystalline Al ₂ O ₃ , undoped specimen 3	10.05	6.50	6.50	1.264	Test #3 Steam, 1300°C	Lot A1
Polycrystalline Al ₂ O ₃ , SiO ₂ doped specimen 4	10.05	6.50	6.49	1.264	Test #4 Air, 1300°C	Lot S1
Polycrystalline Al ₂ O ₃ , SiO ₂ doped specimen 5	10.02	6.49	6.49	1.267	Test #5 Steam, 1300°C	Lot S1
Polycrystalline Al ₂ O ₃ , undoped specimen 6	10.11	6.49	6.49	1.256	Test #6 Steam, 1100°C	Lot A2
Polycrystalline Al ₂ O ₃ , undoped specimen 7	10.10	6.48	6.50	1.257	Test #7 Air, 1100°C	Lot A2
Polycrystalline Al ₂ O ₃ , SiO ₂ doped specimen 8	10.02	6.48	6.50	1.267	Test #8 Steam, 1100°C	Lot S1
Polycrystalline Al ₂ O ₃ , SiO ₂ doped specimen 9	10.04	6.50	6.46	1.265	Test #9 Air, 1100°C	Lot S2 power failure
Polycrystalline Al ₂ O ₃ , SiO ₂ doped specimen 10	10.03	6.50	6.45	1.266	Test #10 Air, 1100°C	Lot S2

3.2 Experimental Facility – Ceramic Fiber Tow Testing

The experimental facility for testing fiber tows at elevated temperature in air and in steam environment was designed and assembled in the Mechanics of Advanced Aerospace Materials Laboratory of the Department of Aeronautics and Astronautics at the Air Force Institute of Technology. Additionally, the methods for testing ceramic fiber tows under monotonic tension and creep loadings at elevated temperature in air and in steam environments were developed.

It has been established that the tensile strength of ceramic fiber tows is generally less than the mean strength of fiber filaments [13, 28, 30, 93]. Nevertheless, as was discussed in Section 2.4, steady-state creep rates are the same between fiber tows and single filaments. Furthermore, it was concluded that because composites utilize fiber tows, the experiments conducted on fiber tows were more representative of the actual service conditions than those conducted on single filaments.

Additionally, Dassios et al. [30] and Calard et al. [13] also concluded that experiments conducted on fiber tows were more representative of actual composites containing the fiber tows rather than single filaments. These results and observations support the decision to investigate the creep response of fiber tows rather than that of the single filaments in this work.

The creep and monotonic tension performance of Nextel™610 and Nextel™720 fiber tows were investigated in air and in steam at the respective maximum operating temperatures of 1100°C and 1200°C. Additional testing of Nextel™720 fiber tows was conducted at 1100°C. Monotonic tensile tests were performed at various loading rates in order to evaluate the effect of loading rate on tensile strength in air and in steam. Creep

experiments were performed from 100 to 500 MPa in order to establish dependence of creep behavior on the applied stress. Creep run-out was set to 100 hours. All creep tests were performed in air and in steam in order to evaluate the effects of steam environment on creep behavior. In each test, load-displacement data were recorded during the initial heating, during loading to the creep stress level, and during the actual creep period. Thus applied stress, thermal strain, the total mechanical strain, and the creep strain could be calculated and examined. In all tests, a heating rate of 1.0°C/s was used, and the targeted temperature was maintained for a minimum of 45 minutes before beginning each test in order to achieve thermal equilibrium. During heat-up and heat-soak each specimen was subjected to a small weight of 10 to 20 grams in order to keep the fiber tow taut. It is noteworthy that in all tests the failures occurred in the heated gauge section of the specimen. Analysis of the experimental data provided insight into the creep and the environmental degradation occurring in the fiber tows at elevated temperatures.

3.2.1 Testing Facility

An experimental facility for testing fiber tows at elevated temperature in air and in steam environments was designed and configured at AFIT. An MTS Landmark™ 370.02 test system, shown in Figure 14, was the primary load frame utilized for testing of the fiber tows in monotonic tension. An MTS FlexTest 40 digital controller was used for input signal generation and for data acquisition in monotonic tensile testing as well as in creep testing.

High temperature environment was provided by an MTS 653.03A two-zone furnace, shown in Figure 15, with silicon carbide heating elements and two R-type

control thermocouples, which supplied feedback to an MTS 409.83 temperature controller. The furnace had a 3.5 inch (90 mm) hot zone. Temperature profiles were measured throughout the length of the furnace using an S-type thermocouple. Once the temperature profile throughout the length of the furnace was established, an effective gauge length of the fiber tow specimen was calculated, which enabled the calculation of engineering strain from recorded displacement measurements. This technique is discussed in detail in Section 3.2.4.

All tests on fiber tows employed an alumina susceptor (ceramic tube with endcaps) designed to fit inside the furnace. The susceptor allowed heat transfer from the heating elements to the fiber tow, while protecting the interior of the furnace, the heating elements and control thermocouples from the degrading effects of steam environment. Initially, the use of the susceptor was intended only for the steam experiments. However, the use of the susceptor resulted in a more uniform and repeatable temperature distribution along the fiber tow specimen. Therefore the susceptor was used for all fiber tow testing. The gauge section of the fiber tow specimen was located inside the susceptor with the ends of the fiber tow specimen passing through slots in the susceptor end caps. Additionally, a hole was cut in the side of the susceptor in order to inject steam through a feeding tube. Figure 16 shows the susceptor set in one half of the furnace with the steam injection tube entering the susceptor at the bottom and a fiber tow specimen suspended from an extendable fixture of the creep test setup.

A model HGA-H from MHI steam generator (see Figure 17) generated steam at 50 mL/hr using deionized water. Steam was supplied to the susceptor through a ceramic feeding tube (see Figure 16) in a continuous flow with a slightly positive pressure,

expelling the dry air and creating a very high partial pressure of water inside the susceptor. This steam-rich environment was easily observable by the condensation on components above the furnace. However, no condensation was observed below the furnace due to vertical convection within the susceptor.



Figure 14. MTS LandmarkTM servo-hydraulic test system

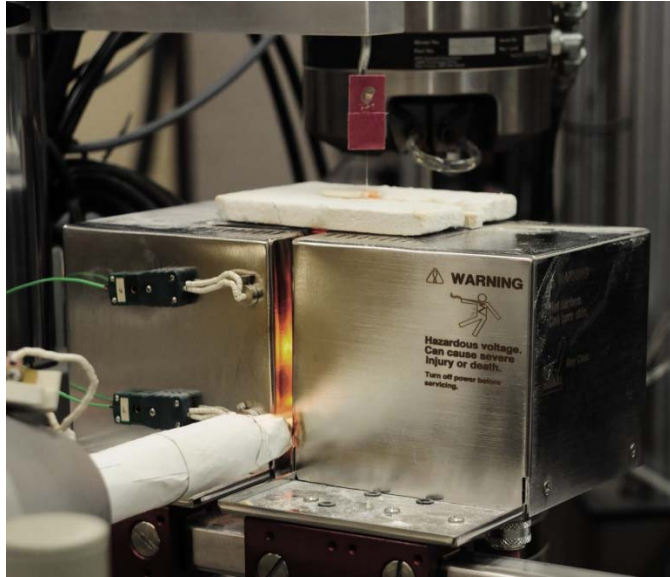


Figure 15. MTS 653.03A two-zone furnace used for fiber tow testing



Figure 16. Experimental setup for creep testing of fiber tows with susceptor and steam feeding tube

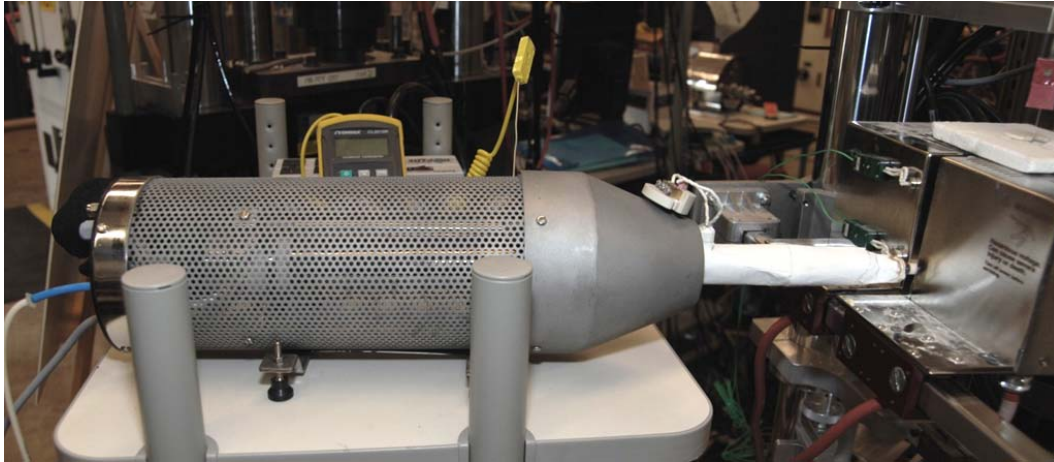


Figure 17. Steam Generator

The initial design of the susceptor had the steam port located at the vertical midpoint of the susceptor. Initial creep tests of NextelTM 610 fiber tows in steam were conducted with this initial susceptor design (i.e. steam port located at the vertical midpoint). After a few initial tests, it was recognized that the convection effects within the susceptor caused the steam to rise inside the susceptor and exit at the top of the susceptor. As a result, the lower half of the gauge section of the fiber tow specimen was not subjected to the steam environment. Hence the susceptor design was improved by relocating the steam port to the bottom of the susceptor. All subsequent testing of NextelTM 610 and NextelTM 720 fiber tows was conducted using the susceptor with the steam port located at the bottom of the susceptor.

The fiber tows were subjected to two types of tests: monotonic tension and tensile creep. The servohydraulic MTS LandmarkTM test system was used to perform the monotonic tension tests. The fiberglass tabs mounted at the ends of the specimen were gripped in the MTS 647.02B hydraulic wedge grips. In conjunction with careful specimen preparation, alignment lines and edge stops of the hydraulic grips aided in

achieving a repeatable gripping process. The wedge grips were actively water cooled using a recirculation chiller, model NESLAB RTE-7, made by Thermo Fisher Scientific. Force measurements were obtained with an MTS force transducer, model 661.11B-02. Displacement measurements were made using the MTS LandmarkTM test system internal displacement transducer.

Initially it was planned to utilize the servohydraulic MTS LandmarkTM testing machine for creep experiments as well. As the desired creep stresses were estimated, the corresponding tensile loads could be readily calculated as ranging from 1 to 5 lbf. Preliminary tests were performed at room temperature and at 1100°C with the purpose of evaluating signal noise in the testing system when the constant loads of the desired magnitude were maintained. An example of a preliminary test performed at room temperature at a constant load of 4 lbf is shown in Figure 18, where the load command signal (solid line) and the load feedback signal (symbols) are plotted vs. time. Noise of ± 0.03 lbf in the feedback signal is evident. Such noise level is still acceptable. However, the picture changes dramatically once a similar test is performed at 1100°C. Figure 19 shows results of a preliminary test performed at 1100°C at a constant load of 3 lbf. In this case, the noise in the feedback signal increases by one order of magnitude to ± 0.3 lbf. Such level of noise in the feedback signal is unacceptable for experiments conducted with the constant load of 1-5 lbf. Therefore, a dead weight setup was developed for creep testing of the ceramic fiber tows at elevated temperatures in air and in steam. It should be noted that the response of the servohydraulic MTS LandmarkTM testing system in constant load rate monotonic tension tests was perfectly acceptable.

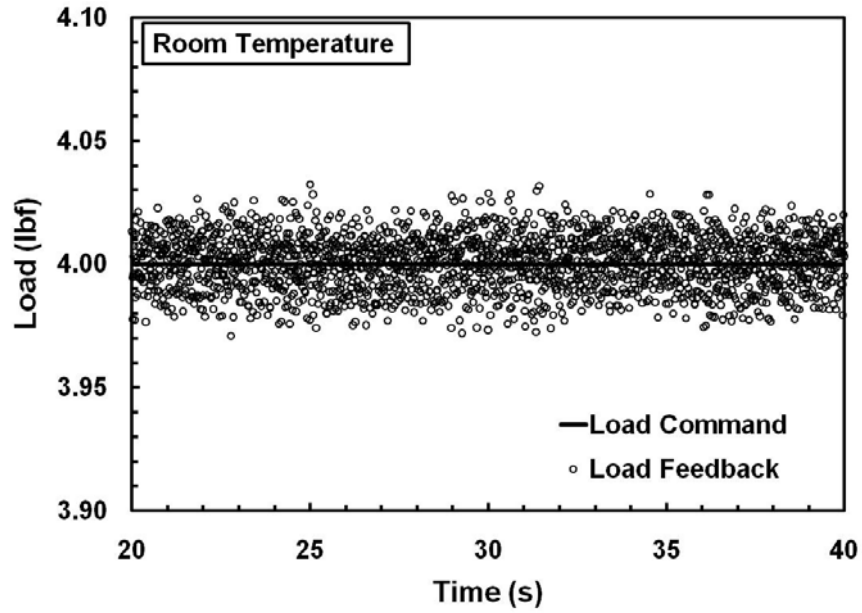


Figure 18. Load command signal (solid line) and load feedback signal (symbols) vs. time for Nextel™ 610 fiber tow at room temperature

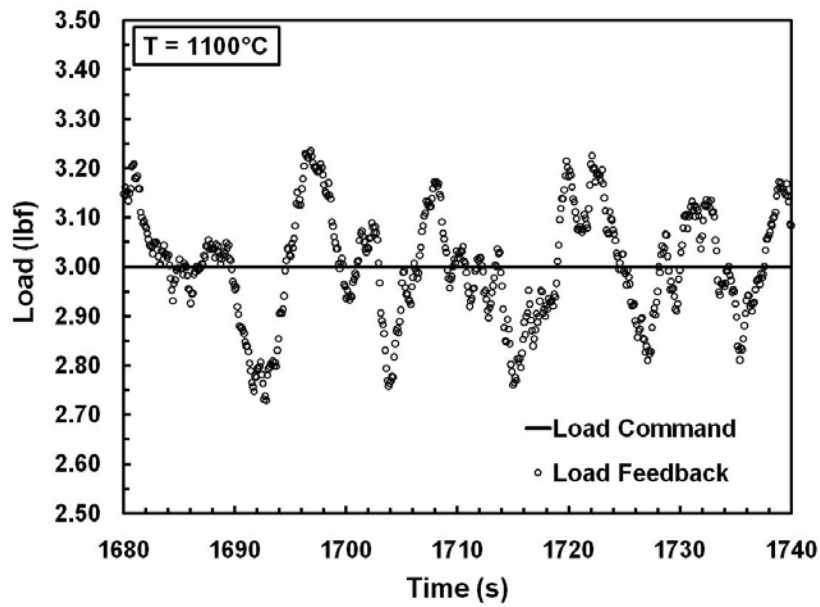


Figure 19. Load command signal (solid line) and load feedback signal (symbols) vs. time for Nextel™ 610 fiber tow at 1100°C

A dead weight setup was developed for creep testing of the ceramic fiber tows at elevated temperatures in air and in steam. The same furnace as that used for the monotonic tension tests was employed for creep testing. The furnace mounting rails were designed to rotate between the servohydraulic testing machine and the dead weight creep testing facility without vertical adjustment. Two extendable fixtures for suspending the test specimens were built specifically for the dead weight creep testing facility. The upper fixture contained a hook for hanging the upper tab of the specimen. The lower fixture held a Schaevitz M12-30 LVDT, which measured the elongation of the fiber tow specimen. The LVDT extension rod hooked onto the bottom tab of the fiber tow specimen. A second LVDT extension rod extended from the bottom of the LVDT core and contained nuts and washers at the bottom for applying the desired load. Finally, a hand-driven screw elevator was constructed to slowly apply the load to the fiber tow specimen. Slow application of the load is essential as it prevents damage to the tow during the initial loading. Figure 20 shows a fiber tow specimen mounted in the dead weight creep testing facility. The fiber tow specimen is suspended from the upper fixture hook through the furnace. The hydraulic grips that were used for monotonic tension setup are seen in the background of Figure 20 but are not utilized in the creep test setup. The LVDT is held by a phenolic block mounted on the end of the lower fixture, and the weights are stacked on the LVDT lower extension rod.

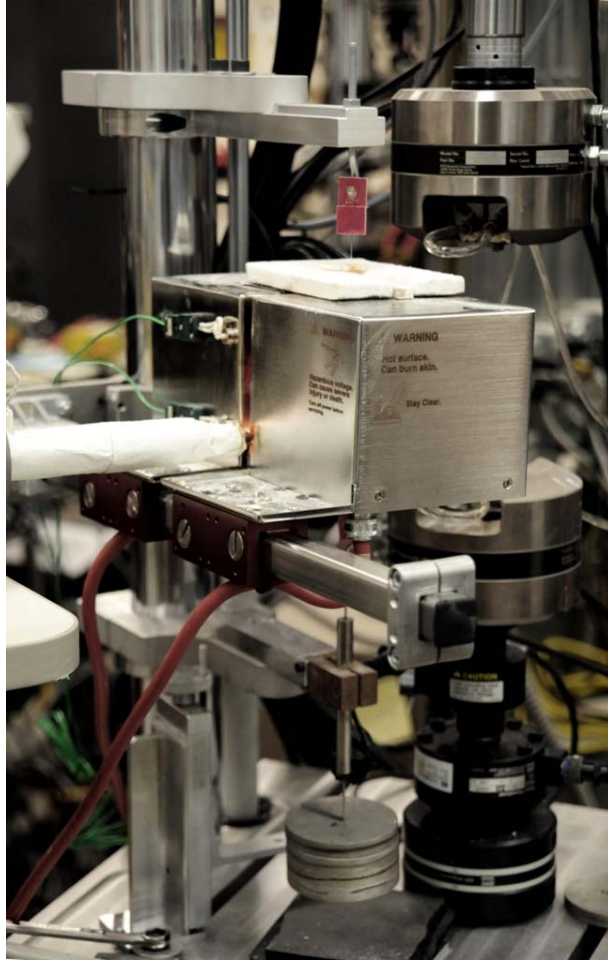


Figure 20. Fiber tow specimen mounted in the dead weight creep testing facility with hydraulic grips seen in the background

3.2.2 Facility Verification – Room Temperature Stress-Strain Chart

The tensile stress-strain behaviors of Nextel™ 610 and Nextel™ 720 fiber tows were evaluated at room temperature in laboratory air for comparison and validation purposes. Figure 21 shows the room temperature stress-strain curves obtained for Nextel™ 610 and Nextel™ 720 fiber tows. The modulus of elasticity values for Nextel™ 610 and Nextel™ 720 fiber tows were 320 GPa and 267 GPa, respectively. Wilson and Visser

reported a stiffness of 373 GPa for the single filament of Nextel™ 610 and 260 GPa for the single filament of Nextel™ 720 [163]. Likewise, Hammond reported the modulus of elasticity of 355 GPa for Nextel™ 610 fiber tow [49]. Additionally Deléglise, et al. reported an average stiffness for Nextel™ 720 of 251 GPa over various gauge lengths [33]. The current results compare well with previously published results and provide a measure of confidence in the current experimental facility design.

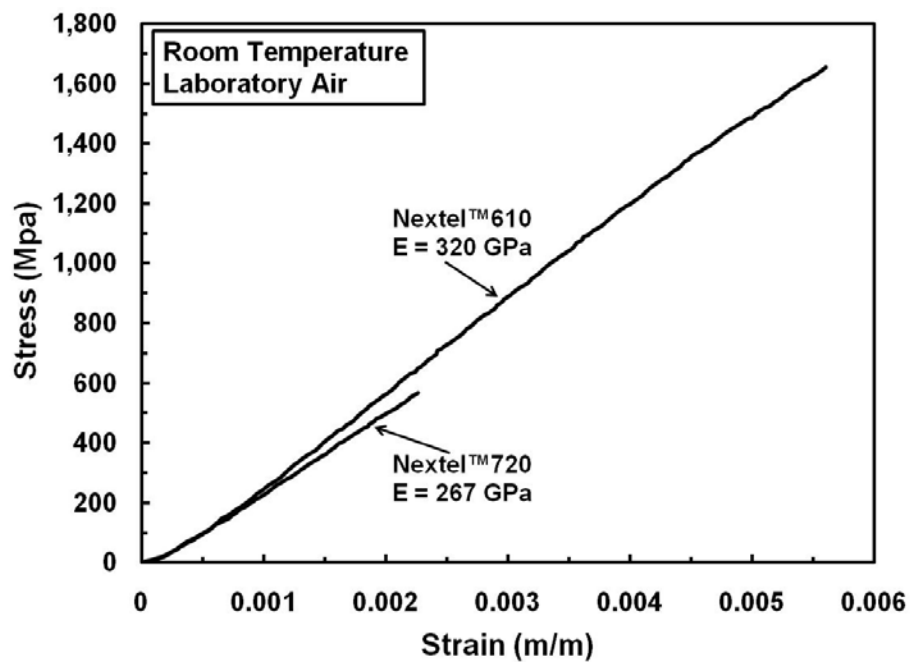


Figure 21. Tensile stress-strain curves for Nextel™ 610 and Nextel™ 720 fiber tows obtained at Room Temperature in laboratory air

3.2.3 Temperature Profiles

Temperature profiles for fiber tow testing were determined by measuring the temperature vertically along the centerline of the furnace with an S-type thermocouple. The S-type thermocouple was approximately 6 inches in length and comprised of an unshielded tip with ceramic insulation along the lead wires. A CL3515R model thermometer was used for temperature readings. The accuracy of these components was $\pm 1.5^{\circ}\text{C}$ for the S-type thermocouple and $\pm 1.5^{\circ}\text{C}$ for the thermometer. During the temperature measurements, the thermocouple was attached to a small aluminum block, which was mounted in the upper grip of the servo-hydraulic machine. This allowed for convenient probing throughout the furnace along the length of the fiber tow specimen.

In order to improve thermal insulation of the furnace and to shield the upper grip and specimen tab, a 0.5-in. thick piece of oxide insulation board was placed on top of the furnace. Additionally, the ceramic susceptor tube was used inside the furnace for all tests, both air and steam, in order to generate a more uniform and symmetric temperature profile. The susceptor was heated by the four silicon carbide heating elements in the MTS 653.03A furnace and radiated circumferentially around the furnace centerline, which reduced undesirable temperature variations along the center line of the furnace where the fiber tow specimen was located.

In order to determine the furnace controller temperature setpoints, the thermocouple was positioned in the center of the furnace as the temperature was increased. To obtain the desired temperature setpoints of the upper and lower temperature controllers, an iterative process was performed by moving the thermocouple up and down from the center point of the furnace and adjusting the setpoints. The

heating elements and furnace control couples were approximately 6 cm apart vertically. Therefore, initial observations of the temperature profile were obtained in the vertical region located within ± 3 cm from the center of the furnace. Once the desired setpoints for the temperature controllers were determined, a detailed temperature profile was measured by taking measurements every 5 mm along the vertical axis of the furnace starting just below the bottom of the furnace and ending just above the top of the furnace. Temperature profiles obtained for 1100°C and 1200°C in air are provided in Figure 22 and those obtained in steam are shown in Figure 23. The temperature controller setpoints determined for each profile are also shown. Due to the vertical heat convection within the furnace, the larger of the two setpoints for a given profile was for the lower control zone of the furnace. Additionally, the stable peak temperature profile across a broad range of the furnace was very desirable for consistent specimen gauge length calculations, which are described in Section 3.2.4. Note, the “dips” in the temperature profiles in Figure 23 correspond to the locations where the steam was injected into the susceptor.

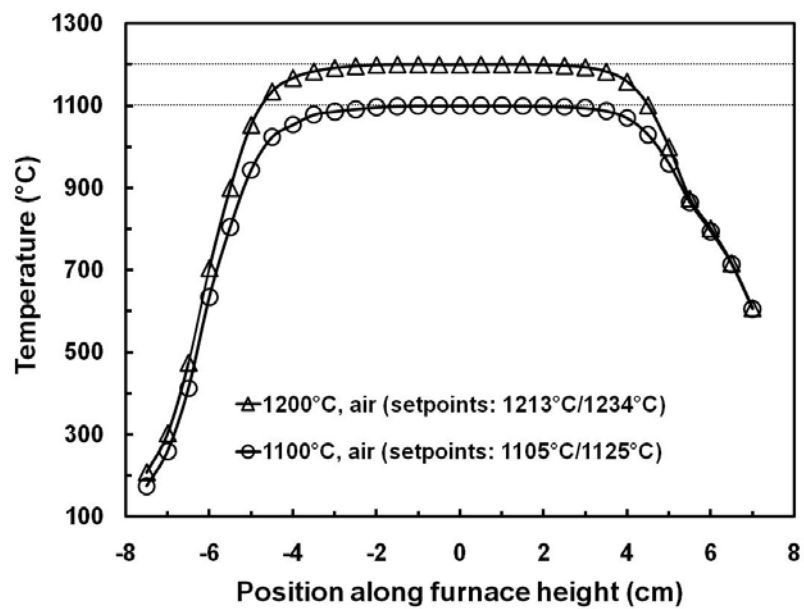


Figure 22. Temperature profiles obtained at 1100°C and at 1200°C in air (positive position corresponds to the top of furnace)

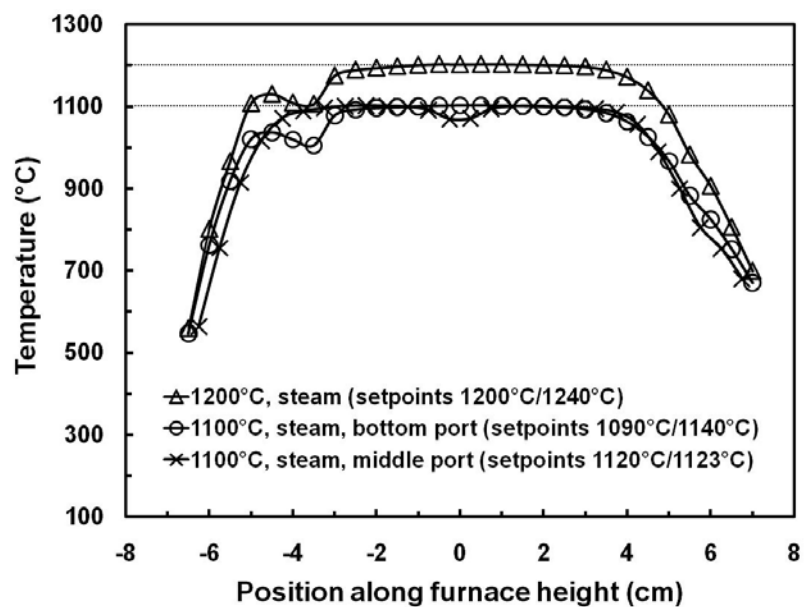


Figure 23. Temperature profiles obtained at 1100°C and at 1200°C in steam (positive position corresponds to the top of furnace)

Additional temperature measurements were taken in order to verify that the temperature settings were the same for the fiber tow specimen installed in the load frame and for the fiber tow specimen installed in the dead weight creep testing facility. Temperature measurements made with a handheld device outside the furnace showed a slightly lower temperature than was recorded from the detailed temperature profile. Nevertheless, temperature measurements taken inside the furnace with a fiber tow specimen installed confirmed that the temperature along the specimen inside the furnace was equivalent to the detailed temperature profile. Since the percentage of strain produced outside the furnace will be shown in Section 3.2.4 to be insignificant compared to the strain produced in the specimen gauge section located inside the furnace, the lower temperature measured outside the furnace was considered inconsequential.

3.2.4 Strain Measurement

Due to the impracticality of obtaining strain measurements by placing a measurement device directly on a bundle of fibers inside a furnace, an indirect method of obtaining strain measurements was necessary. Extension of the fiber tow specimen was measured outside the furnace by linear variable displacement transducers (LVDT in the direction of the load train along the fiber tow. The initial strain measurements were calculated using the effective gauge length described below and the average displacement value of the fiber tow length upon thermal equilibrium during the heat-soak. Machine compliance correction was accomplished for each test during post-processing by subtracting the strain value immediately upon the load application from the subsequent strain data.

An indirect method was utilized to calculate strain and the strain rate of the specimen in the hot test section. Extension of the fiber tow specimen was measured outside the furnace by linear variable displacement transducers and consisted of an amalgamation of extensions produced over the entire specimen length throughout the temperature profile. In order to convert the LVDT measurement into a representative strain at the desired test temperature, the amount of displacement along the length of the test specimen subjected to the temperature profile must be determined. Consider that the section of a fiber tow specimen subjected to a specific load at a higher temperature would displace more than another section of the same fiber tow specimen subjected to the same load but at a lower temperature in the temperature profile. In order to convert the overall displacement of the fiber tow specimen to strain at the desired temperature, the distribution of displacement along the temperature profile must be established. The method for calculating strain and strain rate from displacement measurements proposed below is similar to that of Morrell [100], Kandil and Dyson [65], and DiCarlo [34]. This calculation of the effective gauge length takes into account the varying compliance along the fiber tow subjected to a temperature profile.

Consider a test specimen of constant cross section with a length $2L$. From the center of the specimen gauge section, creep occurs over a total length $-L$ to L . Beyond these boundaries creep is negligible. Therefore, the total measured strain and total measured strain rate are:

$$\varepsilon_m = \frac{\Delta l}{2L} = \int_0^t \dot{\varepsilon}_m dt \quad (4)$$

$$\dot{\varepsilon}_m = \frac{\text{measured extension rate}}{2L} = \frac{1}{2L} \int_{-L}^L \dot{\varepsilon} dl \quad (5)$$

Note that the total measured strain and strain rate account for variations in strain and strain rate along the specimen subject to a temperature profile. At the hottest sections, the amount of strain or strain rate will be greater than at a lower temperature.

Now, consider the strain and strain rate at the desired maximum temperature at the center of the furnace. Let subscript *O* denote quantities obtained at the center of the specimen gauge section. The strain at the center of the furnace can be calculated as the time integral of the strain rate at the center of the furnace. It can also be described by the same overall change in length of the entire specimen divided by a hypothetical length called the effective gauge length, $(2L)_{eff}$. The effective gauge length can also be thought of as the gauge length obtained under a hypothetical step-function temperature profile, in which all the strain was accumulated under the peak temperature and zero strain is achieved under the lower temperature.

$$\varepsilon_o = \int_0^t \dot{\varepsilon}_o dt = \frac{\Delta l}{(2L)_{eff}} \quad (6)$$

Similarly, the strain rate at the maximum temperature (i.e. strain rate at the center of the furnace) can be expressed by using the effective gauge length as:

$$\dot{\epsilon}_o = \frac{\text{measured extension rate}}{(2L)_{eff}} = \frac{1}{(2L)_{eff}} \int_{-L}^L \dot{\epsilon} dl \quad (7)$$

Taking the ratio of Equations 5 and 7 obtain:

$$\frac{\dot{\epsilon}_m}{\dot{\epsilon}_o} = \frac{(2L)_{eff}}{2L} \quad (8)$$

Recall the general power-law creep equation given in Equation 3 and reproduced here considering that stress is uniform and that temperature is a function of location along the fiber tow specimen:

$$\dot{\epsilon} = A\sigma^n \exp\left(\frac{-Q}{RT(l)}\right) \quad (9)$$

Using Equations 5, 8 and 9, the ratio of the measured strain rate to the actual strain rate becomes only a function of temperature, given by:

$$\frac{\dot{\epsilon}_m}{\dot{\epsilon}_o} = \frac{1}{2L} \int_{-L}^L \exp\left\{\frac{-Q}{R}\left(\frac{1}{T(l)} - \frac{1}{T_o}\right)\right\} dl \quad (10)$$

Utilizing a numerical summation of increments of length h , such that $L = kh$ where k is an integer, the ratio of the measured strain rate to the actual strain rate is

$$\frac{\dot{\epsilon}_m}{\dot{\epsilon}_o} = \frac{1}{2k} \sum_{i=-k}^k \exp \left\{ \frac{-Q}{R} \left(\frac{1}{T_i} - \frac{1}{T_o} \right) \right\} \quad (11)$$

As a result, an effective gauge length can be calculated such that:

$$(2L)_{eff} = 2L \left(\frac{\dot{\epsilon}_m}{\dot{\epsilon}_o} \right) \quad (12)$$

The effective gauge length can be used to calculate strain as well as strain rate from displacement measurements made outside the hot zone of the furnace.

Using this approach together with the temperature profile established in Section 3.2.3, and creep activation energy of 644 kJ/mol from literature [49], an effective gauge length of 6.64 cm was calculated for Nextel™ 610 fiber tow specimens at 1100°C in air. In a similar manner, utilizing a creep activation energy of 702 kJ/mol from literature [32], effective gauge lengths of 6.52 cm and 6.83 cm were calculated for Nextel™ 720 fiber tow specimens in air at 1100°C and 1200°C, respectively. Figure 24 and Figure 25 schematically show the effective gauge lengths of the Nextel™ 610 and Nextel™ 720 fiber tow specimens next to the respective temperature profiles. Similarly, effective gauge lengths were calculated for testing in steam environment. Recall that two different designs of the susceptor were used for testing in steam. The initial design had the steam port located at the vertical midpoint, while the final design had the steam port located at the bottom of the susceptor. The bottom location of the steam port was preferred since it exposed the entire gauge section of the specimen to the steam-rich environment. Figure

26 and Figure 27 schematically depict the effective gauge lengths and the temperature profiles obtained for the Nextel™ 610 fiber tow specimens at 1100°C in steam for the initial and final susceptor designs, respectively. From experimental observations, it was concluded that once the steam entered the susceptor it was rapidly heated and flowed vertically. Therefore, the lower half of the fiber tow specimen in Figure 26 was not exposed to the steam rich environment. Furthermore, the effective gauge length for Nextel™ 720 fiber tow specimens at 1100°C in steam is depicted in Figure 27. Figure 28 schematically shows the effective gauge length and the temperature profile obtained for the Nextel™ 720 fiber tow specimens at 1200°C in steam. Note that in this case, the final susceptor design is used, with the steam port located at the bottom of the susceptor. It is interesting to note that the sensitivity of the effective gauge length over reasonable ranges of creep activation energies was very minor. That is, differences in the calculated effective gauge lengths were very small for various creep activation energies. This difference had an even less significant effect on the creep strain rates. Therefore, the effective gauge lengths for each temperature and environmental condition were considered constant as reported here.

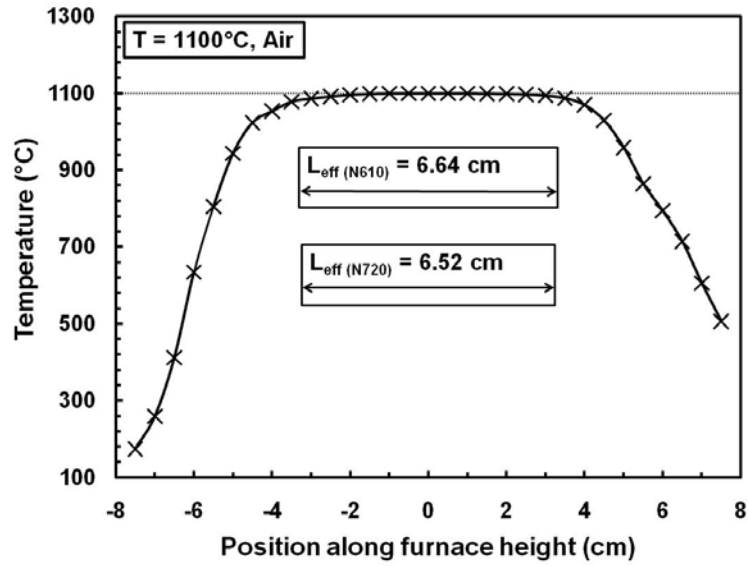


Figure 24. Schematic representation of the effective gauge length for the Nextel™ 610 and 720 fiber tow specimens at 1100°C in air

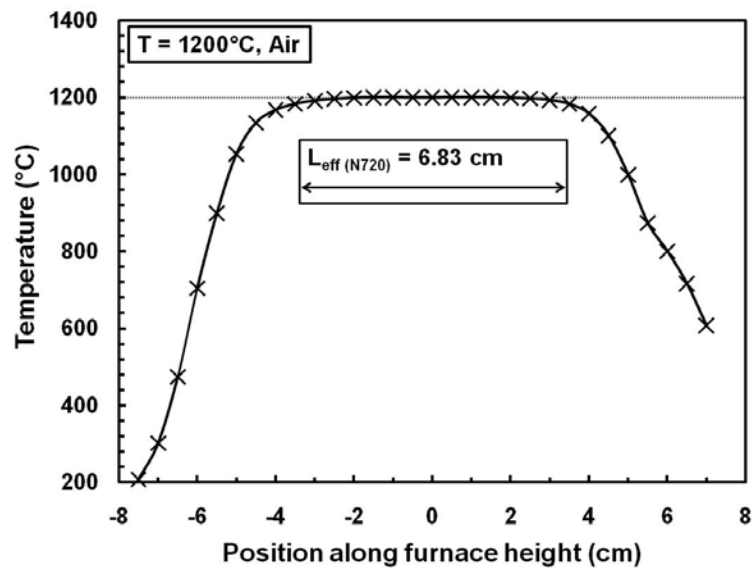


Figure 25. Schematic representation of the effective gauge length for the Nextel™ 720 fiber tow specimen at 1200°C in air

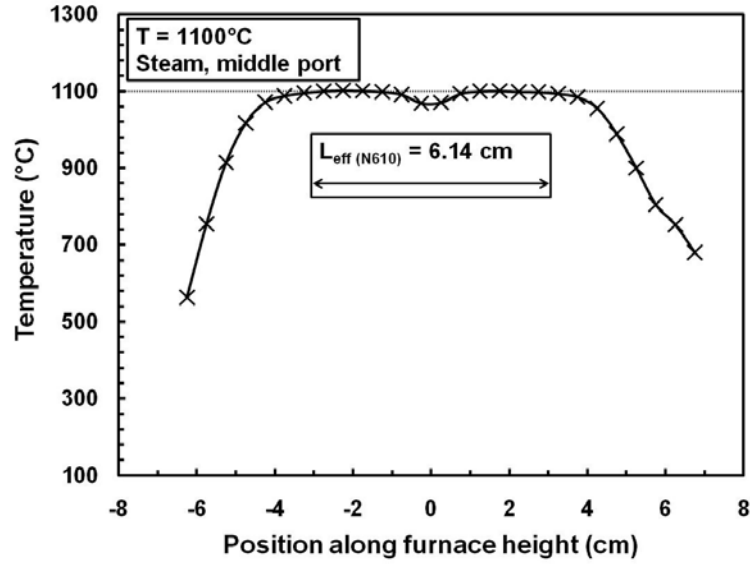


Figure 26. Schematic representation of the effective gauge length for the Nextel™ 610 fiber tow specimen at 1100°C in steam. Steam port is located at the vertical midpoint of the susceptor.

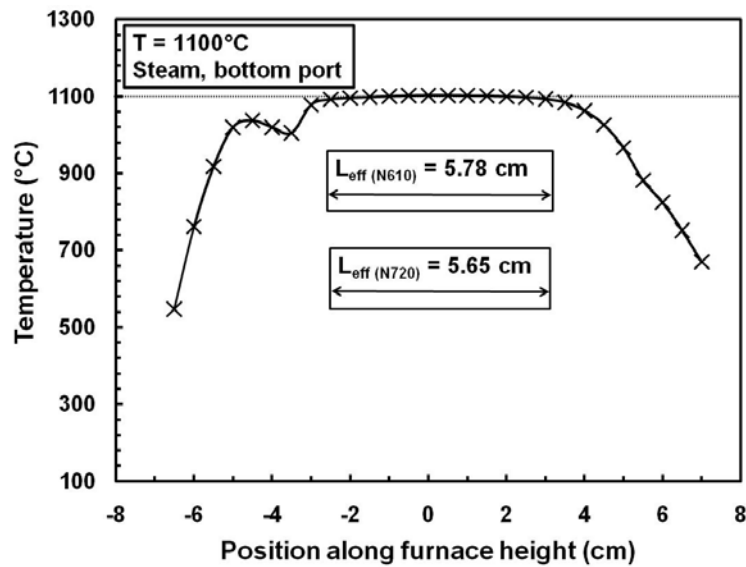


Figure 27. Schematic representation of the effective gauge length for the Nextel™ 610 and 720 fiber tow specimens at 1100°C in steam. Steam port is located at the bottom of the susceptor.

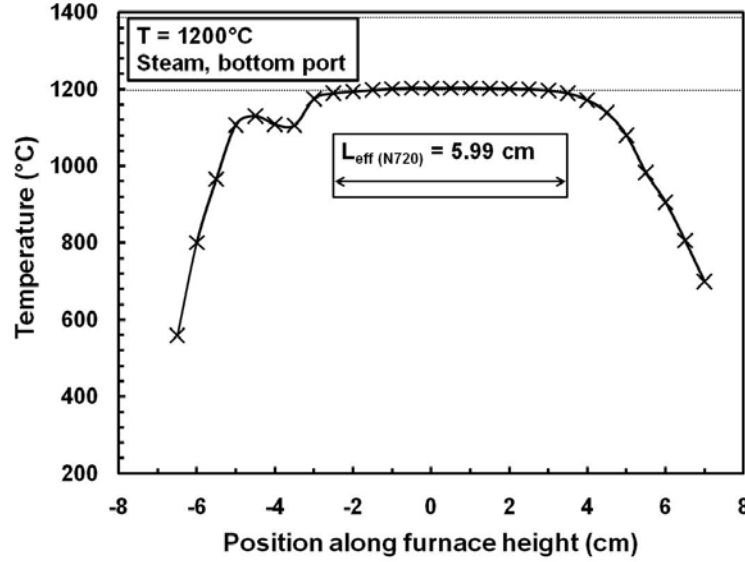


Figure 28. Schematic representation of the effective gauge length for the Nextel™ 720 fiber tow specimen at 1200°C in steam. Steam port is located at the bottom of the susceptor.

Hammond [49] and Yun, et al. [165] applied a simpler approach by assuming the main creep deformation occurred only in the hot zone of the furnace and approximated the gauge length by the flat portion of the temperature profile. This approach is subjective in defining the gauge length of the specimen and is dependent on how flat the maximum temperature profile was and how sharply the temperature drops at the edges of the furnace – the flatter and sharper, the better the estimate.

The calculated effective gauge lengths presented above are physically representative of the flat portion of the temperature profile. Furthermore, notice that the effective gauge lengths essentially compensates for changes in the temperature profile, like the inflow of steam as depicted by the dips in the profiles, and also by taking into account the creep activation energy of the different fiber tows. Using this calculated effective gauge lengths is a much more systematic approach to obtaining strain from

extension measurements for a specimen subjected to a temperature profile regardless of the shape of the profile.

3.3 Experimental Facility – Compression Creep Testing

In addition to evaluating the effects of steam on high-temperature creep resistance of the Nextel™ 610 and Nextel™ 720 fiber tows, this research assessed the feasibility of polycrystalline yttrium aluminum garnet (YAG, $\text{Y}_3\text{Al}_5\text{O}_{12}$) as a candidate oxide fiber material for next-generation high-temperature CMCs. To achieve this objective, the compressive creep performance of high-purity polycrystalline YAG and polycrystalline alumina were investigated at elevated temperatures in air and in steam. Additionally, creep testing was also performed on high-purity single crystal YAG for validation of the experimental setup which utilized single crystal YAG pushrods. Creep results for the single crystal YAG specimen are presented and discussed in Section 3.3.3.

For the comparison of creep results of fibers to bulk materials, Lavaste et al. [77] observed that creep rates and mechanisms of alumina based fibers are similar to those of bulk materials with similar grain sizes. In addition, Chokshi [23] reports a number of creep comparisons between tension and compression loading of polycrystalline alumina with only slight differences. Therefore, comparisons between creep of fibers and bulk materials are made in this work. However, the large differences in grain sizes and underlying creep mechanisms of the fiber and bulk materials must be kept in mind.

The compressive creep stresses for polycrystalline alumina at 1100°C ranged from 100 to 250 MPa. Furthermore, the compressive creep stresses for polycrystalline alumina and YAG at 1300°C ranged from 50 to 200 MPa. In all tests, stress-strain data

were recorded during heating, during loading to the creep stress level, and during the actual creep period. In all tests, a specimen was heated to either 1100 or 1300°C at the rate of 0.5°C/s and then maintained the targeted temperature for 1 hour in order to achieve thermal equilibrium. During the heat-up and 1-hour soak, each specimen was subjected to a small compressive pre-load of 100 lbf. Following a 1-hour soak at temperature, the specimens were loaded to the creep stress level at the stress rate of 15 MPa/s. Several compressive stresses of increasing magnitude were applied to each specimen in order to achieve various creep stress levels with the limited number of specimens. Each compressive stress level was maintained for 3 to 5 hours. In all tests, specimen failure did not occur when the test was interrupted.

Compressive creep experiments were performed at 1300°C at various creep stress levels in order to establish dependence of creep behavior on applied stress and to measure the steady-state creep rates. In order to evaluate effects of steam environment on compressive creep behavior of the polycrystalline YAG and of the polycrystalline alumina, all creep experiments were performed in laboratory air and in steam. The analysis of the experimental data provided new insight into the creep and the environmental degradation mechanisms occurring in the polycrystalline YAG and in the polycrystalline alumina. Based on these findings, the feasibility of developing polycrystalline YAG fibers for use in the next-generation CMCs was assessed.

3.3.1 Testing Facility

It was recognized that the bulk YAG and alumina (Al_2O_3) specimens used in this work did not lend themselves to testing in tension. Therefore, creep testing of the

monolithic YAG and Al_2O_3 was conducted in compression. An experimental facility for testing the high-purity bulk YAG and Al_2O_3 specimens in compression at 1300°C in air and in steam environment was designed. The experimental setup utilized a servo-hydraulic MTS 810 mechanical testing machine equipped with water-cooled MTS 647.02B hydraulic wedge grips, shown in Figure 29. This testing system had a test load capacity up to 5,500 lbs (25 kN). An MTS FlexTest 40 digital controller was used for all input signal generation and data acquisition.

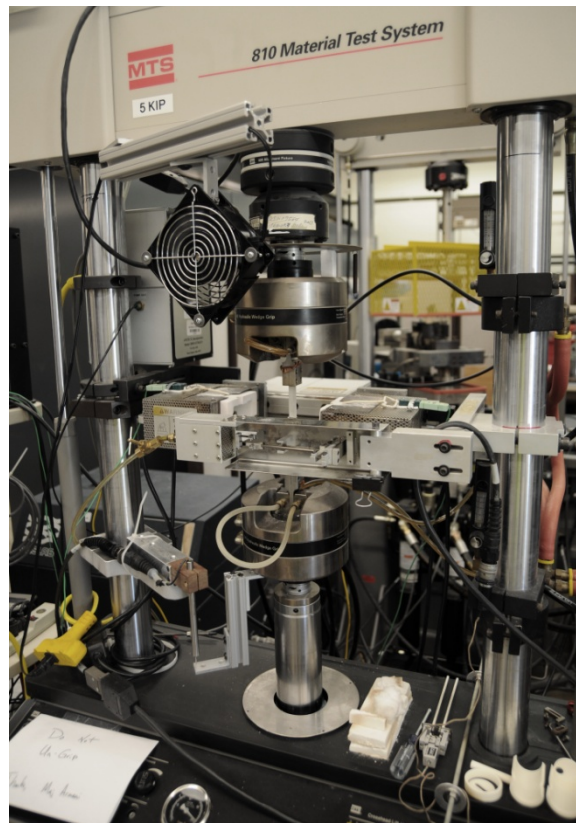


Figure 29. MTS 810 servo-hydraulic test system

An AMTECO Hot Rail compact two-zone resistance-heated furnace, which contained two silicon carbide heating elements and two R-type control thermocouples,

and MTS 409.83 temperature controllers were used for elevated temperature testing. In order to improve thermal insulation of the furnace and to shield the upper grip and fixture, a 0.5-in. thick piece of oxide insulation board was placed on top of the furnace. An alumina susceptor (a tube with endcaps), which fits inside the furnace, was designed and fabricated specifically for compression testing of the YAG specimens at elevated temperature in air and in steam. The susceptor allowed heat transfer from the heating elements to the specimen, while protecting the interior of the furnace, the heating elements and the thermocouples from the degrading effects of steam environment. Initially, the use of the susceptor was intended only for experiments performed in steam. However, the use of the susceptor resulted in a more stable and repeatable temperature profile on the specimen. Therefore the susceptor was used in all tests. The steam entered the susceptor through a feeding tube inserted into the back end cap of the susceptor. The extensometer rods were inserted into the susceptor through a groove in the front end cap. Figure 30 shows the susceptor with the steam injection tube in the rear and extensometer mounted in the front.

An AMTECO HRFS-STMGEN steam generator using de-ionized water generated the steam at 35 mL/hr. Steam was supplied to the susceptor through a ceramic feeding tube in a continuous flow with a slightly positive pressure expelling the dry air and creating a very high partial pressure of water inside the susceptor. This steam-rich environment was easily observable by the condensation on components above the furnace. However, no condensation was observed below the furnace due to vertical convection within the susceptor.

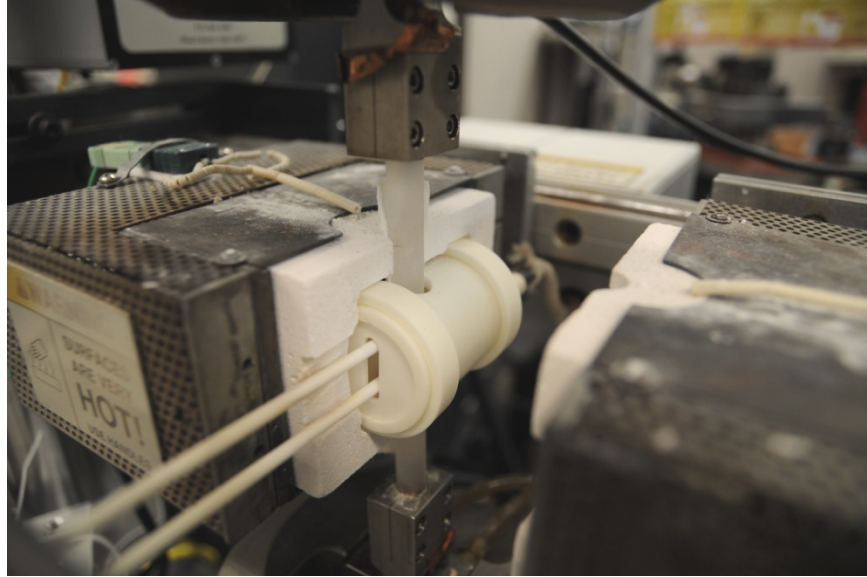


Figure 30. Compression test setup showing the susceptor

For elevated temperature testing, two R-type thermocouples were placed on the specimens surfaces to calibrate the furnace on a periodic basis. The furnace controllers (using non-contacting thermocouples exposed to the ambient environment near the test specimen) were adjusted to determine the power settings needed to achieve the desired temperature of the test specimen. The determined power settings were then used in actual tests.

Note that in order to achieve the desired temperature of the test specimen, the MTS 409.83 temperature controllers had to be reprogrammed. The maximum temperature setpoint for the temperature controller was 1410°C with a rated furnace temperature of 1400°C. However, higher setpoints were needed for the test specimen to reach a temperature of 1300°C. MTS was consulted the temperature controllers setpoint limits were extended to 1450°C. To achieve the specimen temperature of 1300°C in air, the final temperature controller settings were 1419°C. To achieve the specimen

temperature of 1300°C in steam, the final temperature controller settings were 1422°C. Since the susceptor acted as a thermal buffer which radiated symmetrically about the center, both the right and left temperature controller setpoints were equal for each environment. Additionally, the use of the susceptor with the control thermocouples located between the susceptor and the silicon carbide elements ensured highly repeatable temperature calibrations even after replacing damaged heating elements.

The test method developed for testing the polycrystalline YAG and polycrystalline alumina specimens in compression employed single-crystal YAG pushrods of 0.400" diameter. The pushrods were mounted in custom built stainless steel fixtures, which were gripped in the water-cooled hydraulic wedge grips (see Figure 31). The test specimens were compressed between the pushrods. Various thin foils were used on all contact surfaces to alleviate point stress concentrations on the specimen and on the pushrods. Thin (0.0004") copper foil was placed around the circumference and on the end of the single crystal YAG pushrod where it interfaced with the stainless steel fixture. Additionally, 0.005"-thick platinum foil was placed between the top and bottom surfaces of the specimens and the single crystal YAG pushrods. Compressive loading was transferred through the ends of the single crystal YAG pushrod to the compression specimens. The close fit on the circumference of the pushrods and fixtures was designed to ensure proper alignment, not to transfer the desired compressive loads. The loads induced on the circumference of the pushrod and grip fixture were relieved by loosening the set screws on the custom grip fixture after the load train was assembled and immediately prior to conducting each test.

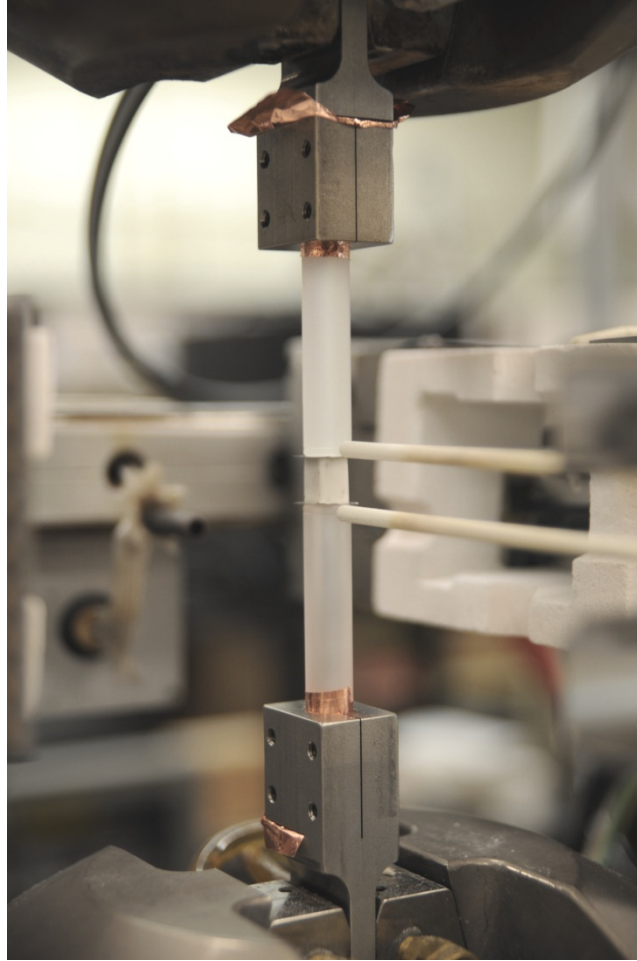


Figure 31. Compression creep test set-up for polycrystalline YAG and polycrystalline alumina specimens

3.3.2 Strain Measurement

For elevated temperature testing the furnace was positioned such that the test specimens were centered in the hot section. A portion of the top and bottom pushrods were also located inside the hot zone. Strain measurements were accomplished with an MTS 632.53E-14 high temperature, low contact force extensometer with a 0.5 in. (12.5 mm) gauge length and a range of +20% to -10% (maximum nonlinearity of 0.15%). A

heat shield and air cooling were used to protect the extensometer from the high temperatures.

Because the extensometer gauge length exceeded the height of the polycrystalline YAG specimens a direct strain measurement, with the extensometer rods positioned on the polycrystalline YAG specimen was clearly impossible. An alternative was to measure the strain by positioning the extensometer rods on the single crystal YAG pushrods, close to the polycrystalline YAG specimen. This alternative was reasonable and defensible if and only if it could be demonstrated that single crystal YAG would produce no measurable creep strain under the “worst” conditions (largest creep stress magnitude in steam). Then it could be argued that whatever strain was measured, was produced by the polycrystalline YAG specimen. To explore the feasibility of this alternative strain measurement option, a single crystal YAG specimen was tested in creep. In this test the extensometer mounted directly into the single crystal YAG specimen. To ensure that the extensometer rods did not slip, two horizontal grooves (0.020” tall by 0.010” deep) were machined into the surface of the single crystal YAG specimen for mounting the extensometer rods. Results of this test are discussed in detail in the section 3.3.3 below.

The alternative strain measurement option outlined above proved to be successful. Hence in all compression creep tests on polycrystalline YAG specimens as well as on polycrystalline alumina specimens, the strain measurement was accomplished by positioning the extensometer rods on the single crystal YAG pushrods. To ensure good contact with the extensometer, grooves (0.020” tall by 0.010” deep) were cut into the circumference of each single crystal YAG pushrod. The grooves were located 0.070”

from the edge of each pushrod. As result, accurate measurements of compressive strain in the polycrystalline YAG and Al_2O_3 specimens were achieved. Figure 31 depicts the extensometer mounted on the grooved single crystal YAG pushrods.

The strain measured by mounting the extensometer on the ends of the single crystal YAG pushrods was based on the extensometer gauge length of 0.5 in., which differed from the actual specimen length. To obtain accurate strain for the polycrystalline YAG specimen, the strain measured by the extensometer had to be corrected to account for this difference in lengths. This was accomplished with a correction factor, termed “strain ratio”.

It was shown in Section 3.3.3 that the single crystal YAG pushrods were practically rigid as compared to the polycrystalline YAG specimen. Therefore under a compressive load, the change in length as measured from the grooves near the edges of the pushrods and the change in length of the test specimen were equal. The error in the measured strain was thus solely due to the difference in the extensometer gauge section and the original length of the polycrystalline YAG specimen. Let the strain measured by the extensometer be given as:

$$\varepsilon_m = \frac{\Delta l}{L_{ref}} \quad (13)$$

where Δl is the change in length and L_{ref} is the extensometer’s referenced gauge length, (i.e. 0.5 in.). Similarly, the strain produced by the polycrystalline YAG specimen strain is given by:

$$\varepsilon_{sp} = \frac{\Delta l}{L_{sp}} \quad (14)$$

where Δl is again the same overall change in length but L_{sp} is the original length of the polycrystalline YAG specimen. Now, define the “strain ratio” as the ratio of strain produced by the polycrystalline YAG specimen to that measured by the extensometer, such that

$$\text{strain ratio} = \frac{\varepsilon_{sp}}{\varepsilon_m} = \frac{L_{ref}}{L_{sp}} \quad (15)$$

Now, the strain produced by each polycrystalline YAG or polycrystalline alumina specimen can be obtained by multiplying the strain measured by the extensometer by the “strain ratio”. The “strain ratios”, which can be readily obtained for each specimen, were given in Table 7 and Table 8 together with the specimen dimensions.

Additionally, a Schaevitz 1000 MHR LVDT, that provided high resolution linear displacement measurements, was mounted to the bottom grip. This was added as a contingency measurement, if the extensometer measurements were unsuccessful. These LVDT measurements were recorded in all tests, but were not used in the data analysis because the extensometer measurements were successful.

3.3.3 Single Crystal YAG – Baseline Testing for YAG Pushrods

The experimental setup for compression creep tests utilized single crystal YAG pushrods that extended into the furnace from both top and bottom and compressed the

test specimens located inside the furnace. Recall that the polycrystalline YAG and polycrystalline alumina specimens were too short to obtain direct strain measurements. Therefore, the extensometer rods were mounted in grooves machined into the ends of the single crystal YAG pushrods. To employ this strain measurement method with confidence, it was necessary to demonstrate that the single crystal YAG pushrods would indeed produce negligible creep strain under the most severe loading and environmental test conditions encountered in this research program.

Hence a baseline compression creep test on a single crystal YAG specimen had to be performed. A specimen of single crystal YAG was machined. The height of this specimen was sufficient to allow a direct strain measurement with the extensometer (i.e. the extensometer rods were mounted directly on the specimen in horizontal slots machined on one face of the specimen). Figure 32 shows the single crystal YAG specimen mounted between the single crystal YAG pushrods prior to testing.

Because steam at 1300°C is the most aggressive environment to be encountered by the polycrystalline YAG and/or polycrystalline alumina specimens in this research, the single crystal YAG specimen was tested at 1300°C in steam. Compressive creep testing was conducted with stress magnitudes increasing stepwise from 50 MPa to 100 MPa to 150 MPa. Each stress level was maintained for 3 hours without any measurable strain being recorded. Finally the stress was increased to 200 MPa and maintained at 200 MPa for 5 hours. The resulting strain varied less than $\pm 0.1\%$ over the duration of the test. A linear regression analysis of the strain versus time plot, shown in Figure 33, yielded a steady-state strain rate of $1.06 \times 10^{-8} \text{ s}^{-1}$.

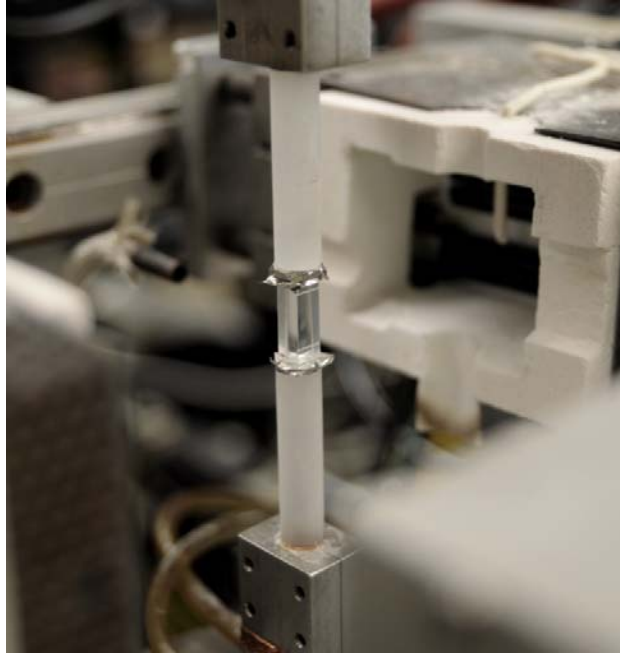


Figure 32. Single Crystal YAG Specimen mounted for compression creep testing

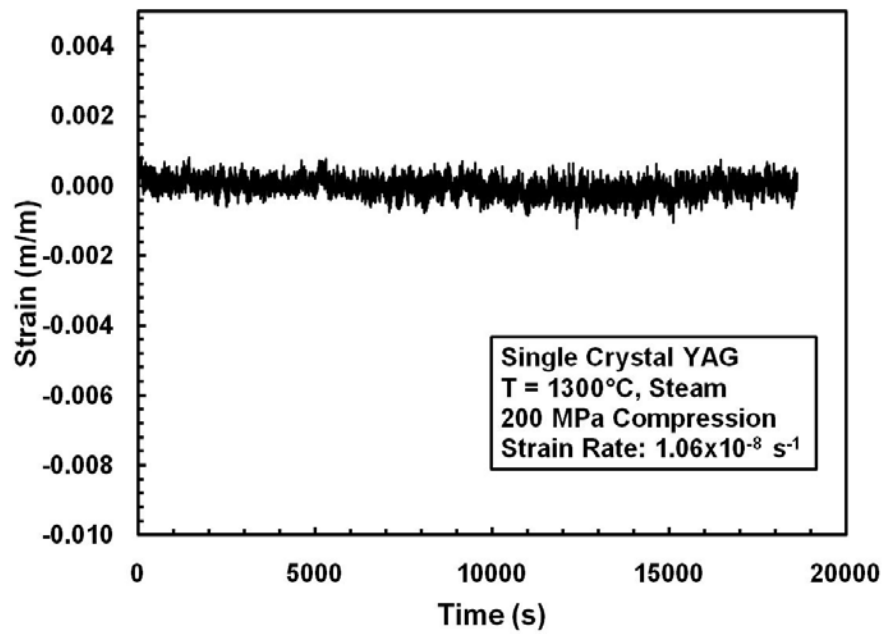


Figure 33. Creep strain vs. time curve for single crystal YAG obtained at 200 MPa at 1300°C in steam

The negligibly small strain rate produced by the single crystal YAG specimen was at least one order of magnitude lower than the strain rates produced by the polycrystalline YAG specimens tested under the same condition. Moreover, at lower stress levels creep of the single crystal YAG was not measurable. Therefore, it was concluded that any strain resulting from the single crystal YAG pushrods was negligible in comparison to the amount of strain produced by the polycrystalline YAG or polycrystalline alumina specimens.

3.4 MTS Servo-Hydraulic Testing System Control

Use of the servo-hydraulic testing equipment previously described requires accurate control. The servo-hydraulic system is utilized by controlling hydraulic actuators that provide axial displacement. The actuators are controlled through electrical servo valves, which govern the flow of oil to the actuators. Modern servo-hydraulic testing equipment has the capability to apply precise displacements and loads over a wide range of displacement and loading rates. While test materials may range from pliable visco-elastic polymers to stiff metals and ceramics, the control system must be adjusted for the specific material under test. This calibration process is referred to as tuning.

3.4.1 Tuning – The Concept

Tuning is the process of changing system variables in order to minimize the difference between the command signal and the feedback signal. This difference is referred to as error. In other words, tuning the system is getting the machine to do what you want it to do. Consider, for example, a test in which the desired action is a constant

load rate on a test specimen. The system controller sends a signal to the actuator to increase the load. The motion of the actuator results in increased load on the specimen. The load cell senses the increased load and reports the sensed load back to the controller. The controller then compares the commanded load to the measured load. The controller then compensates another outgoing signal to the servo valve in an attempt to minimize the error. This closed-loop control process runs continuously throughout the test. With proper tuning of the control parameters, the result is a quick and stable response that closely matches the commanded signal.

For control of such a process, many variables are critical to success. Examples of these variables include feedback sample frequency, rate of motion of the actuator, and many others. Most of these are determined during the machine design by the equipment manufacturers. Nevertheless, the variables which are adjusted in tuning a servo-hydraulic machine to a specific material are the proportional (P) and integral (I) gains in the system controller.

The proportional component of a closed-loop feedback control system produces a response signal that is proportional to the amount of error measured. In order to tune the proportional amount of the response signal the P gain is adjusted. The value of the P gain affects the speed of response of the system to the measured error. If the P gain is too low, the control system will respond too slowly to the commanded signal. As the P gain is increased, the initial error between the commanded and feedback signals decreases more rapidly. One may think that P gain should be maximized in order to achieve the fastest response possible. However, if the P gain is set too high, the control system will overshoot the commanded signal and possibly result in an unstable response. Therefore,

the P gain must be tuned between an acceptable response speed while maintaining a stable response signal.

The integral component of the closed-loop feedback control integrates the error over time and adds to the proportional control in generating the control signal. The I gain is the adjustable variable in tuning the integral control. If a steady-state error exists between the command and feedback signals, then the I gain is too low. If the I gain is too high, the controlled signal will significantly overshoot the desired response. Excessive I gain will result in the control command oscillating about the desired response. Similar to the P gain, the I gain must be tuned to an acceptable level in order to optimize the controlled command to the desired response.

Figure 34 shows an example of servo-hydraulic system with low P and I gains. The low P gain is depicted by the slow initial response upon a command change. The low I gain is illustrated by both a slowly converging response for the constant load condition and by the non-converging response during the constant load rate. After proper tuning, the system response matches the command signal much more closely as illustrated in Figure 35.

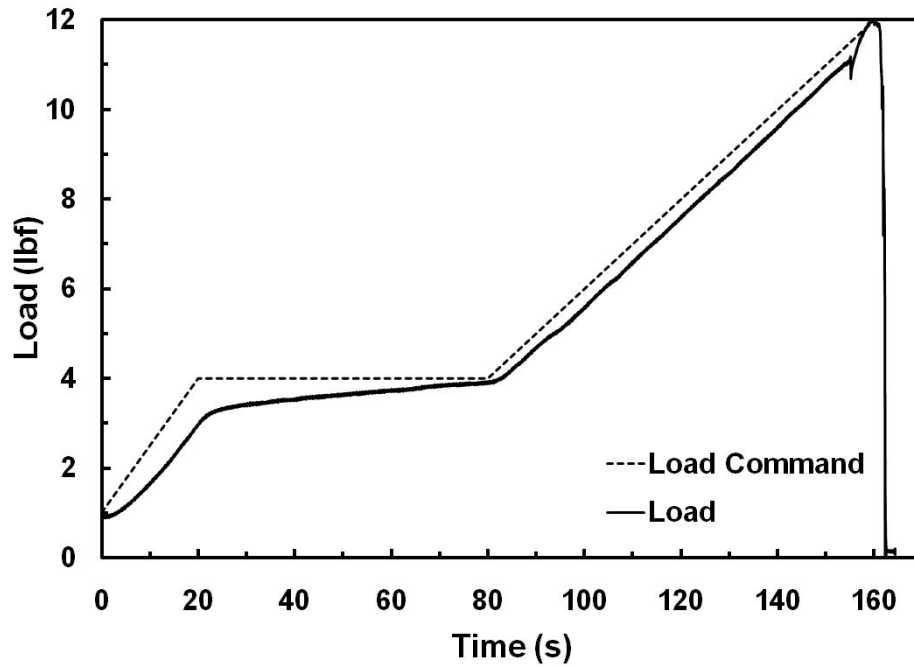


Figure 34. Poorly tuned servo-hydraulic system

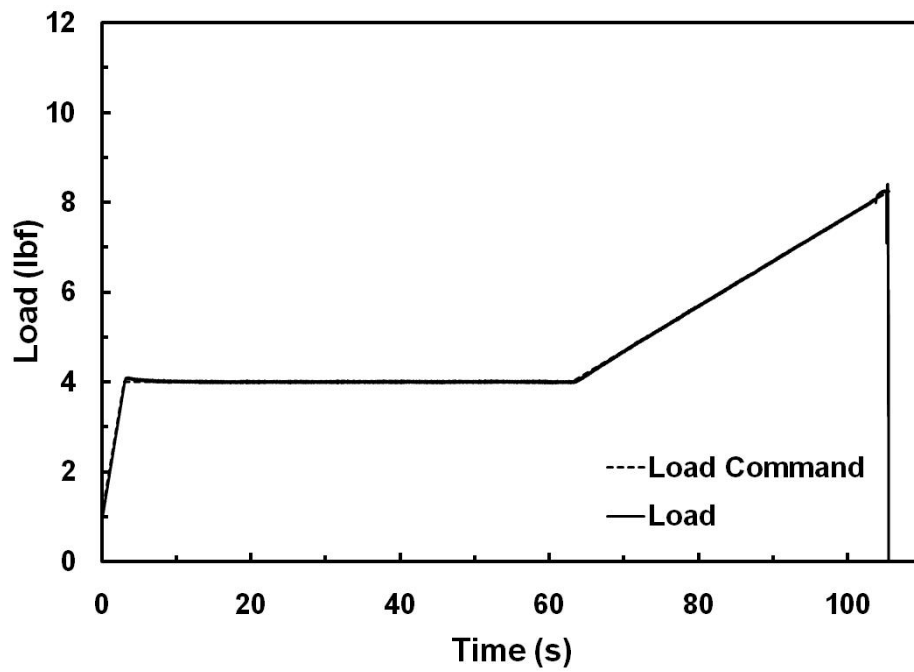


Figure 35. Properly tuned servo-hydraulic system

3.4.2 Tuning – The Procedure

The system controller for all testing in this study was an MTS FlexTest 40 digital controller. Two control modes were utilized: load control and displacement control. Tuning of the FlexTest 40 used a built-in function generator to provide commands to the system. Real time built-in scope was used to compare the command and response signals throughout the tuning process.

Before tuning the system, a system warm-up was performed in displacement control without a specimen in the load train. Square wave forms at 5-10 Hz were used for the warm-up. After a brief warm-up, the displacement control mode was tuned. Again, no specimen was loaded during tuning of the displacement control mode. Therefore the displacement control mode was not material dependent unlike the load control mode. A buildup approach for both frequency and displacement was used. Initially, a low frequency and small displacement, like 0.5 Hz and ± 0.05 inch, were used. Also, per MTS recommendations, the I gain was initially set at 10% of the P gain. After comparing a few cycles of the commanded and response signals, the P and I gains were adjusted. Next, the frequency and displacement were increased to 1 Hz and ± 0.10 inch. Again, the P and I gains were adjusted as necessary while comparing the commanded and response signals. Finally, the frequency and displacement were increased to 5 Hz and ± 0.15 inch. In displacement control, the gains for the smaller MTS LandmarkTM 370 system used for fiber testing, were $P = 20$ and $I = 4$. In displacement control, the gains for the larger MTS 810 system used for compressive creep testing, were $P = 60$ and $I = 5$.

For tuning the load control mode, a specimen must be gripped in the load train. Therefore, load control is highly dependent upon the material and specimen to be tested. With a specimen gripped and with the controller set in load control, a buildup for both frequency and load was used. The frequency was initially set at 0.25 Hz and was incrementally increased to 1.0 Hz. Immediately after the specimen was gripped, a small load was applied to the specimen. For the tensile testing, the initial loading was in tension. For compressive testing, the initial load was in compression. A rule-of-thumb is to tune the specimen around 10% of its ultimate strength. However, for the fiber tow testing, the load control tuning was performed at $2 \text{ lbf} \pm 1 \text{ lbf}$. Additionally, the initial load control tuning was performed with the specimen at room temperature, however, it was necessary to retune or verify the tuning at test temperatures. Similar to the displacement control tuning, the P and I gains for load control were adjusted as necessary while comparing the commanded and response signals. In load control, the gains for the smaller MTS LandmarkTM 370 system used for fiber testing, were $P = 150$ and $I = 50$. For a small set of testing performed on NextelTM 610 in steam, a P gain of 200 and I gain of 100 were used. This proved to be marginally stable for NextelTM 610 and unstable for NextelTM 720. Therefore, the gains were reduced to the original values of $P = 150$ and $I = 50$ for the majority of fiber tow testing. In load control, the gains for the larger MTS 810 system used for compression creep testing, were $P = 15$ and $I = 2$.

3.5 Summary of Experimental Methods

In this chapter, the experimental methods are addressed in detail. The test materials and specimen preparation are described. In order to accomplish this

experimental endeavor, extensive work was performed in establishing the experimental facilities. For fiber tow testing, two facilities were designed – a hydraulically actuated monotonic tension facility and a dead weight creep facility. For both facilities, an in-depth discussion is provided for the temperature calibration and profiles, which led to the ability to make precise strain measurements from displacement measurements through the use of an innovative numerical integration approach.

Additionally, a compressive creep facility was designed in order to test the experimental bulk specimens. In this facility, direct contact strain measurements were feasible. An analysis of the baseline test of the single crystal YAG pushrod material is provided to demonstrate that the strain produced in the pushrods was negligible compared to the specimen strain.

Lastly, a description is provided for the control of the servo-hydraulic test systems. An overview of tuning the system's command/feedback loop is described, as well as, the tuning procedure and specifics used in this work.

These experimental methods facilitated the successful accomplishment of the objectives of this research.

IV. Mechanical Behavior of Nextel™ 610 Fiber Tows at 1100°C

This chapter discusses (1) the influence of loading rate on tensile strength of Nextel™ 610 fiber tows at 1100°C in air and in steam and (2) the experimental investigation of the effects of steam on creep performance of Nextel™ 610 fiber tows at 1100°C in air and in steam. Experimental results are presented and analyzed. A linear elastic crack growth model is used to predict the creep lifetimes from the constant stress rate test data. Finally, the Monkman-Grant relationship is applied to creep data obtained for Nextel™ 610 fiber tows at 1100°C in air and in steam.

4.1 Influence of Loading Rate on Tensile Strength of Nextel™ 610 Fiber Tows at 1100°C in Laboratory Air and in Steam

Previous studies by Ruggles-Wrenn et al. [125, 126, 129] revealed a strong influence of loading rate on the monotonic tensile behavior and tensile properties of oxide-oxide CMCs at elevated temperature in steam. Results obtained by Ruggles-Wrenn and co-workers suggest that the environmentally assisted subcritical crack growth in the fibers may be responsible for the rate-dependence of strength exhibited by the composites. To explore this hypothesis a series of constant stress rate tension tests to failure were performed on the Nextel™ 610 fiber tows at 1100°C in laboratory air and in a steam. The experimental setup described in Section 3.2 was employed.

The tensile strength values obtained at 1100°C in laboratory air at stress rates ranging from 10 to 1000 MPa/sec did not exhibit a clear dependence on the stress rate. The average ultimate tensile strength (UTS) obtained for the Nextel™ 610 fiber tows at 1100°C in air was 513 MPa. However, the data variability was large with an overall

standard deviation of 128 MPa. It is noteworthy that these tests resulted in lower UTS values than the tensile tests conducted in displacement control with a rate of 0.05 mm/sec, which yielded an average UTS of 672 MPa with a standard deviation of 42 MPa.

In contrast, the tensile strength values produced in monotonic tension tests of the NextelTM 610 fiber tows conducted at 1100°C in steam were strongly influenced by the rate of loading. The values of tensile strength obtained at various stress rates are presented in Table 9. As seen in Figure 36, the UTS of the NextelTM 610 fiber tows obtained at 1100°C in steam increases as the stress rate increases from 1 to 30 MPa/sec. Once the stress rate exceeds 30 MPa/sec, the ultimate tensile strength of the fiber tow becomes independent of the stress rate suggesting that the rate of crack growth has saturated. For stress rates ≥ 30 MPa/s, the tensile strength is approximately 900 MPa.

Through additional analysis, namely the determination of the subcritical crack growth parameter, predictions for creep lifetimes can be determined from the monotonic tension experiments. Subcritical crack growth parameters are determined in the next section. These values are then used to make creep lifetime predictions, which are compared to creep results in Section 4.4.

Table 9. Tensile strength values obtained at various constant stress rates for Nextel™ 610 fiber tows at 1100°C in steam environment

Loading Rate (MPa/sec)	1	10	30	100	1000
	456.8	694.0	866.8	849.9	949.4
	547.0	834.3	914.9	975.3	839.5
	638.6	775.1	915.5	960.3	
Average (MPa)	547.5	767.8	899.1	928.5	894.5
Standard Deviation	90.9	70.4	27.9	68.5	77.7

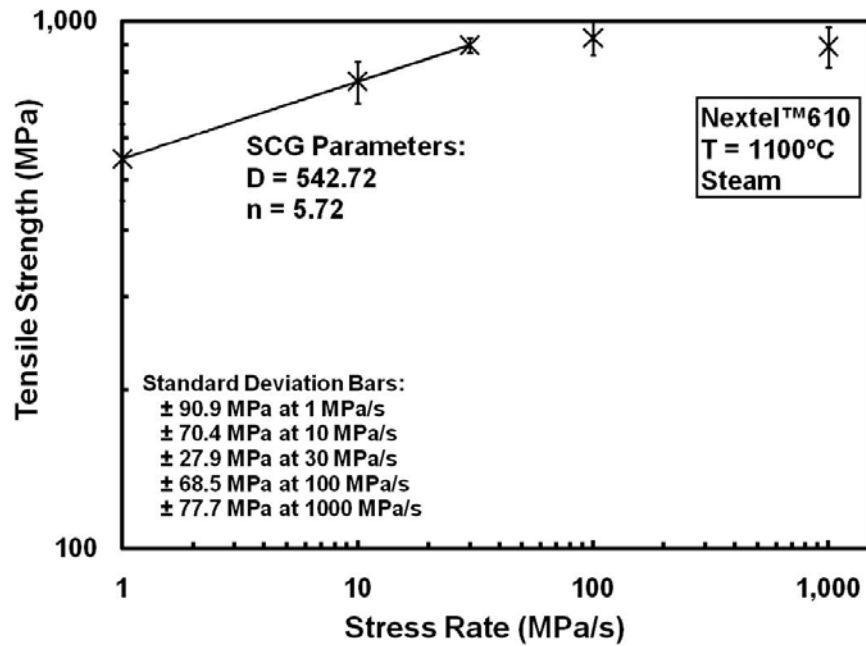


Figure 36. Tensile strength as a function of stress rate for Nextel™ 610 fiber tow at 1100°C in steam. Effect of loading rate on ultimate tensile strength is evident.

4.1.1 Determination of Subcritical Crack Growth Parameters for Nextel™ 610 Fiber Tows at 1100°C in Steam

The strong dependence of tensile strength on stress rate reported by Ruggles-Wrenn et al. [125, 126, 129, 133] for the CMCs was akin to that observed for the monolithic ceramics at elevated temperatures [9, 20, 38]. For monolithic ceramics the time (or rate) dependency of strength (also known as delayed failure) has been shown to proceed by environmentally assisted subcritical crack growth (also known as slow crack growth) [154, 155, 157]. The subcritical crack growth rate can be expressed by the empirical power-law relation [4, 5, 38]:

$$v = \frac{da}{dt} = A \left[\frac{K_I}{K_{IC}} \right]^n \quad (16)$$

where:

v = crack velocity

a = the crack size

t = time

K_I = the mode I stress intensity factor

K_{IC} = the critical stress intensity factor (or fracture toughness)
under mode I loading

A, n = the slow crack growth parameters associated with the
material and environment.

By definition, the mode I stress intensity factor is related to the applied stress by

$$K_I = Y \sigma \sqrt{a} \quad (17)$$

where:

Y = geometry factor related to flaw shape and its orientation to the applied stress

σ = the applied stress

Using Equations 16 and 17, a relationship between the degraded fracture strength, σ_f , under slow crack growth and the inert strength, σ_i , can be formulated as:

$$\sigma_f^{n-2} = \sigma_i^{n-2} - \frac{1}{B} \int_0^t [\sigma(t)]^n dt \quad (18)$$

where, B , is a combined material/environment parameter given by:

$$B = \frac{2K_{IC}^2}{AY^2(n-2)}$$

For constant stress-rate testing, the applied stress becomes:

$$\sigma(t) = \dot{\sigma}t \quad (19)$$

Substituting Equation 19 into Equation 18, the fracture strength becomes:

$$\sigma_f = \left[B(n+1)\sigma_i^{n-2} \right]^{1/(n+1)} \dot{\sigma}^{1/(n+1)} \quad (20)$$

After combining like terms, the fracture strength can be expressed as:

$$\sigma_f = D(\dot{\sigma})^{1/(n+1)} \quad (21)$$

where, D , is a slow crack growth parameter given by:

$$D = \left[\frac{2(n+1)K_{IC}^2\sigma_i^{n-2}}{AY^2(n-2)} \right]^{1/(n+1)}$$

By taking the logarithm of both sides of Equation 21,

$$\log \sigma_f = \frac{1}{n+1} \log \dot{\sigma} + \log D \quad (22)$$

the subcritical (slow) crack growth parameters n and D can be determined through linear regression analysis of Equation 22 when \log (fracture strength) is plotted vs. \log (stress rate).

Following the procedure outlined above, the experimental results obtained for the Nextel™ 610 fiber tows at 1100°C in steam were employed to calculate the subcritical crack growth parameters. Note that only the data points produced at stress rates ranging from 1 to 30 MPa/s were included in the calculation. The subcritical crack growth parameters $n = 5.72$ and $D = 542.72$ were determined. The crack growth exponent n

represents a measure of susceptibility of the material to subcritical crack growth. For brittle materials, the susceptibility is considered high for $n \leq 20$, intermediate for $30 \leq n \leq 50$, and low for $n > 50$. Therefore, at 1100°C in steam, the Nextel™ 610 fiber tows exhibited a high susceptibility to subcritical crack growth.

Considerable susceptibility to subcritical crack growth has been previously observed for several CMCs as well as for some oxide ceramic filaments. Choi et al. [21, 22] found that several non-oxide CMCs exhibited significant susceptibility at temperatures $\geq 1100^\circ\text{C}$ with the values of n ranging from 6 to 20. Similarly, Ruggles-Wrenn et al. [125, 126, 135] reported subcritical crack growth susceptibility in oxide-oxide CMCs at temperatures $\geq 1100^\circ\text{C}$ in steam, with n ranging from 12 to 19. Additionally, Milz et al. [92] and Goering et al. [46] found that single filaments of Nextel™ 720 exhibited considerable susceptibility to delayed failure at temperatures $\geq 1000^\circ\text{C}$ with values of n ranging from 9 to 18.

4.2 Creep of Nextel™ 610 Fiber Tows at 1100°C in Laboratory Air

Creep experiments of Nextel™ 610 ceramic fiber tows were performed at 1100°C in laboratory air utilizing the experimental setup described in Section 3.2. Results of the creep-rupture tests conducted at 1100°C in laboratory air are summarized in Table 10. Representative creep curves obtained at 1100°C in laboratory air are shown in Figure 37. Creep curves produced in all tests conducted in air exhibit primary and secondary creep regimes. In many cases, tertiary creep was also evident. Transition from primary to secondary creep occurred early in the creep life. The accumulated creep strain decreased

as the applied stress increased from 200 to 400 MPa. Similar creep strains were accumulated in the 400 and 500 MPa tests. Creep run-out of 100 hours was achieved in the 100 MPa tests.

Table 10. Summary of creep-rupture results for the Nextel™ 610 fiber tows at 1100°C in laboratory air

Creep Stress (MPa)	Creep Strain (%)	Time to rupture (min)	Steady-State Creep Rate (s ⁻¹)
100 MPa	1.8 †	>6000 †	3.57x10 ⁻⁸
100 MPa	1.5 †	>6000 †	3.23x10 ⁻⁸
200 MPa	16.9	2936	5.45x10 ⁻⁷
200 MPa	14.2	1898	7.42x10 ⁻⁷
300 MPa	10.8	400	2.96x10 ⁻⁶
300 MPa	7.9	245	3.18x10 ⁻⁶
400 MPa	5.0	78	7.39x10 ⁻⁶
400 MPa	4.2	80	6.43x10 ⁻⁶
500 MPa	4.4	33	1.43x10 ⁻⁵
500 MPa	3.0	25	1.40x10 ⁻⁵

† Run-out

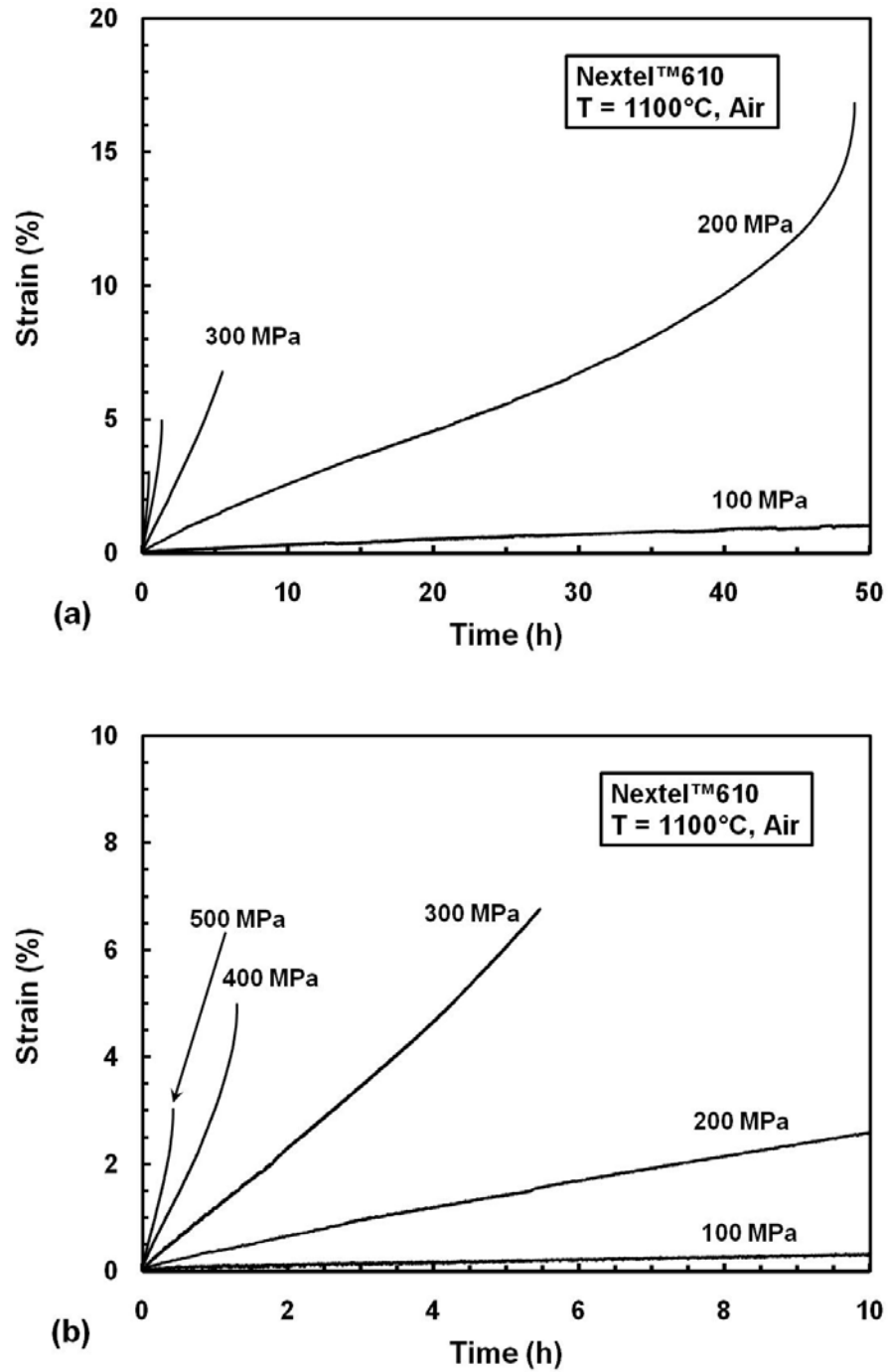


Figure 37. Creep strain vs. time curves for Nextel™610 fiber tows at 1100°C in laboratory air: (a) scale 0-20%, 0-50 h, (b) scale 0-10%, 0-10 h

Steady-state creep rate was reached in all experiments and dominated the majority of the creep lifetime. Creep rate as a function of applied stress is presented in Figure 38 along with fiber tow data from Hammond [49] and single filament results from Wilson [159]. Fitting the creep results obtained for the Nextel™ 610 fiber tows at 1100°C in laboratory air with the power-law equation described earlier in Section 2.4

$$\dot{\epsilon} = A\sigma^n \exp\left(\frac{-Q}{RT}\right) \quad (23)$$

yields a stress exponent $n = 3.4$. This value of the stress exponent is consistent with previous results described in Sections 2.3 and 2.4.

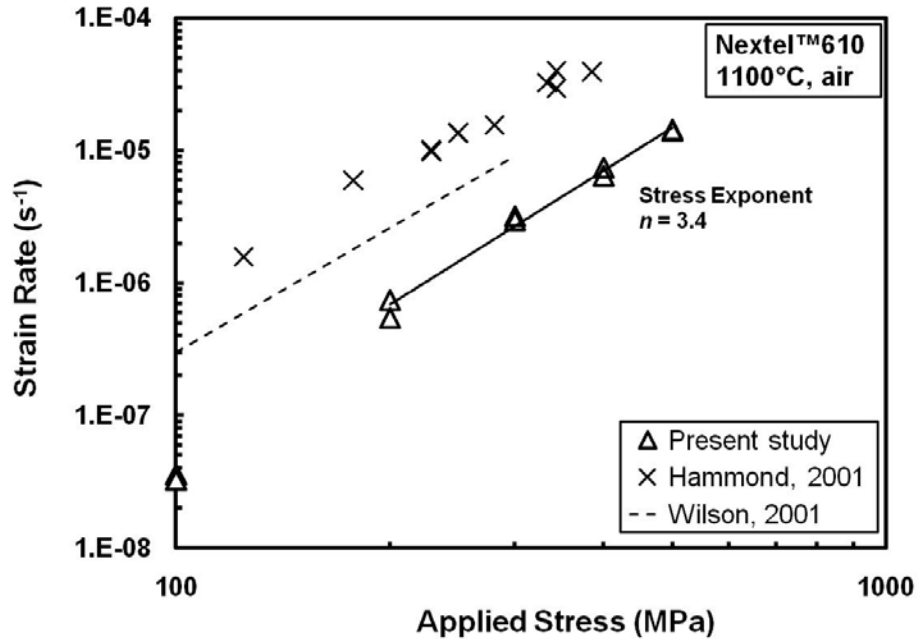


Figure 38. Steady-state creep rate as a function of applied stress for Nextel™ 610 at 1100°C in laboratory air

The creep rates for Nextel™ 610 fiber tows in the present study are less than those reported by Hammond and Wilson. However, the stress exponent $n = 3.4$ is approximately the same as the stress exponents reported by Hammond ($n = 2.9$) [50] and Wilson ($n = 3.1$) [162]. Therefore, the dominant creep mechanism appears to be consistent with the previously reported interface-reaction controlled creep mechanism [50, 161, 162]. The difference in the creep rates of the three studies in Figure 38 is likely due to processing variations in fiber composition (i.e. grain size, silica content, etc.) or possibly due to experimental variations.

Additionally, the stress-rupture behavior at 1100°C in laboratory air is summarized in Figure 39. As expected, the creep lifetime decreases with increasing applied stress.

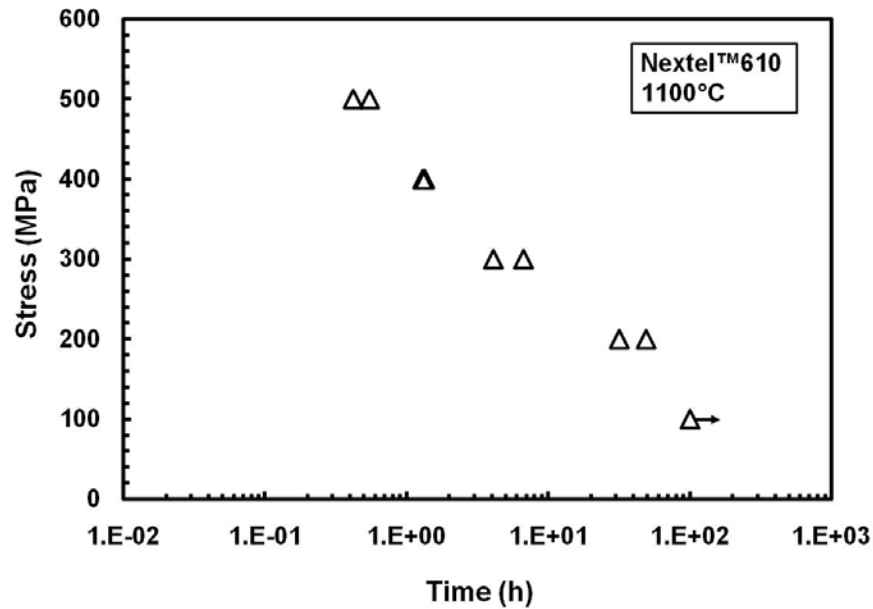


Figure 39. Creep stress vs. time to rupture for Nextel™ 610 fiber tows at 1100°C in laboratory air. Arrow indicates that failure of specimen did not occur when the test was terminated.

4.3 Creep of Nextel™ 610 Fiber Tows at 1100°C in Steam Environment

A recent study by Ruggles-Wrenn et al. [136] revealed a degrading influence of steam on high-temperature creep performance of oxide-oxide CMCs reinforced with Nextel™ 610 fibers. Creep behavior of Nextel™ 610/Monazite/Al₂O₃ composite and of Nextel™ 610/Al₂O₃ composite was studied at 1100°C in both air and steam environments. The addition of monazite coating significantly improved the creep resistance. However, the presence of steam accelerated creep rates of both the monazite containing CMC and of the uncoated fiber composite by approximately two orders of magnitude. Mechanical behavior of a composite with 0°/90° fiber orientation under tensile loading is fiber-dominated. Therefore, fiber degradation represents a likely source of composite degradation. In the current study, creep experiments were performed at 1100°C in steam on the Nextel™ 610 ceramic fiber tows alone in order to evaluate the effects of steam on creep behavior of the fibers.

Creep experiments of Nextel™ 610 ceramic fiber tows were performed at 1100°C in steam environment utilizing the experimental setup described in Section 3.2. As was described in Section 3.2, initial experiments conducted at 1100°C in steam employed the susceptor with the steam port located at the vertical midpoint. After a few initial tests, the susceptor design was improved by relocating the steam port to the bottom of the susceptor. Even though the midpoint configuration proved to be less desirable, the midpoint steam data are included in this chapter. The data with the steam entry point at the bottom resulted from the improved design and corresponds to a steam-rich environment throughout the heated gauge section of the tow.

Results of the creep-rupture tests conducted at 1100°C in steam are summarized in Table 11. Note that creep test results obtained with the initial susceptor design (steam port located at the vertical midpoint) are included in Table 11 for completeness. However, it is believed that the improved susceptor design (steam port located at the bottom) produced a near 100% steam environment around the heated gauge section of the specimen. Hence only the data produced with the improved susceptor design were used in later analyses.

Representative creep curves obtained at 1100°C in steam are shown in Figure 40. Creep curves produced in all tests conducted in steam exhibit primary and secondary creep regimes. In many cases, tertiary creep was also evident. Transition from primary to secondary creep occurred early in the creep life. The accumulated creep strain decreased as the applied stress increased from 200 to 400 MPa. Similar creep strains were accumulated in the 400 and 500 MPa tests. Creep run-out of 100 hours was achieved in the 100 MPa tests. The effect of steam primarily manifests itself in shorter creep lifetimes and increasing steady-state creep rates, while not largely affecting the failure strains.

Table 11. Summary of creep-rupture results for the Nextel™ 610 fiber tows at 1100°C in steam

Creep Stress (MPa)	Maximum Strain (%)	Time to Rupture (min)	Steady-State Creep Rate (s ⁻¹)	Steam Port Location
100	3.1 †	>6000 †	7.88x10 ⁻⁸	Midpoint
200	12.7	987	1.58x10 ⁻⁶	Midpoint
200	9.5	966	1.07x10 ⁻⁶	Midpoint
300	6.2	107	6.16x10 ⁻⁶	Midpoint
300	8.5	149	6.34x10 ⁻⁶	Midpoint
400	1.5	21	1.09x10 ⁻⁵	Midpoint
400	3.5	29	1.26x10 ⁻⁵	Midpoint
500	1.0	4	3.20x10 ⁻⁵	Midpoint
500	2.4	7	4.36x10 ⁻⁵	Midpoint
100	9.9 †	>6000 †	2.23x10 ⁻⁷	Bottom
200	15.1	402	3.63x10 ⁻⁶	Bottom
200	14.9	511	2.85x10 ⁻⁶	Bottom
300	6.5	55	1.33x10 ⁻⁵	Bottom
300	6.8	57	1.24x10 ⁻⁵	Bottom
400	3.8	15	3.09x10 ⁻⁵	Bottom
400	2.1	12	2.48x10 ⁻⁵	Bottom
500	3.2	6	5.80x10 ⁻⁵	Bottom
500	3.9	14	3.40x10 ⁻⁵	Bottom

† Run-out

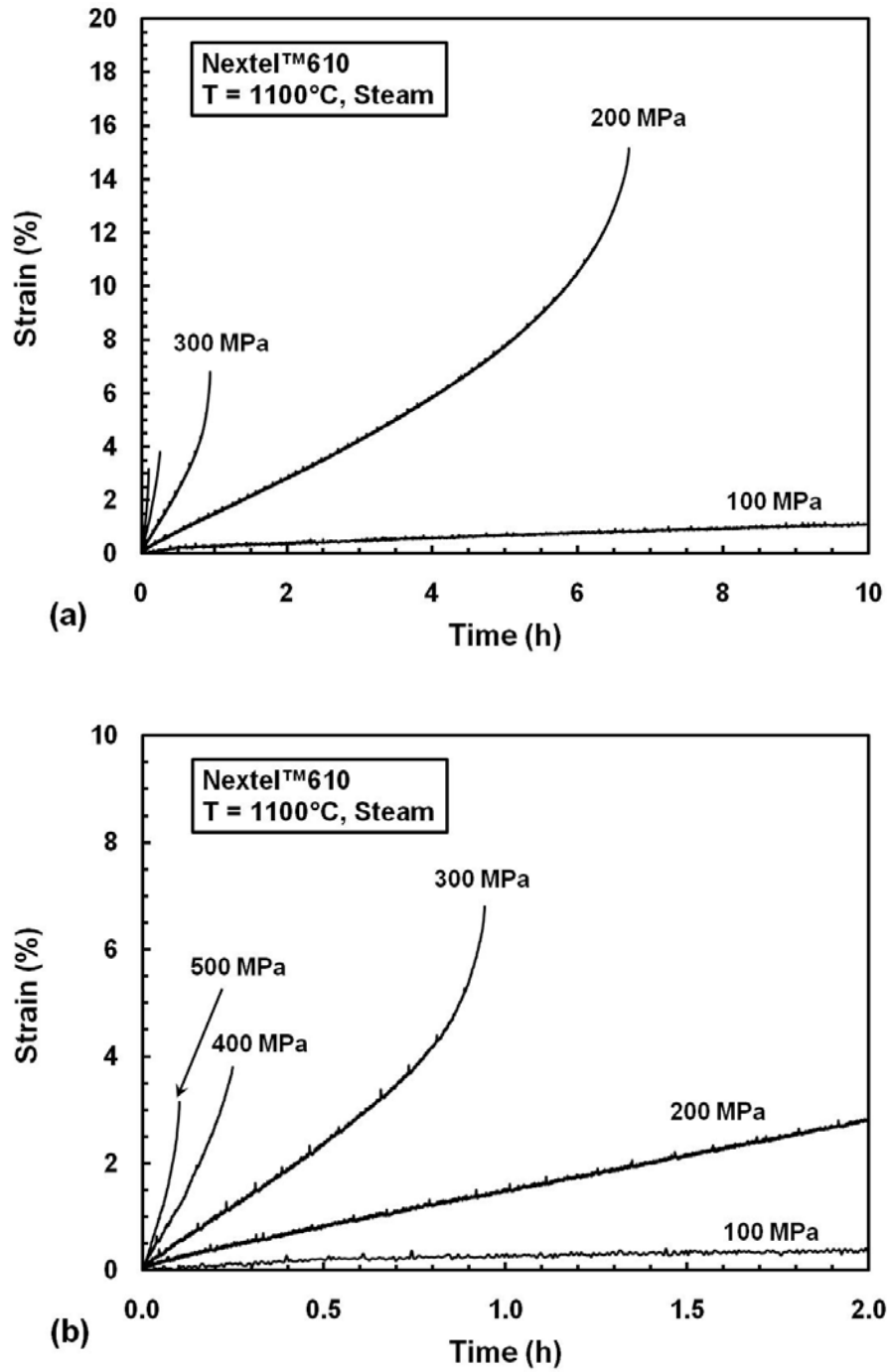


Figure 40. Creep strain vs. time curves for Nextel™ 610 fiber tows at 1100°C in steam:
 (a) scale 0-20%, 0-10 h, (b) scale 0-10%, 0-2 h

Steady-state creep rate was reached in all experiments and dominated the majority of the creep lifetime. Creep rate as a function of applied stress is presented in Figure 41. Creep results obtained at 1100°C in steam were fitted with the power-law equation of the form given in Equation 23. Then the stress exponent $n = 2.9$ was determined by linear regression for Nextel™ 610 fiber tows at 1100°C in steam.

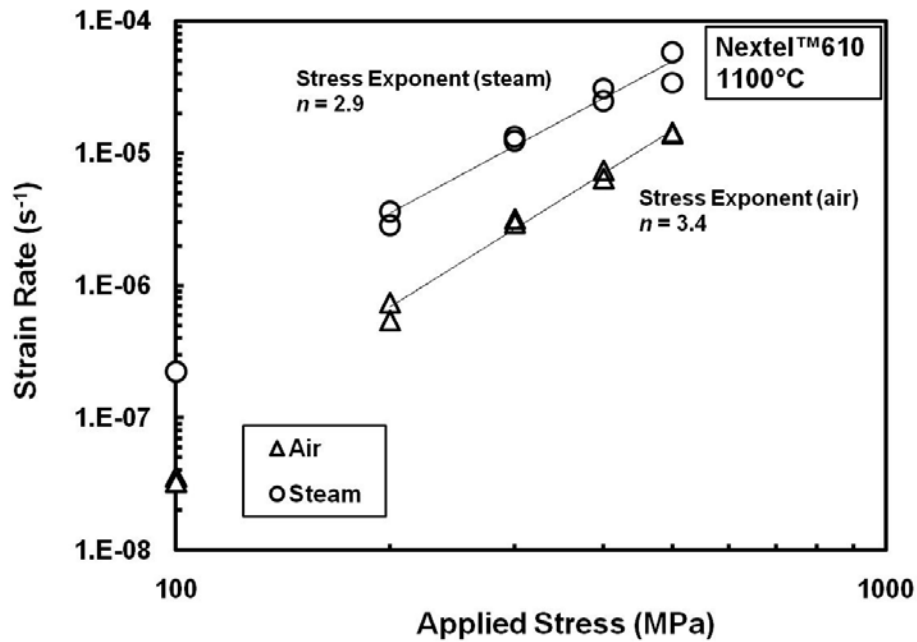


Figure 41. Steady-state creep rate as a function of applied stress for Nextel™ 610 fiber tows at 1100°C in laboratory air and in steam

Notably, approximately the same stress exponent, $n \approx 3$, was obtained for Nextel™ 610 fiber tows at 1100°C in air and in steam (notice the two nearly parallel regression lines in Figure 41). Again, this stress exponent is consistent with the interface-reaction controlled creep mechanism. However, steam had a noticeable effect on creep performance of the Nextel™ 610 fiber tow at 1100°C. In the presence of steam, the creep rate of the Nextel™ 610 fiber tow increased by nearly one order of magnitude.

Recall the study [136] described at the beginning of this chapter, in which the creep rate of the NextelTM 610 based CMCs increased by approximately two orders of magnitude. However for an individual fiber tow, the current study demonstrates only one order of magnitude increase in steam. For a possible explanation of this difference between the fiber tow and CMC, consider the previously mentioned study by Schmücker et al. [139]. In that study, excessive out-diffusion of silica was observed from the fiber into a pure alumina matrix. As a result of the loss of silica, excessive grain growth in the alumina fiber was observed for the CMC as compared to a stand alone fiber under the same conditions. As discussed earlier in Section 2.5, steam at high temperatures has also been shown to deplete silica from alumina [44, 72, 147], which would also result in alumina grain growth. For the CMC containing NextelTM 610, the matrix may buffer the fiber and slow the rate of silica volatilization and therefore lead to less grain growth of the CMC based fiber. Whereas, a more rapid depletion rate of silica from the fiber tow alone in the steam environment may lead to further or more rapid grain growth than in the CMC, which lowers the creep rate compared to the CMC. For confirmation of this phenomenon, microscopy and further analysis of both the NextelTM 610 fiber tow and the CMC are required.

The stress-rupture behavior at 1100°C in steam is summarized in Figure 42. As expected, the creep lifetime decreases with increasing applied stress. At 1100°C the presence of steam reduced the creep lifetime of the NextelTM 610 fiber tow by nearly one order of magnitude.

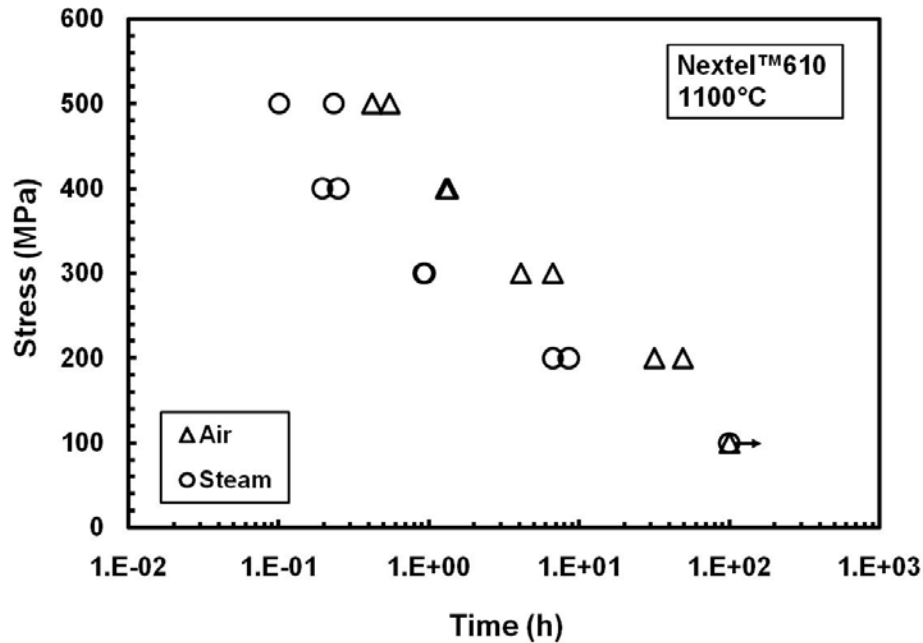


Figure 42. Creep stress vs. time to rupture for Nextel™ 610 fiber tows at 1100°C in laboratory air and in steam. Arrow indicates that failure of specimen did not occur when test was terminated.

The effects of steam on the creep performance of Nextel™ 610 fiber tow at 1100°C are significant. The presence of steam accelerates the steady-state creep rate by approximately one order of magnitude. Moreover, the presence of steam reduces creep lifetime of the tow by approximately one order of magnitude.

4.4 Predicting Creep Lifetimes from Constant Stress Rate Test Data for Nextel™ 610 Fiber Tows at 1100°C in Steam

For many glass and ceramic materials that exhibit subcritical (slow) crack growth as the dominant time-dependent failure mechanism, time to failure under constant stress (creep lifetime) can be predicted from constant stress-rate test data by using the linear elastic crack growth model. Griffith in 1920 postulated that brittle materials already

contain (pre-existing) cracks. The linear elastic fracture mechanics is based on the assumption that failure of brittle materials occurs due to stress-induced growth of these preexisting flaws to critical size for spontaneous crack propagation. The time to failure under a constant tensile stress can be derived from the stress intensity factor (see Equation 17). By taking the derivative of Equation 17 with respect to time and substituting the subcritical crack velocity from Equation 16, the expression obtained is:

$$\frac{dK_I}{dt} = v \left(\frac{\sigma^2 Y^2}{2K_I} \right) \quad (24)$$

By rearranging and integrating Equation 23, the time to failure under a constant stress is:

$$t_f = \frac{2}{\sigma^2 Y^2} \int_{K_{II}}^{K_{IC}} \left(\frac{K_I}{v} \right) dK_I \quad (25)$$

where the initial stress intensity factor can be expressed as:

$$K_{II} = \left(\frac{\sigma}{\sigma_i} \right) K_{IC} \quad (26)$$

Substituting Equation 16 into Equation 25 and integrating, the time to failure is:

$$t_f = \frac{2K_{IC}^n}{\sigma^2 Y^2 A(n-2)} \left(K_{II}^{2-n} - K_{IC}^{2-n} \right) \quad (27)$$

Using Equation 26 and recognizing that, in general, $K_{IC}^{2-n} \ll K_{II}^{2-n}$, the failure time becomes:

$$t_f = \left[\frac{2K_{IC}^2 \sigma_i^{n-2}}{AY^2(n-2)} \right] \sigma^{-n} \quad (28)$$

or by combining terms:

$$t_f = \left[\frac{D^{n+1}}{n+1} \right] \sigma^{-n} \quad (29)$$

The time to failure under a constant tensile stress, given in Equation 29, represents the time required for a flaw to grow from an initial, subcritical size to a dimension critical for catastrophic crack propagation to occur. Note that the creep lifetime in Equation 29 is expressed in terms of the subcritical crack growth parameters, n and D , obtained from the constant stress-rate data.

The subcritical crack growth parameters n and D calculated in Section 4.1.1 from the constant stress-rate data for Nextel™ 610 fiber tows at 1100°C in steam were used to predict creep lifetimes for creep stresses ranging from 100 to 500 MPa. Predicted creep lifetimes are listed in Table 12 below.

Table 12. Creep lifetime predicted from constant stress-rate data for Nextel™ 610 fiber tows at 1100°C in steam

Creep Stress	100 MPa	200 MPa	300 MPa	400 MPa	500 MPa
Time to Rupture (min)	21,420.5	406.4	40.0	7.7	2.2

The predicted creep lifetimes are compared with experimental creep results in Figure 43, where the prediction is shown as a solid line. It is seen that the predictions are in excellent agreement with experimental data for all creep stress levels considered except at the highest stress level of 500 MPa. For the highest stress of 500 MPa, which is near the ultimate tensile strength at 1100°C and where fracture is imminent, the creep lifetimes is somewhat under-predicted.

The excellent agreement between the prediction and the experimental results obtained at 1100°C indicates that environmentally-assisted slow crack growth is the governing failure mechanism for Nextel™ 610 fiber tows at 1100°C in steam. It is likely that this subcritical crack growth in the filaments of the fiber tow is a result of chemical interactions of the water molecules with the silica dopant used as a grain growth inhibitor during processing of Nextel™ 610 fiber tows. Recall from Chapter 3, formation of volatile hydroxides (e.g. Si(OH)_4 and Al(OH)_3) have been reported for alumina in hot gas and water vapor environments [44, 72, 147]. Furthermore, recall that Schmücker et al. [139] demonstrated excessive grain coarsening as a result of out-diffusion of SiO_2 into high-purity alumina-based matrices. This could explain the reduced creep lifetime of the

Nextel™ 610 fiber tow. However in this study, further investigations into the microstructure of tested specimens would be required to more fully understand the mechanisms responsible for this subcritical crack growth.

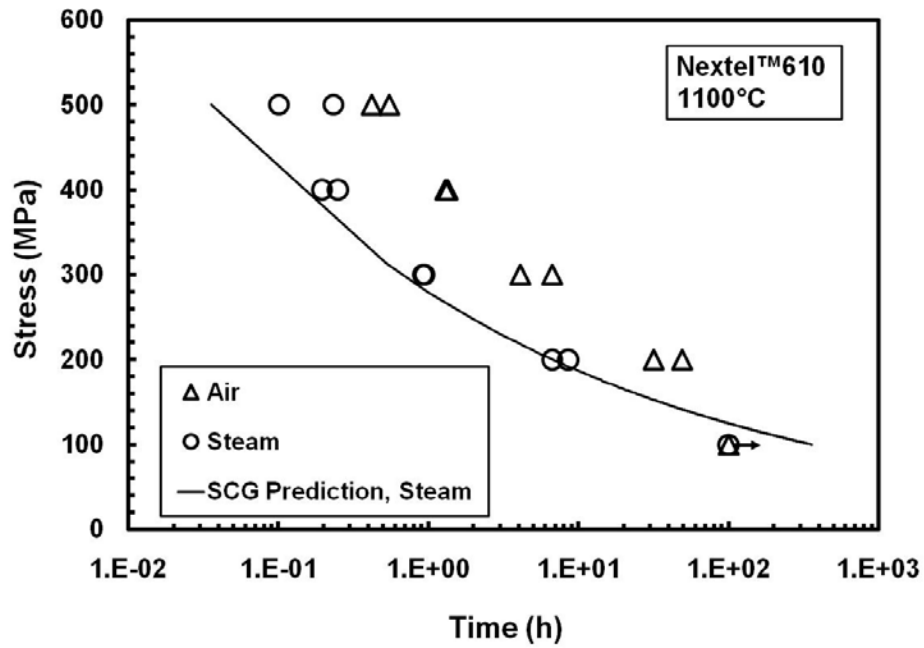


Figure 43. Creep stress vs. time to rupture for Nextel™ 610 fiber tows at 1100°C in laboratory air and in steam. Arrow indicates that failure of specimens did not occur when the test was terminated.

4.5 Stress Rupture of Nextel™ 610 Fiber Tow at 1100°C in Air and in Steam and Monkman-Grant Failure Relationship

The empirical relationship proposed by Monkman and Grant [94] relates the creep-rupture life to the steady-state (or minimum) creep rate as:

$$t_f \dot{\epsilon}^a = C \quad (30)$$

where, a and C are constants. The advantage of using the Monkman-Grant relation is that once the constants a and C have been determined from a limited number of creep tests for a given material, all that is needed for estimating failure time for a long-term test is the value of the secondary creep rate. Since the time required to reach the secondary creep regime is generally short, this information can be gained from short-term tests.

While the Monkman-Grant relationship was originally developed for metals, its applicability to predict rupture life of ceramics has been examined [35, 36, 42, 91]. Ferber and Jenkins [42] evaluated the strength and creep-fatigue behavior of HIPed Silicon Nitride and found that in the 1260-1370°C temperature range the fatigue life was controlled by the secondary creep strain rate in accordance with the Monkman-Grant relation. Menon et al. [91] employed the Monkman-Grant relation to predict the stress rupture life of NT 154 silicon nitride and reported that the Monkman-Grant relation was a function of temperature or stress. DiCarlo and Yun [35, 36] used the Monkman-Grant relation and data obtained from single Nextel™ 610 fibers at elevated temperature in air to successfully predict the creep lifetimes of a woven Nextel™ 610/aluminosilicate composite [173].

In this section, the Monkman-Grant relationship is examined to establish whether the relationship can be used to predict creep-rupture life of Nextel™ 610 fiber tows at 1100°C in air and, especially, in steam. Recall that the presence of steam has a degrading effect on the creep performance of Nextel™ 610 fiber tows at 1100°C. The steady-state creep rates increase by approximately one order of magnitude while the creep lifetimes decrease by approximately one order of magnitude due to steam. Figure 44 shows a log-log plot of the creep lifetime versus the steady-state creep rate obtain for the Nextel™ 610 fiber tows at 1100°C in air and in steam. It is seen that the data obtained (i) in air, (ii) in steam, with steam port located at the midpoint of the susceptor and (iii) in steam, with steam port located at the bottom of the susceptor, fall along a common line. This result indicates that the Monkman-Grant relationship given by Equation 30 applies, and that the Monkman-Grant constants a and C are independent of the test environment. The fit of the experimental data to Equation 30 (shown as a solid line in Figure 44) was good with the coefficient of correlation in regression of 0.957. The Monkman-Grant constants $a = 1.43$ and $C = 2.17 \times 10^{-4}$ were determined from the experimental data by a linear regression analysis.

Furthermore, these results are in reasonable agreement with the Nextel™ 610 fiber tows results from Hammond [49]. The dashed line in Figure 44 was calculated using the values of $a = 1.52$ and $C = 1.67 \times 10^{-4}$ as reported by Hammond. Moreover, the results from DiCarlo et al. [35, 36] for Nextel™ 610 single filament at 1090°C are also included. DiCarlo argues that fiber rupture data can be used to predict stress rupture behavior for cracked and uncracked CMCs under simple application conditions. He compares his single filament data with results from Zuiker's oxide-oxide CMC utilizing Nextel™ 610 as

the fiber reinforcement [173], which are also included in Figure 44. Additionally, Nextel™ 610 based CMC data has also been included from Ruggles-Wrenn et al. in both air [132] and in steam [136].

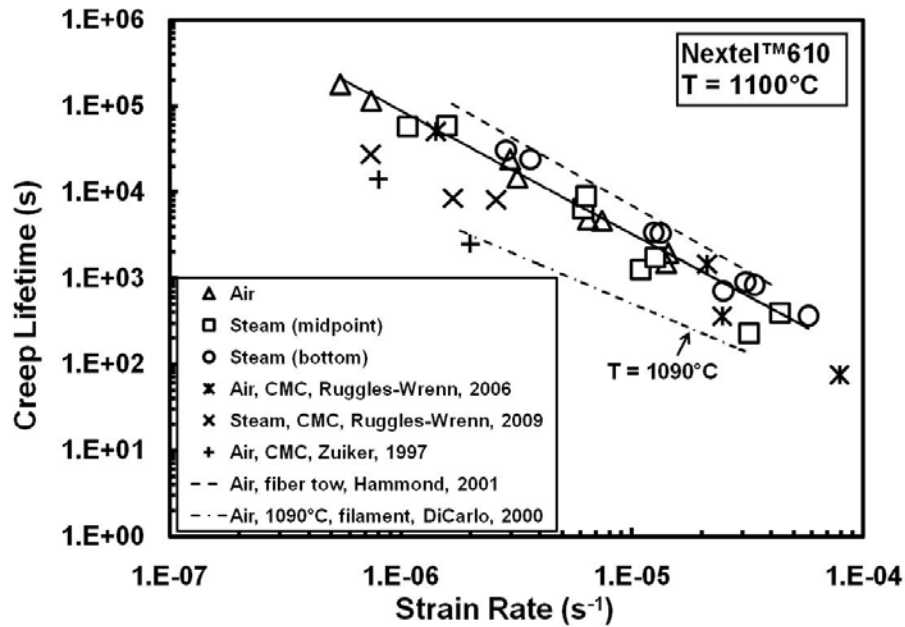


Figure 44. Monkman-Grant plot of creep lifetime vs. steady-state strain rate for Nextel™ 610 and CMCs utilizing Nextel™ 610 at 1100°C in laboratory air and in steam

These results indicate that the Monkman-Grant relationship can be employed to predict creep-rupture for the Nextel™ 610 fiber tows at 1100°C in air and in steam. In some cases, the Monkman-Grant relationship from fiber data may accurately predict creep-rupture for Nextel™ 610 based CMCs. However, the validity of the Monkman-Grant relation at a single temperature may have no implication for the interdependence of creep and rupture at other temperatures. Moreover, caution is also advised particularly when attempting to use the Monkman-Grant relation for the fibers to predict creep

behavior of a composite. While DiCarlo compares the Monkman-Grant results of the single fiber to that of Zuiker's Nextel™ 610 based CMC, this type of macroscopic correlation does not always hold (see Halverson et al. [48] for example). For a more rigorous modeling approach, a micromechanical based modeling approach that takes into account the behavior of all constituents should be considered when trying to predict or optimize deformation and failure of CMCs [48, 49, 173].

4.6 Summary of the Effects of Steam on the Mechanical Behavior of Nextel™ 610 Fiber Tows at 1100°C

This chapter detailed a comparison of mechanical properties of Nextel™ 610 fiber tows at 1100°C in both air and in steam. Creep rates and creep lifetimes were determined in both air and in steam. Based on the stress exponent, $n \approx 3$, as compared with previously reported creep results for Nextel™ 610, the dominant creep mechanism was consistent with the interface-reaction controlled creep. In steam, the underlying mechanism did not change. However, the effects of steam on the fiber tow increased the creep rates by one order of magnitude while decreasing the creep lifetime by one order of magnitude. Therefore, the effects of steam have a dramatic effect on diffusion transport of the interface-reaction controlled creep of Nextel™ 610 at 1100°C.

Additionally, the influence of varying the loading rate on the tensile strength of Nextel™ 610 fiber tows was examined. Predictions of creep lifetime based on subcritical crack growth were made from the monotonic tension data. Comparison of the predictions and the creep data revealed that subcritical crack growth is the dominate failure mechanism of Nextel™ 610 fiber tow at 1100°C in steam environment.

Finally, the Monkman-Grant relationship was examined for creep-rupture life of NextelTM 610 in air and in steam. It was found that the Monkman-Grant relationship was independent of the test environment and may be used to accurately predict creep-rupture for NextelTM 610 fiber tow. Additionally, the applicability of the Monkman-Grant relationship for NextelTM 610 based CMCs was also discussed. While the relationship based on fiber data may accurately predict CMC stress rupture behavior in some cases, this approach must be considered with much caution. Rather, a more sophisticated micromechanical based modeling approach should be considered for modeling of CMCs.

V. Mechanical Behavior of Nextel™ 720 Fiber Tows at 1100 and 1200°C

This chapter discusses (1) the influence of loading rate on tensile strength of Nextel™ 720 fiber tows at 1200°C in air and in steam and (2) the experimental investigation of the effects of steam on creep performance of Nextel™ 720 fiber tows at 1100°C and 1200°C in air and in steam. Experimental results are presented and analyzed. A linear elastic crack growth model is used to predict the creep lifetimes from the constant stress rate test data. Finally the Monkman-Grant relationship is applied to creep data obtained for Nextel™ 720 fiber tows at 1200°C in air and in steam.

5.1 Influence of Loading Rate on Tensile Strength of Nextel™ 720 Fiber Tows at 1200°C in Laboratory Air and in Steam

Recall from Section 4.1 that a loading rate dependency of ultimate tensile strength (UTS) for oxide-oxide CMCs has been attributed to environmentally assisted subcritical crack growth in the fiber constituent. To explore this hypothesis a series of constant stress rate tension tests to failure were performed on the Nextel™ 720 fiber tows at 1200°C in laboratory air and in a steam. The experimental setup described in Section 3.2 was employed.

The tensile strength values obtained at 1200°C in laboratory air at stress rates ranging from 10 to 1000 MPa/sec were influenced by the rate of loading. The values of tensile strength obtained at various stress rates are presented in Table 13. As seen in Figure 45, the UTS of the Nextel™ 720 fiber tows obtained at 1200°C in air increases as the stress rate increases from 10 to 1000 MPa/sec. However, the dependency becomes weaker above 100 MPa/sec. For comparison, single fiber results by Milz et al [92] were

approximated and are included in Figure 45, even though the subcritical crack growth parameters were not determined in that study as discussed below.

Table 13. Tensile strength values obtained at various constant stress rates for Nextel™ 720 fiber tows at 1200°C in laboratory air

Loading Rate (MPa/sec)	10	100	1000
	338.0	498.6	570.7
	421.9	540.2	602.4
	351.2	575.9	621.1
Average	370.4	538.2	598.1
Standard Deviation	45.1	38.7	25.5

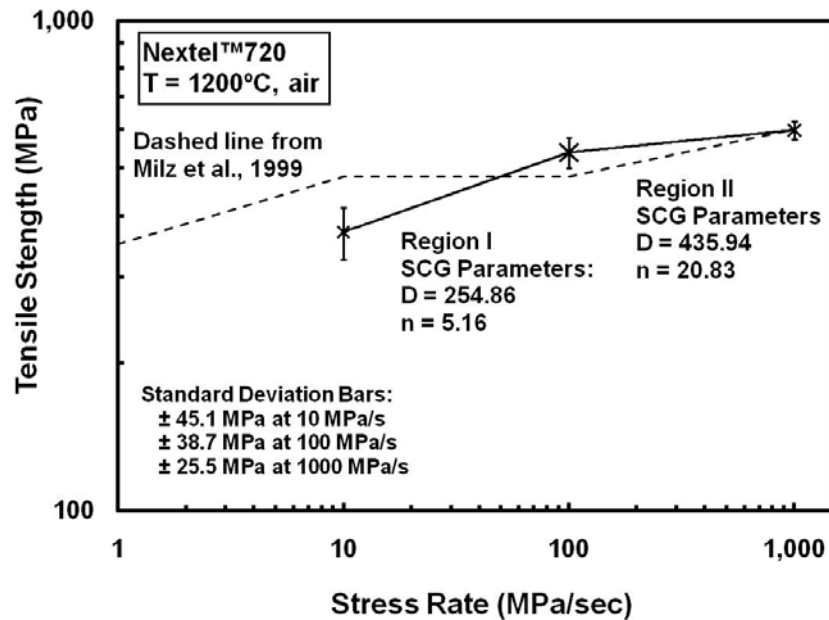


Figure 45. Tensile strength as a function of stress rate for Nextel™ 720 at 1200°C in laboratory air. Effect of loading rate on ultimate tensile strength is evident.

This shift in UTS dependency on stress rate at 100 MPa/sec is likely the result of one of two possibilities. First, as the stress rate increases, eventually the rate of crack growth will become saturated. The corresponding UTS at a fully saturated crack growth rate would be independent of stress rate and would approximately equal the strength in the absence of subcritical crack growth. Under this scenario, the Region II in Figure 45 (from 100 to 1000 MPa/sec) would represent a partially saturated crack growth region that is less dependent upon stress rate, and Region I (from 10 to 100 MPa/sec) would be the best region to determine subcritical crack growth parameters. Similarly, Evans [38, 39] describes the effect of strain rate on fracture strength for subcritical crack growth conditions. A logarithmic plot of strength versus strain rate, similar to Figure 45, can be divided into regions that correspond to a stress intensity factor versus crack length plot. The region of lower strain rate exhibits a linear increase of the logarithm of fracture stress with increasing logarithm of strain rate. In this region, the subcritical crack growth parameters can be calculated. As the rate increases, the slope decreases and the fracture strength approaches the stress expected in the absence of subcritical crack growth.

However, a second possibility for the change in UTS dependency on stress rate is that Region I may be significantly influenced by creep damage at the lowest stress rates. It would therefore be incorrect to use Region I for calculating subcritical crack growth parameters, resulting in Region II as the best region to determine subcritical crack growth parameters. A similar behavior was previously described by Milz et al. [92] for single filaments of Nextel™720 at 1000-1100°C. However, Milz did not determine subcritical crack growth parameters at 1200°C due to the suspicion that all strength values were

influenced by creep damage. For the current study, both Region I and Region II, as depicted in Figure 45 for 1200°C in air, were independently considered.

In contrast, the tensile strength values produced in monotonic tension tests of the NextelTM 720 fiber tows conducted at 1200°C in steam were weakly influenced by the rate of loading over the entire range. The values of tensile strength obtained at various stress rates are presented in Table 14. As seen in Figure 46, the UTS of the NextelTM 720 fiber tows obtained at 1200°C in steam increases consistently as the stress rate increases from 3 to 1000 MPa/sec.

The weak dependency of UTS on stress rate represents a reduced susceptibility of the material on subcritical crack growth. Through additional analysis, namely the determination of the subcritical crack growth parameter, predictions for creep lifetimes can be determined from the monotonic tension experiments. Subcritical crack growth parameters are determined in the next section. These values are then used to make creep lifetime predictions, which are compared to creep results in Sections 5.3 and 5.5 in air and in steam, respectively.

Table 14. Tensile strength values obtained at various constant stress rates for Nextel™720 fiber tows at 1200°C in steam environment

Loading Rate (MPa/sec)	3	10	100	1000
	442.4	470.9	572.4	534.8
	532.0	543.5	486.3	580.9
		494.5	523.5	
Average	487.2	503.0	527.4	557.8
Standard Deviation	63.4	37.0	43.2	32.6

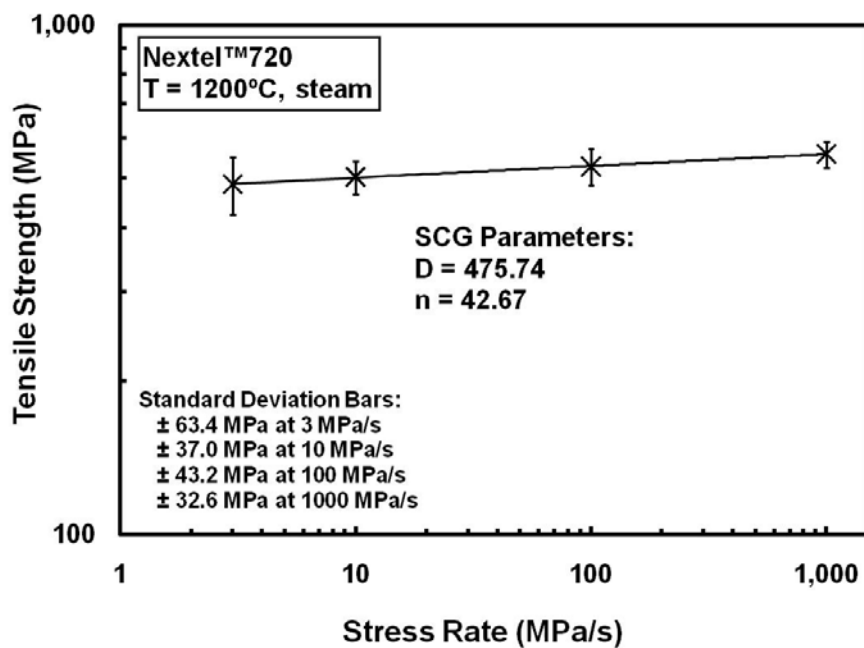


Figure 46. Tensile strength as a function of stress rate for Nextel™720 fiber tow at 1200°C in steam. Effect of loading rate on ultimate tensile strength is evident.

5.1.1 Determination of Subcritical Crack Growth Parameters for Nextel™720 Fiber Tows at 1200°C in Laboratory Air and in Steam

The dependence of tensile strength on stress rate in ceramics was previously discussed in Section 4.1.1. Following the procedure outlined in Section 4.1.1, the experimental results obtained for the Nextel™720 fiber tows at 1200°C in air and in steam were employed to calculate the subcritical crack growth parameters.

For the tests performed in laboratory air, both regions previously described were analyzed independently. In the region from 10 to 100 MPa/sec (Region I), the subcritical crack growth parameters $n = 5.16$ and $D = 254.86$ were determined. In the region from 100 to 1000 MPa/sec (Region II), the subcritical crack growth parameters $n = 20.83$ and $D = 435.94$ were determined. For the test performed in the steam environment, the subcritical crack growth parameters $n = 42.67$ and $D = 475.74$ were determined over the entire range of 3 to 1000 MPa/sec. As presented in Section 5.1, the dependency of UTS on the stress rate in steam was weaker than the dependency of the Nextel™610 fiber tows as presented in Chapter 4. The larger value of n for the Nextel™720 fiber tows in the steam environment represents less susceptibility to subcritical crack growth.

5.2 Creep of Nextel™720 Fiber Tows at 1100°C and 1200°C in Laboratory Air

Creep experiments of Nextel™720 ceramic fiber tows were performed at 1100°C and 1200°C in laboratory air utilizing the experimental setup described in Section 3.2. Initially, creep experiments for Nextel™720 fiber tows were performed at the maximum recommended operating temperature of 1200°C. However, as will be described later in this section and in Section 5.4, a transition in creep performance for different creep

stresses was discovered. Therefore, the test temperature was dropped to 1100°C in order to investigate this behavior further.

Results of the creep-rupture tests conducted at 1100°C in laboratory air are summarized in Table 15. Representative creep curves obtained at 1100°C in laboratory air are shown in Figure 47. Note that the level of noise in the creep curves for NextelTM720 is of the same order for NextelTM610 in Chapter 4. The appearance of additional noise is simply due to an order of magnitude higher resolution on the strain scale for NextelTM720. Creep curves produced in all tests conducted in air exhibit primary and secondary creep regimes. Tertiary creep was not evident for NextelTM720 at 1100°C. Transition from primary to secondary creep occurred early in the creep life. The accumulated creep strains were very small even at high stresses. Creep run-out of 100 hours was achieved in one of the 400 MPa tests as well as at 350 and 375 MPa.

Table 15. Summary of creep-rupture results for the Nextel™720 fiber tows at 1100°C in laboratory air

Creep Stress (MPa)	Maximum Strain (%)	Time to Rupture (min)	Steady-State Creep Rate (s ⁻¹)
350	0.2 †	>6000 †	1.15x10 ⁻⁹
375	0.3 †	>6000 †	1.29x10 ⁻⁹
400	0.2 †	>6000 †	1.58x10 ⁻⁹
400	0.4	1236	2.63x10 ⁻⁸
425	0.4	203	2.25x10 ⁻⁸
450	0.4	126	7.76x10 ⁻⁸
450	‡	N/A	1.19x10 ⁻⁸
450	‡	N/A	3.23x10 ⁻⁹
500	‡	N/A	3.18x10 ⁻⁸

† Run-out

‡ Experiment was interrupted before failure

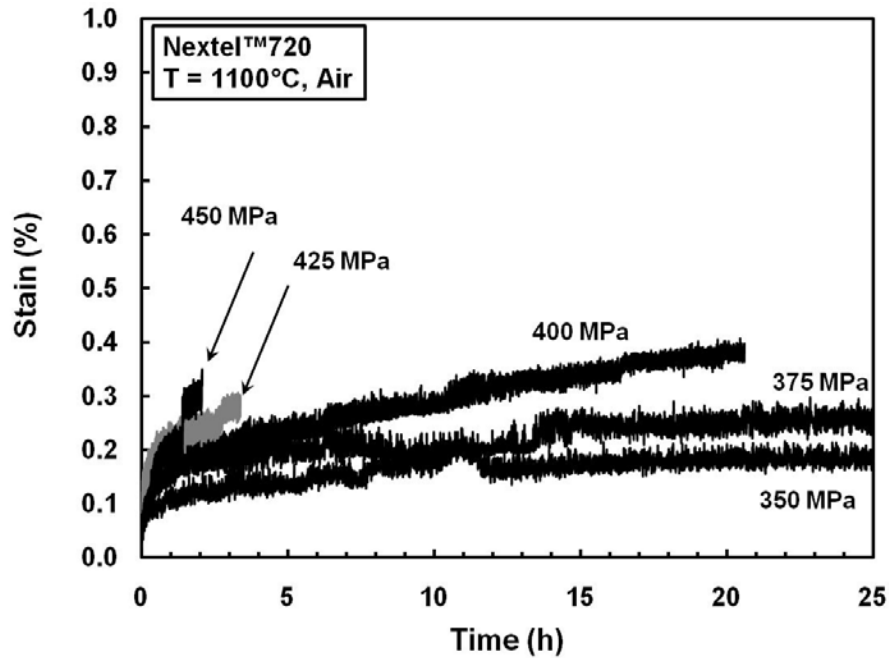


Figure 47. Creep strain vs. time curves for Nextel™720 fiber tows at 1100°C in laboratory air

Results of the creep-rupture tests conducted at 1200°C in laboratory air are summarized in Table 16. Representative creep curves obtained at 1200°C in laboratory air are shown in Figure 48. Creep curves produced in all tests conducted in air exhibit primary and secondary creep regimes. In many cases, tertiary creep was also evident. Transition from primary to secondary creep occurred early in the creep life. The accumulated creep strain was again quite small as compared to the Nextel™610 from the previous chapter and decreased as the applied stress increased from 300 to 400 MPa. Similar creep strains were accumulated in the 400 to 500 MPa tests. Creep run-out of 100 hours was achieved in the 100 and 200 MPa tests.

Table 16. Summary of creep-rupture results for the Nextel™720 fiber tows at 1200°C in laboratory air

Creep Stress (MPa)	Maximum Strain (%)	Time to Rupture (min)	Steady-State Creep Rate (s ⁻¹)
100	0.2 †	>6000 †	2.94x10 ⁻⁹
200	0.4 †	>6000 †	7.28x10 ⁻⁹
200	0.4 †	>6000 †	6.90x10 ⁻⁹
300	2.6	5801	2.60x10 ⁻⁸
300	1.6	3622	2.81x10 ⁻⁸
350	0.8	200	6.79x10 ⁻⁷
400	0.5	38	1.18x10 ⁻⁶
400	0.4	22	1.69x10 ⁻⁶
450	0.5	28	1.37x10 ⁻⁶
450	0.4	11	2.70x10 ⁻⁶
500	0.2	3	4.93x10 ⁻⁶

† Run-out

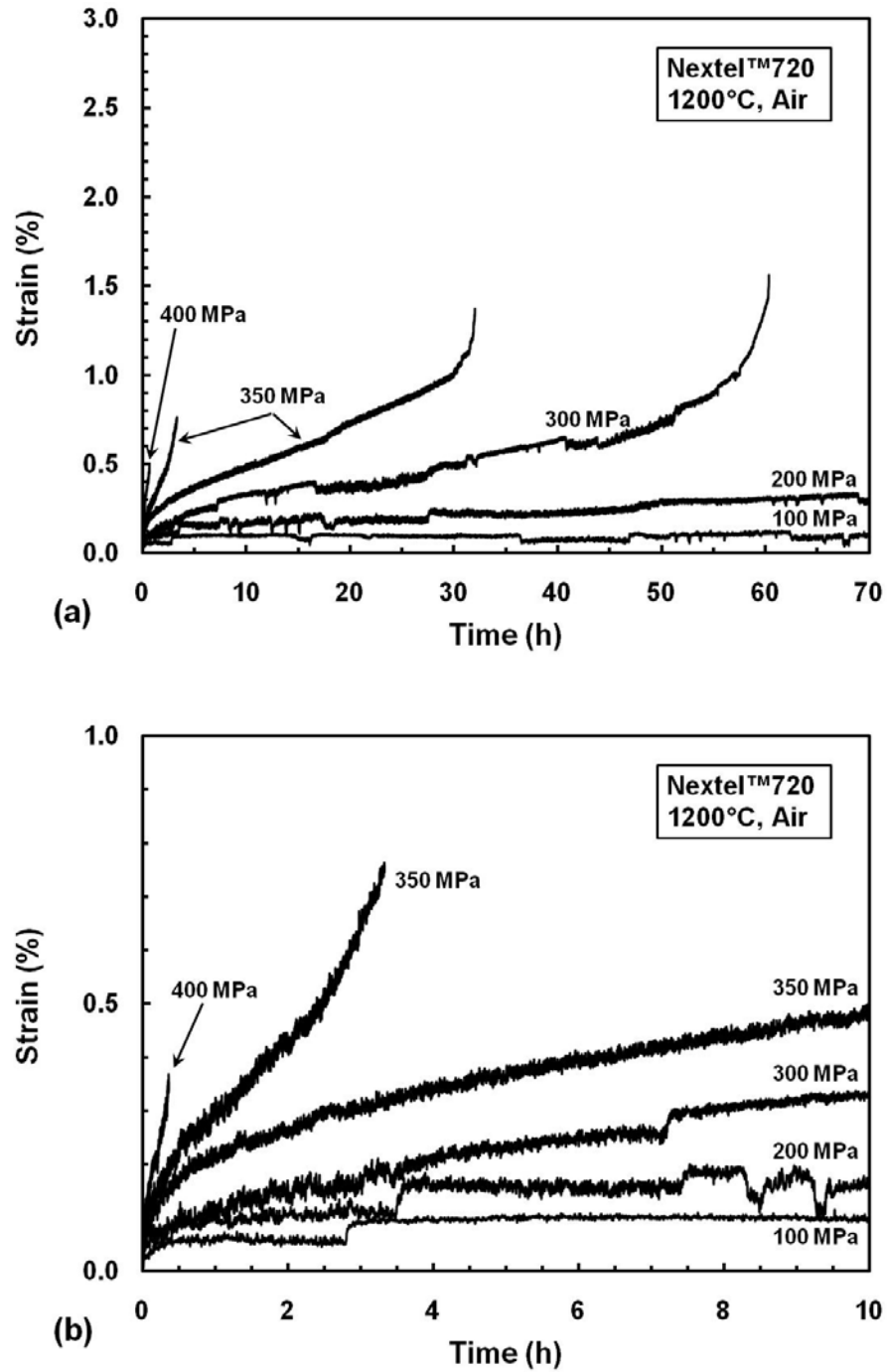


Figure 48. Creep strain vs. time curves for Nextel™720 fiber tows at 1200°C in laboratory air: (a) scale 0-3%, 0-70 h, (b) 0-1%, 0-10 h

Comparing with the creep experiments of Nextel™ 610 from the previous chapter, the accumulated strains for Nextel™ 720 fiber tow were much lower. Even with the increased maximum recommended operating temperature of 1200°C for Nextel™ 720 as compared to 1100°C for Nextel™ 610, the creep strains for Nextel™ 720 were approximately one order of magnitude less for the stresses that resulted in failure. In this regard, the Nextel™ 720 fiber tow outperformed the Nextel™ 610 fiber tow.

Steady-state creep rate was reached in all experiments and dominated the majority of the creep lifetime. Creep rate as a function of applied stress for both 1100°C and 1200°C is presented in Figure 49. In addition, the expression developed by Deléglise et al [33] for creep of Nextel™ 720 at 1200°C from their fiber bundle data is included in Figure 49, along with single filament results from Wilson[161] at 1100°C and 1200°C.

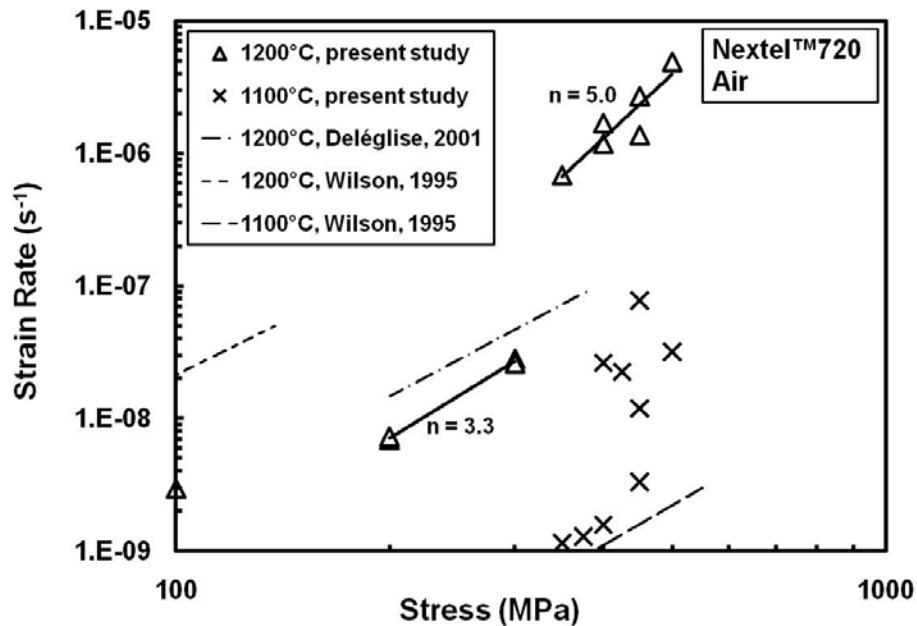


Figure 49. Steady-state creep rate as a function of applied stress for Nextel™ 720 at 1100°C and 1200°C in laboratory air

The steady-state creep rates for both 1100°C and 1200°C creep experiments clearly divide into two distinct modes with respect to creep stresses. For 1100°C experiments, a shift in the creep rate dependency on stress occurred at 400 MPa. For 1200°C experiments, a shift in the creep rate dependency on stress occurred at 300 MPa. Fitting the creep results obtained for the for NextelTM720 fiber tows at 1200°C in laboratory air with the power-law equation described earlier in Sections 2.4 and 4.2 yields a stress exponent $n = 3.3$ for creep stresses ≤ 300 MPa. This value of the stress exponent is consistent with previous results of $n \approx 3$ described in Sections 2.3 and 2.4. Therefore, the dominate creep mechanism is consistent with the previously reported interface-reaction controlled creep.

However for stresses greater than 300 MPa, the stress exponent increased to $n = 5.0$, which has not been previously reported for NextelTM720. All previous studies have not reported creep results of NextelTM720 in the region of this transition for either temperature with the exception of Deléglise et al [33], which had a maximum creep stress of 380 MPa. Nevertheless, a similar shift in creep behavior has been previously documented for several ceramics [16, 23, 24, 59, 158] and superplastic metallic alloys [25]. This shift in the steady-state creep rate with respect to creep stress is due to a shift in the creep mechanism. Recalling Table 3 from Section 2.4, the higher stress creep mechanism is likely attributed to dislocation creep or possibly void growth. Due to the very low creep rates and lack of data attained at lower stresses for the experiments at 1100°C, stress exponents were not calculated. However, a qualitative parallel in behavior is present for NextelTM720 fiber tows where the stress exponent transition region is shifted

to approximately 400 MPa at 1100°C, as compared to the transition at 300 MPa for 1200°C.

Additionally, the stress-rupture behavior at 1100°C and 1200°C in laboratory air is summarized in Figure 50. As expected, the creep lifetime decreases with increasing applied stress.

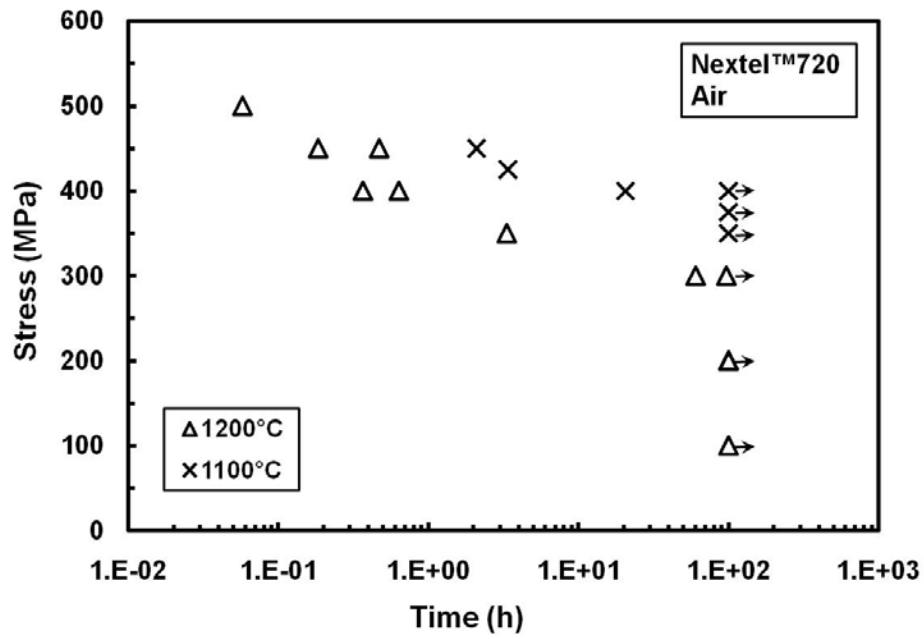


Figure 50. Creep stress vs. time to rupture for Nextel™720 fiber tows at 1100 and 1200°C in laboratory air. Arrows indicates that failure of specimens did not occur when the test was terminated.

5.3 Predicting Creep Lifetimes from Constant Stress Rate Test Data for Nextel™ 720 Fiber Tows at 1200°C in Air

From Section 4.4, the time to failure under a constant tensile stress (creep lifetime) was derived utilizing the subcritical crack growth parameters using the linear elastic crack growth model. The time to failure under a constant tensile stress, given in Equation 29, represents the time required for a flaw to grow from an initial, subcritical size to a dimension critical for catastrophic crack propagation to occur. The subcritical crack growth parameters n and D calculated Section 5.1.1 from the constant stress-rate data for Nextel™ 720 fiber tows at 1200°C in air were used to predict creep lifetimes for creep stresses ranging from 100 to 500 MPa. The predicted creep lifetimes for both Region I and Region II described in Section 5.1.1 are listed in Table 17 below and are compared with experimental creep results in Figure 51, where the predictions are shown as solid lines.

Table 17. Creep lifetime predicted from constant stress-rate data for Nextel™ 720 fiber tows at 1200°C in air

Creep Stress	100 MPa	200 MPa	300 MPa	400 MPa	500 MPa	SCG Parameters
Time to Rupture (min)	86.12	2.41	0.30	0.07	0.02	Region I $n = 5.16$, $D = 254.86$
Time to Rupture (min)	6.94×10^{12}	3.72×10^6	799.92	2.00	0.02	Region II $n = 20.83$, $D = 435.94$

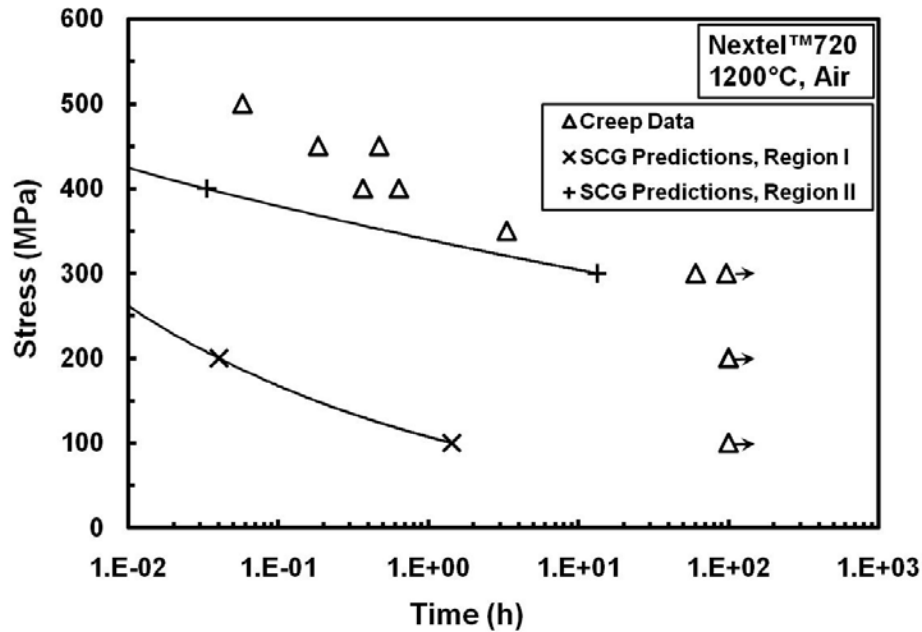


Figure 51. Creep lifetime data compared subcritical crack growth predictions for Nextel™720 tows in air at 1200°C

As previously mentioned, Milz et al. [92] concluded that the fracture behavior of Nextel™ 720 single filaments at 1200°C in air could not be characterized by subcritical crack growth due to observed non-linear elastic mechanical behavior. They assumed that fracture was strongly controlled by creep damage at 1200°C in air.

From Figure 51, Region II predictions are clearly closer to the creep data than Region I. However, this prediction is not as definitive as the previous results of Nextel™ 610 in steam from Chapter 4. Furthermore, a single set of subcritical crack growth parameters could not be determined across a large range of stress rates. Nonetheless, subcritical crack growth of Nextel™720 fiber tows may still be a factor failure mechanism in air at 1200°C {{57 Deléglise,F. 2001}}.

Although the predictions for creep lifetimes of NextelTM720 tows in air at 1200°C are less conclusive, the results for NextelTM720 tows in steam at 1200°C are significantly different. Recall from Section 5.1 that the increase in ultimate tensile strength of NextelTM720 tows in steam at 1200°C weakly but consistently increased with increasing stress rate. Therefore, a single set of subcritical crack growth parameters were determined across the range of 3 to 1000 MPa/sec. These results are compared to creep data in Section 5.5 following the creep results of NextelTM720 tows in steam at 1200°C in the following section.

5.4 Creep of NextelTM720 Fiber Tows at 1100°C and 1200°C in Steam Environment

Several studies by Ruggles-Wrenn et al. [125, 126, 128, 129, 131] revealed a degrading influence of steam on high-temperature creep performance of oxide-oxide CMCs reinforced with NextelTM720 fibers. Results revealed that reduced creep lifetimes and accelerated creep rates were produced in the presence of steam. Fiber degradation was attributed as the likely source of composite degradation. In the current study, creep experiments were performed at 1100°C and 1200°C in steam on the NextelTM720 ceramic fiber tows alone in order to evaluate the effects of steam on creep behavior of the fibers.

Creep experiments of NextelTM720 ceramic fiber tows were performed at 1100°C and 1200°C in steam environment utilizing the experimental setup described in Section 3.2. Results of the creep-rupture tests conducted at 1100°C in steam are summarized in Table 18. Representative creep curves obtained at 1100°C in steam are shown in Figure 52. Creep curves produced in all tests conducted in steam exhibit primary and secondary

creep regimes. Tertiary creep was not evident for Nextel™720 at 1100°C. Transition from primary to secondary creep occurred early in the creep life. The accumulated creep strains were again quite small. The 300 MPa test was interrupted after 71 hours, which is represented by the arrow in Figure 52. The steady-state strain rate was very low at $8.98 \times 10^{-9} \text{ s}^{-1}$, and the accumulated strain was 0.43% when the test was interrupted. All attempts at stresses greater than 400 MPa were unsuccessful due to fiber tow failure on loadup.

Table 18. Summary of creep-rupture results for the Nextel™720 fiber tows at 1100°C in steam

Creep Stress (MPa)	Maximum Strain (%)	Time to Rupture (min)	Steady-State Creep Rate (s^{-1})
300	0.43 ‡	>4264 ‡	8.98×10^{-9}
350	0.67	3781	2.30×10^{-8}
400	0.77	3075	2.88×10^{-8}
400	0.64	3754	2.04×10^{-8}

‡ Experiment was interrupted before failure

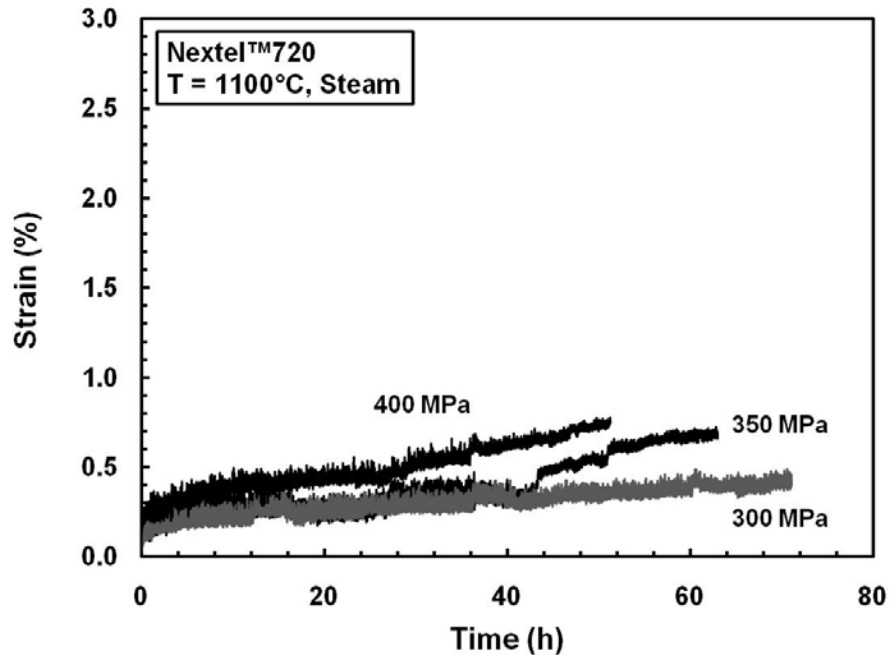


Figure 52. Creep strain vs. time curves for Nextel™720 fiber tows at 1100°C in steam

Similarly, the results of creep-rupture tests conducted at 1200°C in steam are summarized in Table 19. Representative creep curves obtained at 1200°C in steam are shown in Figure 53. Creep curves produced in all tests conducted in steam exhibit primary and secondary creep regimes. In many cases, tertiary creep was also evident. Transition from primary to secondary creep occurred early in the creep life. The accumulated creep strain decreased as the applied stress increased from 100 to 325 MPa. Similar creep strains were accumulated in the 350 to 400 MPa tests. Creep run-out of 100 hours was achieved in only one of the 100 MPa tests. All attempts at stresses greater than 400 MPa were unsuccessful due to fiber tow failure on loadup.

Table 19. Summary of creep-rupture results for the Nextel™720 fiber tows at 1200°C in steam

Creep Stress (MPa)	Maximum Strain (%)	Time to Rupture (min)	Steady-State Creep Rate (s ⁻¹)
100	0.7 †	>6000 †	6.01x10 ⁻⁹
100	2.9	4365	1.34x10 ⁻⁸
200	2.3	3361	3.41x10 ⁻⁸
200	2.3	2663	4.69x10 ⁻⁸
300	2.0	1182	1.28x10 ⁻⁷
300	2.3	1165	1.36x10 ⁻⁷
325	0.8	209	2.95x10 ⁻⁷
350	0.6	116	7.37x10 ⁻⁷
400	0.6	39	1.37x10 ⁻⁶

† Run-out

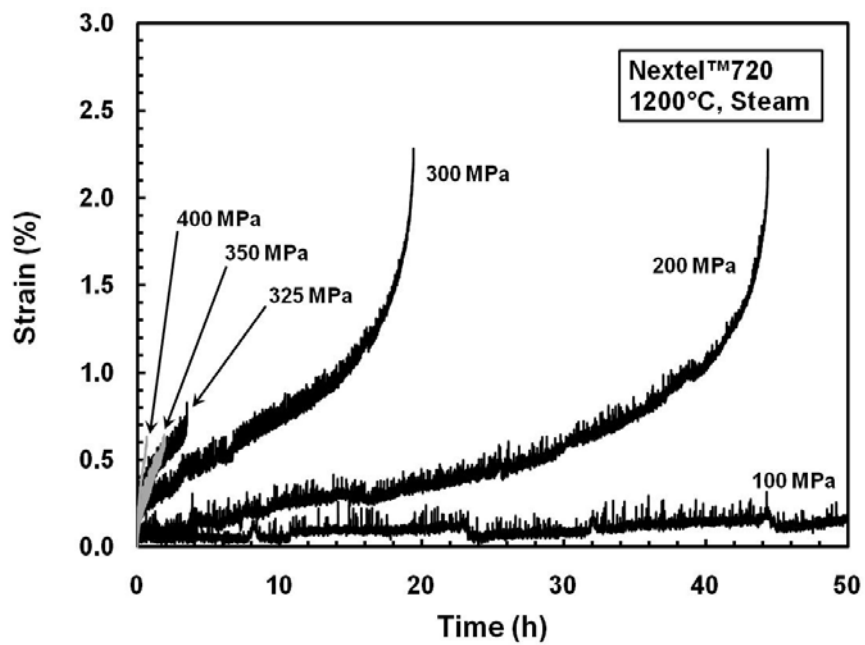


Figure 53. Creep strain vs. time curves for Nextel™720 fiber tows at 1200°C in steam

For the test temperature of 1200°C in steam, the creep strains of the Nextel™720 fiber tow increased over the 1100°C experiments. Nevertheless, these creep strains were still quite small. Moreover, tertiary creep became prevalent in Nextel™720 fiber tow at 1200°C in steam for creep stresses ranging from 100-300 MPa but was not observed at 1100°C.

Steady-state creep rate was reached in all experiments and dominated the majority of the creep lifetime. Creep rate as a function of applied stress for both 1100°C and 1200°C in air and in steam is presented in Figure 54.

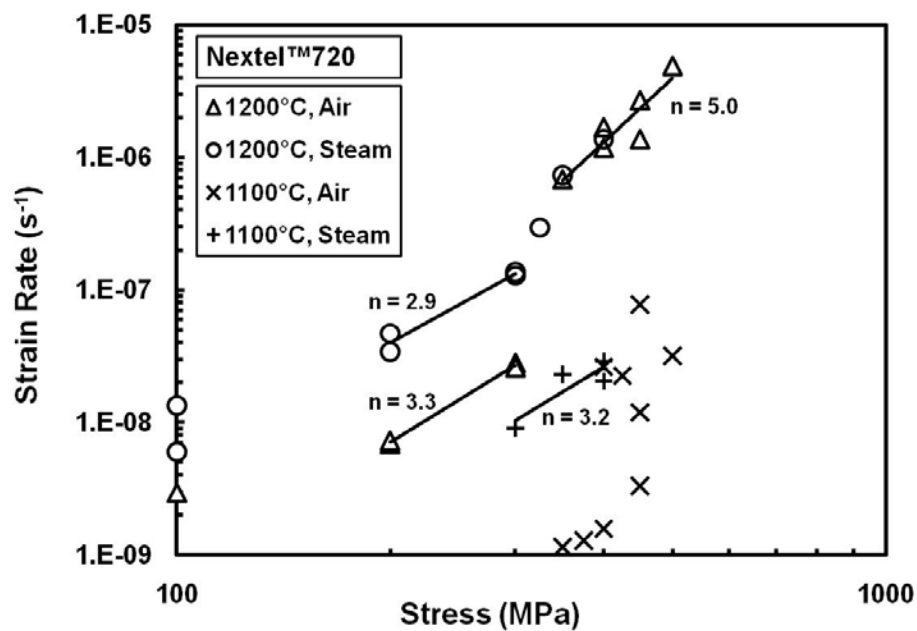


Figure 54. Steady-state creep rate as a function of applied stress for Nextel™720 fiber tows at 1100°C and 1200°C in air and in steam

The steady-state creep rates for both 1100°C and 1200°C creep experiments in air were previously shown to divide into two distinct regions corresponding to distinct

governing creep mechanisms with respect to creep stresses. For 1100°C experiments in steam, the maximum creep stress that resulted in a successful test was 400 MPa. Since no data was obtained above 400 MPa at 1100°C in steam, the shift in the creep rate dependency on stress was not observed at 1100°C in steam. This lack of the second creep mechanism at the lower temperature in steam is likely due to the temperature dependence on the creep rate and the fact that creep experiments for the higher creep stresses were not attainable in steam due to tow failure on loadup. However, a shift in the creep rate dependency on stress occurred above 300 MPa in steam at 1200°C in a similar way as previously demonstrated in laboratory air. Fitting the creep results obtained for Nextel™ 720 fiber tows in steam with the power-law equation described earlier in Sections 2.4 and 4.2 yields a stress exponent $n = 3.2$ for 1100°C. For the stress region ≤ 300 MPa, the stress exponent at 1200°C in steam was $n = 2.9$. These values of the stress exponents are again consistent with previous results described in Sections 2.3 and 2.4. For stresses greater than 300 MPa, the steady-state creep rate in steam becomes more responsive to the applied stress, just as previously described for laboratory air in Section 5.2, and has a stress exponent of $n = 5.0$.

The effect of steam was an increase of steady-state creep rate by approximately one order of magnitude for creep stresses ≤ 300 MPa at 1200°C and for creep stresses less than 400 MPa at 1100°C. At 1200°C, the increase in steady-state creep rate was slightly less than one order of magnitude. Whereas, for 1100°C, the increase in steady-state creep rate was slightly greater than one order of magnitude. However, the creep rates for both air and steam at 1200°C converged above 300 MPa. Therefore, the creep mechanism above 300 MPa is unaffected by steam.

Recall the studies from the beginning of this section where Nextel™720 based CMCs experienced reduced creep resistance in steam. Also, recall the similar study of a Nextel™610 based CMC from Section 4.3 that experienced a two order of magnitude increase in creep rate in the presence of steam. In the case of the Nextel™720 based CMC studies, the increase in creep rate in the presence of steam is less dramatic than it was for the Nextel™610 based CMC. In this case, Nextel™720 contains much more silica than Nextel™610, primarily in the form of mullite. If the previous difference in degraded creep performance of the Nextel™610 based CMC compared to the Nextel™610 fiber tow was a result of grain growth as reasoned in Section 4.3, then the difference between fiber tow and CMC for Nextel™720 would be less simply due to the abundant silica in Nextel™720 and excessive grain growth less likely. Therefore, the increased creep rates in steam for Nextel™720 fiber tow and Nextel™720 based CMC are more similar than for the Nextel™610 case. As was the case for Nextel™610, confirmation of this phenomenon would require microscopy and analysis for both the Nextel™720 fiber tow and the CMC.

Additionally, the stress-rupture behavior at 1100°C and 1200°C in steam is summarized in Figure 55. As expected, the creep lifetime decreases with increasing applied stress. The transition in creep mechanism is also apparent at 300 MPa. Above 300 MPa, the creep lifetimes are similar for either laboratory air or steam at 1200°C. However at ≤ 300 MPa, the creep lifetime in steam is reduced by approximately one order of magnitude.

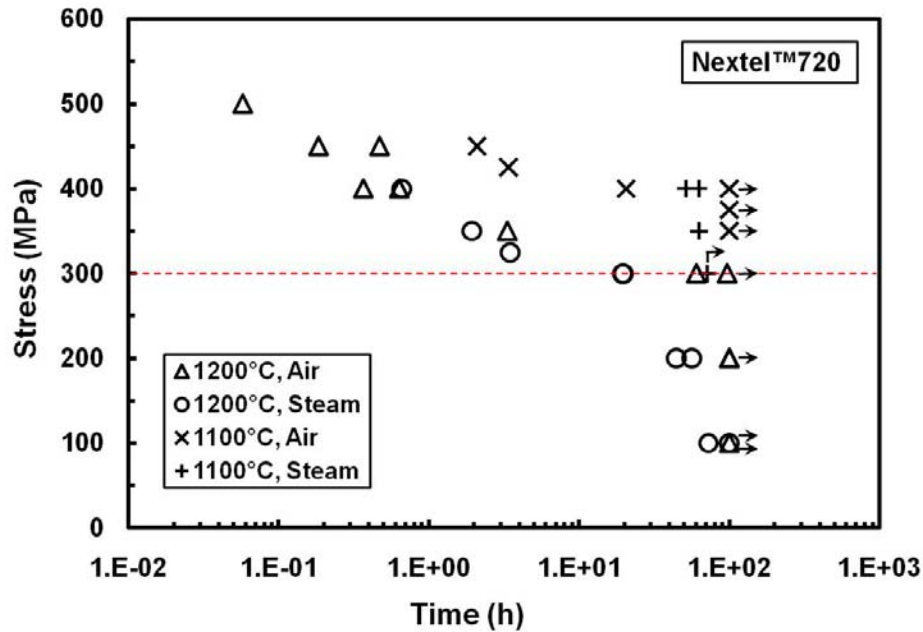


Figure 55. Creep stress vs. time to rupture for Nextel™720 fiber tows at 1100 and 1200°C in laboratory air and steam. Arrows indicates that failure of specimens did not occur when the test was terminated.

The effects of steam on the creep performance of Nextel™720 fiber tow at 1100°C and 1200°C are significant. In the lower stress exponent region of $n \approx 3$, the presence of steam accelerates the steady-state creep rate by approximately one order of magnitude and reduces the creep lifetime of the tow by approximately one order of magnitude. However, the creep mechanism at the higher stress exponent region of $n \approx 5$ becomes independent of the environment.

5.5 Predicting Creep Lifetimes from Constant Stress Rate Test Data for Nextel™ 720 Fiber Tows at 1200°C in Steam

The subcritical crack growth parameters n and D calculated Section 5.1.1 from the constant stress-rate data for Nextel™ 720 fiber tows at 1200°C in steam were used to predict creep lifetimes for creep stresses ranging from 100 to 500 MPa. Predicted creep lifetimes are listed in Table 20 below.

Table 20. Creep lifetime predicted from constant stress-rate data for Nextel™ 720 fiber tows at 1200°C in steam

Creep Load	100 MPa	200 MPa	300 MPa	400 MPa	500 MPa	SCG Parameters
Time to Rupture (min)	1.45×10^{28}	2.08×10^{15}	6.36×10^7	296.82	0.02	$n = 42.67,$ $D = 475.74$

The predicted creep lifetimes are compared with experimental creep results in Figure 56, where the prediction is shown as a solid line. The predicted values from the constant stress-rate experiments overpredict the creep lifetime data at 1200°C in steam. The predictions are reasonable for the higher stress region but do not capture the shift in creep behavior at 300 MPa.

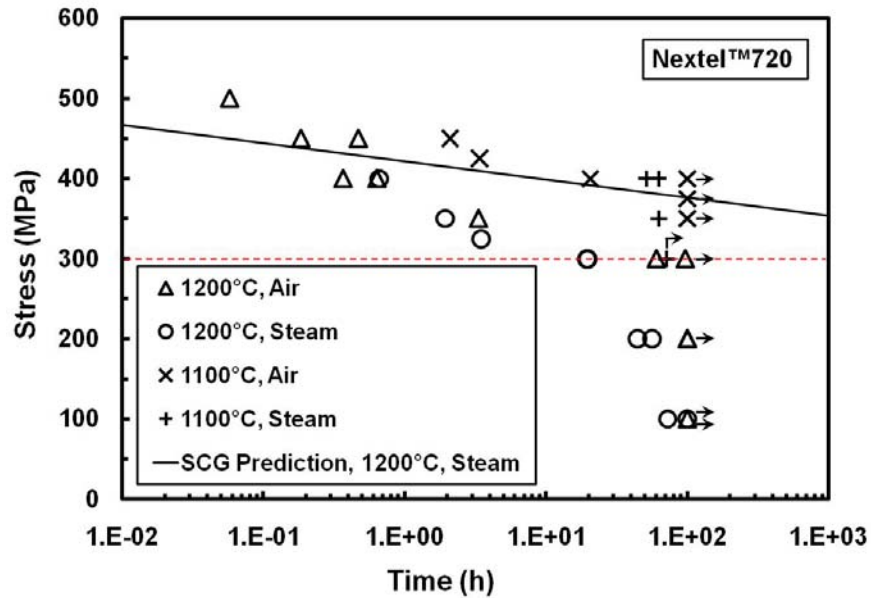


Figure 56. Creep lifetime data compared subcritical crack growth predictions for Nextel™720 tows in steam

Nevertheless, subcritical crack growth of the fiber tow may still be a liable for failure in Nextel™720 tows in steam at 1200°C. The subcritical crack growth in Nextel™720 is likely governed by crack nucleation around flaws along with mullite dissolution, liquid phase formation and alumina growth near the crack tip { {57 Deléglise,F. 2001} }. The complex, two-phase microstructure and the shift in controlling creep mechanism of the Nextel™720 fiber makes predictions from linear elastic fracture mechanics difficult at the extreme operating conditions. Further investigations into the microstructure of tested specimens would be required to more fully understand the microstructural mechanisms responsible for failure of Nextel™720 tows in steam at 1200°C.

5.6 Stress Rupture of Nextel™ 720 Fiber Tow at 1200°C in Air and in Steam and Monkman-Grant Failure Relationship

Recall the empirical Monkman and Grant relationship between creep-rupture life and steady-state creep rate described in Section 4.5. In this section, the Monkman-Grant relationship is examined to establish whether the relationship can be used to predict creep-rupture life of Nextel™ 720 fiber tows at 1200°C in air and, especially, in steam. Recall that at 1200°C the presence of steam had a degrading effect on the creep performance of Nextel™ 720 fiber tows for creep stresses of ≤ 300 MPa. The steady-state creep rates increased by approximately one order of magnitude while the creep lifetimes decreased by approximately one order of magnitude due to steam. However, the creep rates and lifetimes above 300 MPa were independent of the environment. Figure 57 shows a log-log plot of the creep lifetime versus the steady-state creep rate obtain for the Nextel™ 720 fiber tows at 1200°C in air and in steam. It is seen that the data obtained in air and in steam fall along a common line despite the transition in creep behavior at 300 MPa. This result indicates that the Monkman-Grant relationship given by Equation 30 applies, and that the Monkman-Grant constants a and C are independent of the test environment and the change in creep behavior for Nextel™ 720 fiber tows at 1200°C. The fit of the experimental data to Equation 30 (shown as a solid line in Figure 57) was good with the coefficient of correlation in regression of 0.973. The Monkman-Grant constants $a = 1.32$ and $C = 3.50 \times 10^{-5}$ were determined from the experimental data by a linear regression analysis.

Furthermore in a similar manner as in Section 4.5, creep-rupture data at 1200°C from CMCs utilizing the Nextel™ 720 fiber are compared to the fiber tow data in Figure

57. Note, the CMC data from Ruggles-Wrenn et al [128] was conducted in air, steam and argon environments. Reasonable agreement exists between the CMC creep-rupture data and the fiber tow data.

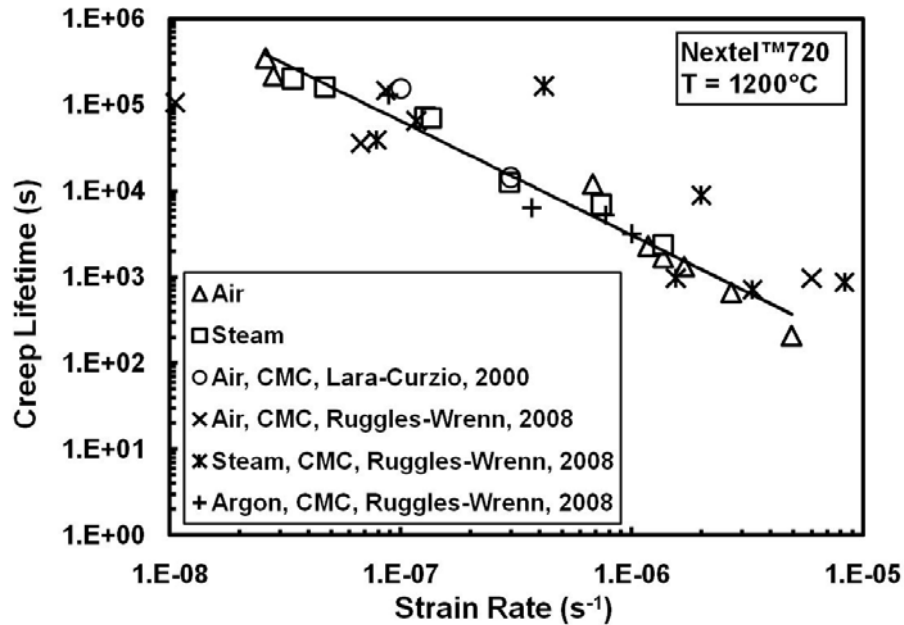


Figure 57. Monkman-Grant plot of creep lifetime vs. steady-state strain rate for Nextel™720 at 1200°C in laboratory air, steam and argon

As was the case in Section 4.5 for Nextel™610 fiber tows, the Monkman-Grant relationship can be utilized to predict creep-rupture for the Nextel™720 fiber tows in air and in steam. Additionally as discussed in Section 4.5, the Monkman-Grant relationship may also accurately predict creep-rupture for CMCs based on Nextel™720 fiber from the fiber data alone. However, note the cautions as previously discussed in Section 4.5.

5.7 Summary of the Effects of Steam on the Mechanical Behavior of Nextel™ 720 Fiber Tows at 1100 and 1200°C

This chapter demonstrated the effects of steam on the mechanical properties of Nextel™ 720 fiber tows. Creep rates and creep lifetimes were determined at 1100 and 1200°C in both air and in steam environments. For creep stresses ≤ 300 MPa at 1200°C and ≤ 400 MPa at 1100°C, the stress exponent of $n \approx 3$ indicates that the dominant creep mechanism is interface-reaction controlled creep. In steam, the creep mechanism did not change. However, the creep rates in steam increased by one order of magnitude over that of air, while the creep lifetime decreased by one order of magnitude. Therefore, the effects of steam have a dramatic effect on diffusion transport of the interface-reaction controlled creep of Nextel™ 720 f or creep stresses ≤ 300 MPa at 1200°C.

For creep stresses above 300 MPa, a shift in the creep mechanism was observed. Based on the stress exponent $n = 5$, the dominate mechanism is likely that of dislocation creep or possibly void growth. In this region, the creep mechanism was independent of the testing environment.

Additionally, the predictions for creep lifetime based on subcritical crack growth were calculated from monotonic tension tests in air and in steam. Results were inconclusive whether the environmentally assisted subcritical crack growth is the dominant failure mechanism of Nextel™ 720 fiber tow at 1200°C.

Finally, the Monkman-Grant relationship was examined for creep-rupture life of Nextel™ 720 in air and in steam at 1200°C. The Monkman-Grant relationship was discovered to be independent of the test environment and may be used to accurately predict creep-rupture for Nextel™ 720 fiber tow. However, the applicability of the

Monkman-Grant relationship base on fiber data to CMCs must be used with caution as discussed in Chapter 4.

VI. Creep Behavior of Polycrystalline Alumina (Al_2O_3) at 1100 and 1300°C

This chapter describes the compressive creep performance of polycrystalline alumina (Al_2O_3) at 1100 and 1300°C in air and in steam environments. The results obtained for bulk polycrystalline alumina provide a basis for comparison with the results obtained for Nextel™ 610 fiber tow as well as with the results obtained for the bulk polycrystalline YAG. The effects of steam environment and of silica (SiO_2) doping on creep performance of high-purity polycrystalline alumina at 1100°C and at 1300°C were examined. The results produced at 1100°C are compared with the creep results obtained for Nextel™ 610 fiber tows at 1100°C from Chapter 4, and the results produced at 1300°C are compared to the results obtained for the polycrystalline YAG (see Chapter 7).

Compressive creep experiments of bulk polycrystalline alumina with and without silica doping were performed at 1100°C and at 1300°C in laboratory air and in steam. Details on the alumina specimens are provided in Section 3.1. The facility used to test the bulk alumina specimens is described in Section 3.3.

6.1 Compressive Creep of Polycrystalline Alumina at 1100°C in Laboratory Air

Compressive creep experiments of bulk polycrystalline alumina with and without silica doping were performed at 1100°C in laboratory air. Results of the creep experiments performed on the polycrystalline alumina at 1100°C in laboratory air are summarized in Table 21. Compressive creep curves obtained at 1100°C in air for alumina and for the silica doped alumina are presented Figure 58 and Figure 59, respectively. In all tests, specimen failure did not occur when the test was interrupted.

Table 21. Summary of creep results for polycrystalline alumina at 1100°C in laboratory air

Specimen Number / Type	Creep Stress (MPa)	Steady-State Creep Rate (s^{-1})
Specimen 7 – undoped	100	4.22×10^{-7}
Specimen 7 – undoped	150	7.05×10^{-7}
Specimen 7 – undoped	200	9.92×10^{-7}
Specimen 7 – undoped	250	1.20×10^{-6}
Specimen 10 – SiO ₂ doped	100	2.57×10^{-8}
Specimen 10 – SiO ₂ doped	150	4.64×10^{-8}
Specimen 10 – SiO ₂ doped	200	2.67×10^{-8}
Specimen 10 – SiO ₂ doped	250	5.04×10^{-8}

Creep curves produced in all tests conducted at 1100°C in air exhibit primary and secondary creep regimes. Transition from primary to secondary creep occurred early in the creep life. Generally the steady-state creep rates increased with increasing creep stress magnitudes. The silica doped alumina exhibited less creep compared to the undoped alumina specimens. However, this preliminary comparison of the creep rates produced by polycrystalline alumina with and without silica doping does not take into account the different grain sizes of the two materials. The grain sizes of the two materials are analyzed, and a comparative analysis of the compressive creep rates of the silica doped to undoped alumina that takes into account the different grain sizes is discussed in detail in Section 6.3.

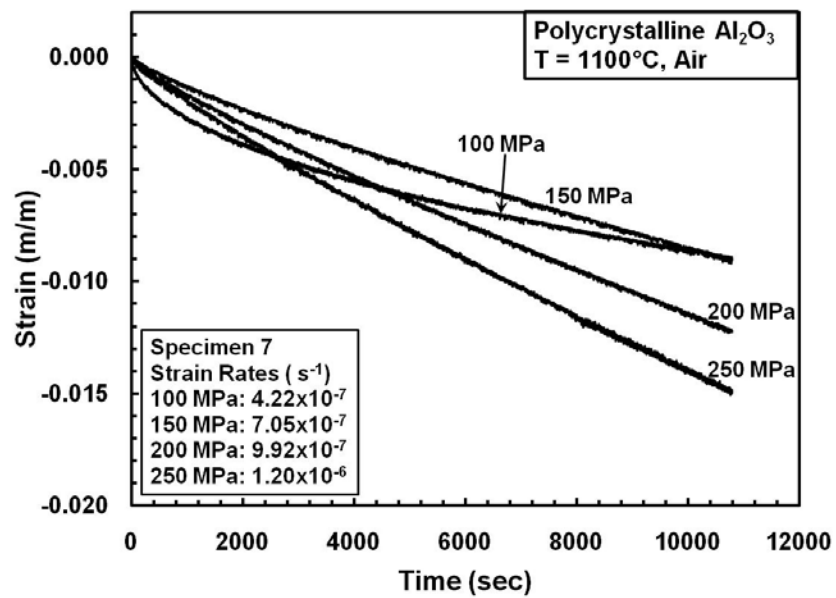


Figure 58. Creep strain vs. time curves for polycrystalline alumina at 1100°C in laboratory air

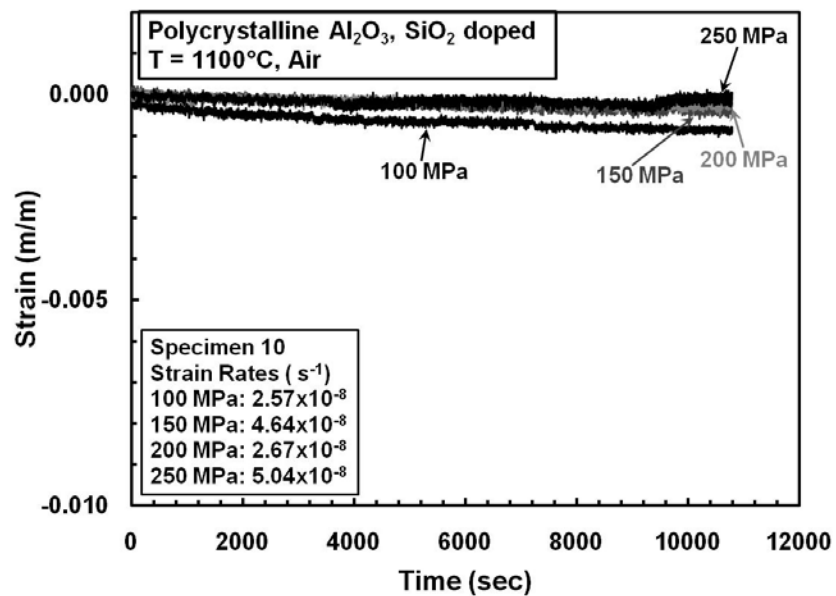


Figure 59. Creep strain vs. time curves for silica doped polycrystalline alumina at 1100°C in laboratory air.

6.2 Compressive Creep of Polycrystalline Alumina at 1100°C in Steam

Compressive creep experiments of bulk polycrystalline alumina with and without silica doping were performed at 1100°C in steam. Results of the creep experiments performed on the polycrystalline alumina at 1100°C in steam are summarized in Table 22. Compressive creep curves obtained at 1100°C in steam for alumina and for the silica doped alumina are presented in Figure 60 and Figure 61, respectively. In all tests, specimen failure did not occur when the test was interrupted.

Table 22. Summary of creep results for polycrystalline alumina at 1100°C in steam

Specimen Number / Type	Creep Stress (MPa)	Steady-State Creep Rate (s^{-1})
Specimen 6 – undoped	100	3.20×10^{-7}
Specimen 6 – undoped	150	5.88×10^{-7}
Specimen 6 – undoped	200	7.64×10^{-7}
Specimen 6 – undoped	250	1.05×10^{-6}
Specimen 8 – SiO ₂ doped	100	1.60×10^{-8}
Specimen 8 – SiO ₂ doped	150	2.54×10^{-8}
Specimen 8 – SiO ₂ doped	200	2.72×10^{-8}
Specimen 8 – SiO ₂ doped	250	8.65×10^{-8}

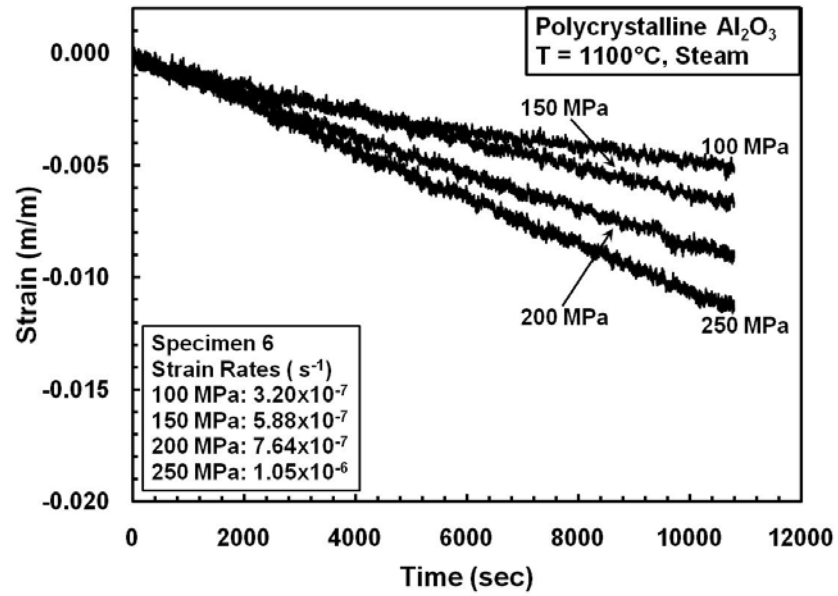


Figure 60. Creep strain vs. time curves for polycrystalline alumina at 1100°C in steam

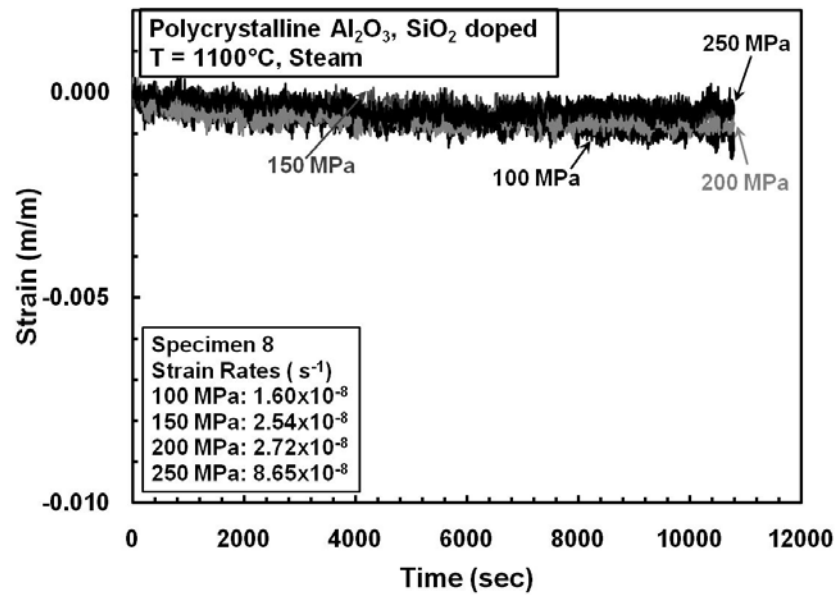


Figure 61. Creep strain vs. time curves for silica doped polycrystalline alumina at 1100°C in steam

Creep tests conducted at 1100°C in steam exhibit similar trends and regimes as was reported in Section 6.1 for 1100°C in air. Likewise, the comparison of creep for the silica doped alumina to the undoped alumina that takes into account the grain size information is presented in Section 6.3. The steady-state (minimum) creep rate was reached in all experiments and dominated the majority of the creep lifetime for all specimens. The steady-state creep rates (prior to grain size correction) as a function of applied stress are presented in Figure 62.

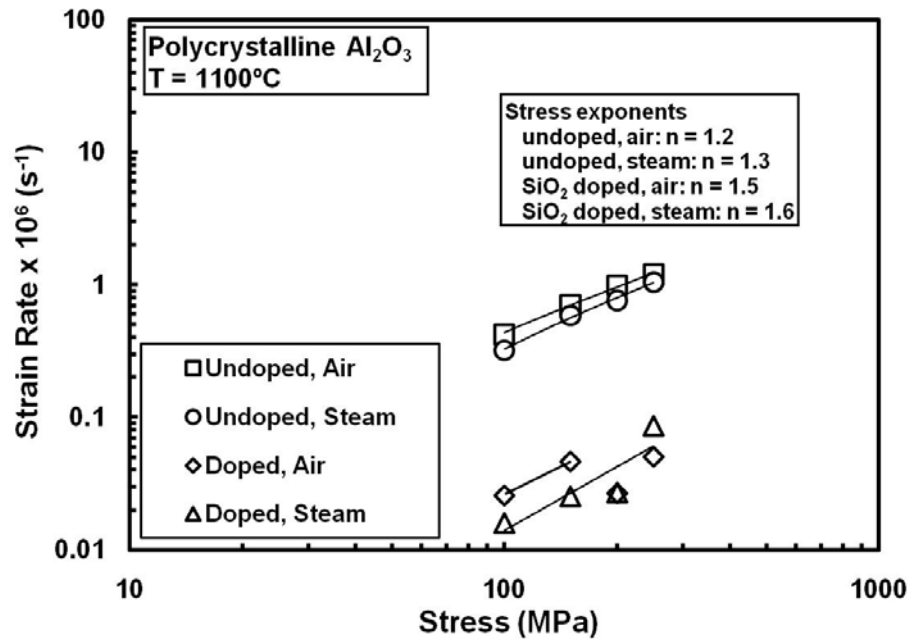


Figure 62. Steady-state creep rate as a function of applied stress for polycrystalline alumina and for silica doped polycrystalline alumina at 1100°C in laboratory air and in steam

The most striking result in Figure 62 is that the presence of steam has very little effect on the creep rate at 1100°C of polycrystalline alumina with or without silica doping. This result is opposite to the results reported in Chapter 4 for the Nextel™ 610

alumina fiber tow. The creep rate of Nextel™ 610 fiber tow at 1100°C is compared to the creep rates of the polycrystalline alumina at 1100°C in Figure 63. Recall that at 1100°C the steady-state creep rates of Nextel™ 610 fiber tows increased approximately by one order of magnitude due to the presence of steam and that the dominant creep mechanism for the fiber tow was that of interface-reaction controlled creep. This difference in the effect of steam between the bulk material and fiber is attributed to the different grain sizes and thus different responsible creep mechanisms, which are affected differently by steam.

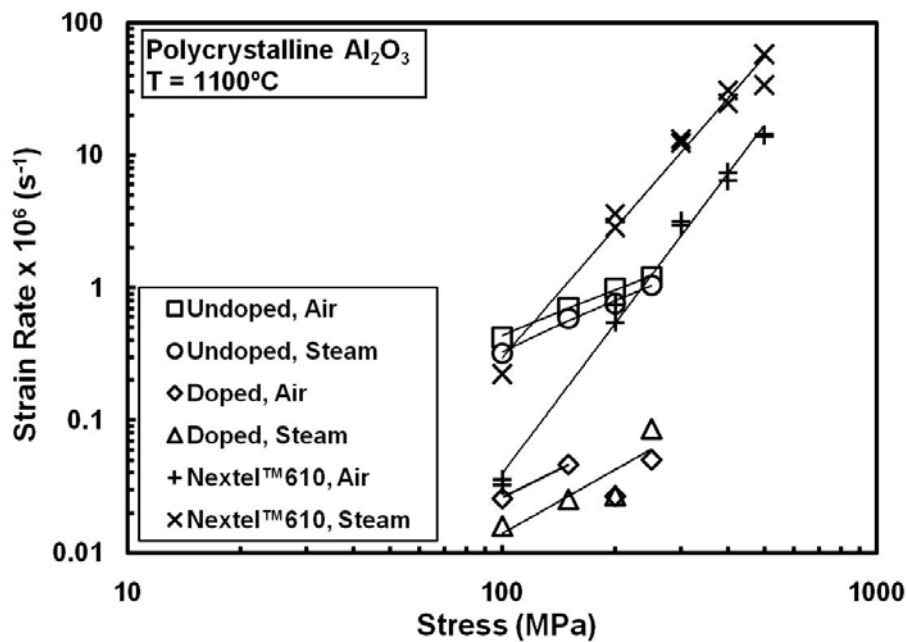


Figure 63. Steady-state creep rates as functions of applied stress of polycrystalline alumina and of Nextel™ 610 fiber tow at 1100°C in laboratory air and in steam

6.3 Effect of Silica Doping on Compressive Creep Rates of Polycrystalline Alumina at 1100°C in Air and Steam

Recall that the steady-state creep rate is proportional to the applied stress, σ , raised to a stress exponent, n , and inversely proportional to the grain size d raised to a grain size exponent, m , such that:

$$\dot{\epsilon} \propto \frac{\sigma^n}{d^m} \quad (31)$$

Plotting the data in Figure 62 as log (strain rate) vs. log (applied stress), the stress exponent, n , was determined by a linear regression analysis for each data set. The stress exponent values for the undoped polycrystalline alumina were 1.2 in air and 1.3 in steam. The stress exponent values for silica doped polycrystalline alumina were 1.5 in air and 1.6 in steam. These values of n are consistent with those reported in literature [15, 17, 164] for alumina of similar grain sizes and suggest a diffusional creep mechanism.

Another observation that can be made when comparing the creep data obtained for the Nextel™ 610 fiber tows to that obtained for the bulk alumina is the difference in stress dependency of the creep rate. Recall that for Nextel™ 610 fiber tows at 1100° C, the stress exponent, n , was determined as 3.4 in air and 2.9 in steam, respectively. For the Nextel™ 610 fibers the stress exponent of approximately 3 has been also reported in literature [12, 50, 162]. This value of n is significantly different from the stress exponents $1.2 \leq n \leq 1.6$ determined for bulk alumina in compression creep in this study. This difference in stress exponents is a result of different underlying creep mechanisms

which is also evident by the large difference in grain sizes. As the grain size decreases, the creep mechanism shifts from the diffusional creep mechanisms of Nabarro-Herring and then Coble creep to the interface-reaction controlled creep for the very fine grain sizes where perfect sources and sinks are no longer assumed.

The average grain size of Nextel™ 610 alumina fibers has been reported at approximately 0.1 μm [10, 12, 50, 162]. Additionally, the interface-reaction controlled creep mechanism, ascribed to the Nextel™ 610 fibers, has a grain size exponent $m = 1$ [50, 161, 162]. The grain sizes of the bulk alumina materials used in this study were measured before creep testing at the Air Force Research Laboratory, Materials and Manufacturing Directorate. Typical optical micrographs of the undoped polycrystalline alumina and of the silica doped polycrystalline alumina are shown in Figure 64 and Figure 65, respectively. Note that, no substantial differences in the optical micrographs were reported for the pre-testing micrographs compared with the post-testing micrographs. The grain size distribution analyses were performed and the grain sizes were determined using a log-normal distribution. The log-normal average grain size and standard deviations were $0.24 \pm 0.15 \log \mu\text{m}$ for the undoped alumina and $0.56 \pm 0.23 \log \mu\text{m}$ for the silica doped alumina. These log-normal average grain sizes equate to 1.7 μm for the undoped alumina and to 3.6 μm for the silica doped alumina. Due to spatial interpretation errors in measuring the grain size from a single section, a stereological correction was applied to the grain sizes by dividing by $\sqrt{3} / 2$. This stereological correction factor is the result of an average distribution of linear section measurements of equiaxial shaped particles. This correction was applied to the previous grain size measurements, which results in an average grain size of 2.0 μm for the undoped alumina

specimens and an average grain size of $4.2\text{ }\mu\text{m}$ for the silica doped alumina specimens. The stereologically corrected grain sizes were used to compare the creep rates obtained for the undoped and for the silica doped specimens.

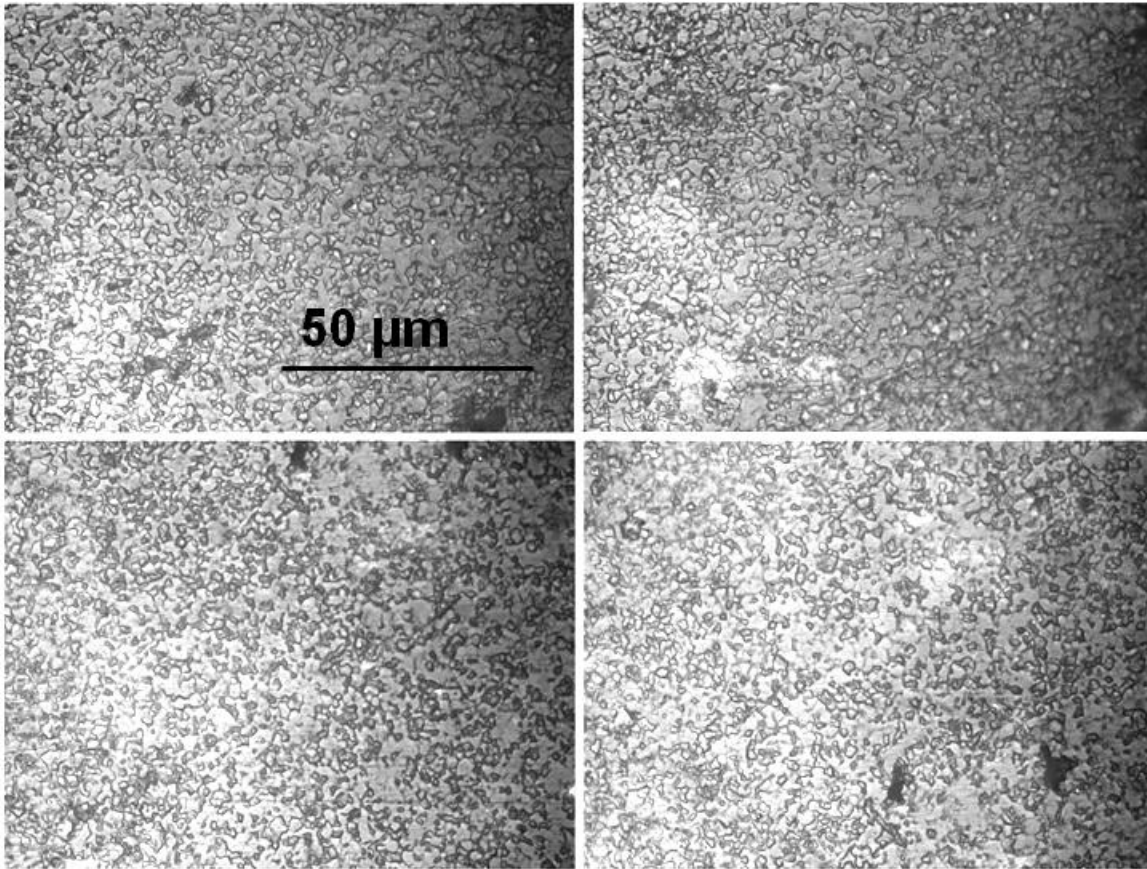


Figure 64. Optical micrographs showing the grain structure of the undoped polycrystalline alumina (micrographs taken before creep testing)

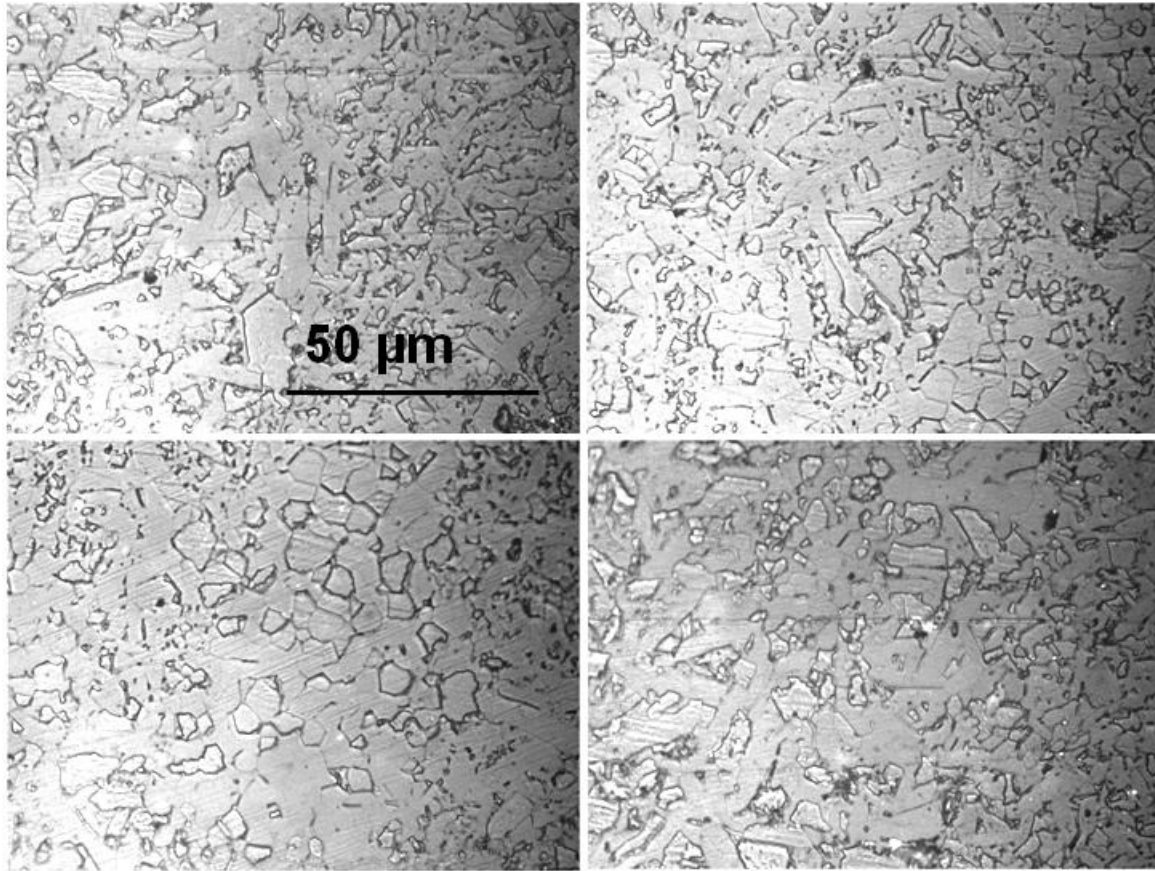


Figure 65. Optical micrographs showing the grain structure of the silica doped polycrystalline alumina (micrographs taken before creep testing)

It is seen that that the undoped alumina and the silica doped alumina have significantly different grain structures. The silica doped alumina contains a mixture of small and large grains with abnormal grain growth. The smaller grains are greater numerically but not in total area. The larger grains tend to be platelets in structure having a large aspect ratio as well as an elongated depth. Conversely, the undoped alumina specimens contain grains that are more equiaxial. The large platelet grains in the silica doped alumina complicate the comparison of silica doped alumina to the undoped

alumina due to the lack of self-similar grain morphology. For example, increased creep resistance has been attributed to large grain aspect ratio and interlocking grain structure [148]. The large platelet grains shown in Figure 65 are therefore likely responsible for the very low creep rates and low accumulated creep strains seen in Figure 59 and Figure 61.

Abnormal grain growth in alumina has been an important research issue since it results in significant degradation of material properties [58, 86]. It is believed that abnormal grain growth in alumina is an extrinsic effect controlled by impurities. However, despite years of study, the mechanism is still poorly understood. Numerous studies have demonstrated that abnormal grains readily grow in alumina with even very low concentrations of silica [7]. Some techniques used to suppress abnormal grain growth include: ultrapure sintering [8], compensating codoping [86], and doping with MgO [56].

In this study, the differences in the grain morphology of the silica doped alumina and undoped alumina complicate the comparison of creep results. Despite the lack of an ideal self-similar grain morphology of the doped to undoped specimens, an analysis of the steady-state creep rates, which takes into account the different average grain sizes of the two materials, is presented below.

In order to compare the creep rates produced by specimens with different grain sizes, the creep mechanisms must first be determined. Utilizing the correct creep mechanism with the applicable grain size exponent will allow a grain size normalization of the creep rates. Then, the creep rates obtained for the materials with various grain sizes can be compared by using the normalized creep rates. Recall that the stress

exponent for polycrystalline alumina with and without silica doping at 1100°C was determined as $1.2 < n < 1.6$ and diffusional creep was identified as the governing creep mechanism. The classical cases of diffusion controlled creep, known as Nabarro-Herring or Coble creep, both contain a theoretical stress exponent $n = 1$. In the case of Nabarro-Herring creep, the steady-state creep rate is controlled by lattice diffusion of vacancies and matter through the grains and has grain size exponent $m = 2$. In the case of Coble creep, the steady-state creep rate is controlled by diffusion of vacancies and matter along the grain boundaries and has a grain size exponent $m = 3$. The creep mechanism most often cited for alumina with grain sizes on the order of 1-15 μm is the Nabarro-Herring creep mechanism [15-17, 164].

The steady-state creep rates obtained for the undoped alumina and for the silica doped alumina in air and in steam, as well as the steady-state creep rates obtained for the Nextel™ 610 fiber tows in air and in steam, have been normalized to a 1 μm grain size by using the applicable creep mechanism. The bulk alumina creep rates were normalized using the Nabarro-Herring creep mechanism with a grain size exponent $m = 2$, whereas the creep rates of Nextel™ 610 were normalized utilizing the interface-reaction controlled creep mechanism with a grain size exponent $m = 1$. The grain sizes used in the normalization were 2.0 μm for the undoped alumina specimens, 4.2 μm for the silica doped alumina specimen, and 0.1 μm for the Nextel™ 610 fiber tows. Normalized creep rates as functions of applied stress are shown in Figure 66. This normalization is carried out by multiplying the measured creep rate by the ratio raised to the grain size exponent of the actual grain size to 1 μm , such that:

$$\dot{\epsilon}_{norm} = \dot{\epsilon}_{actual} \left(\frac{d_{act}}{1 \mu m} \right)^m \quad (32)$$

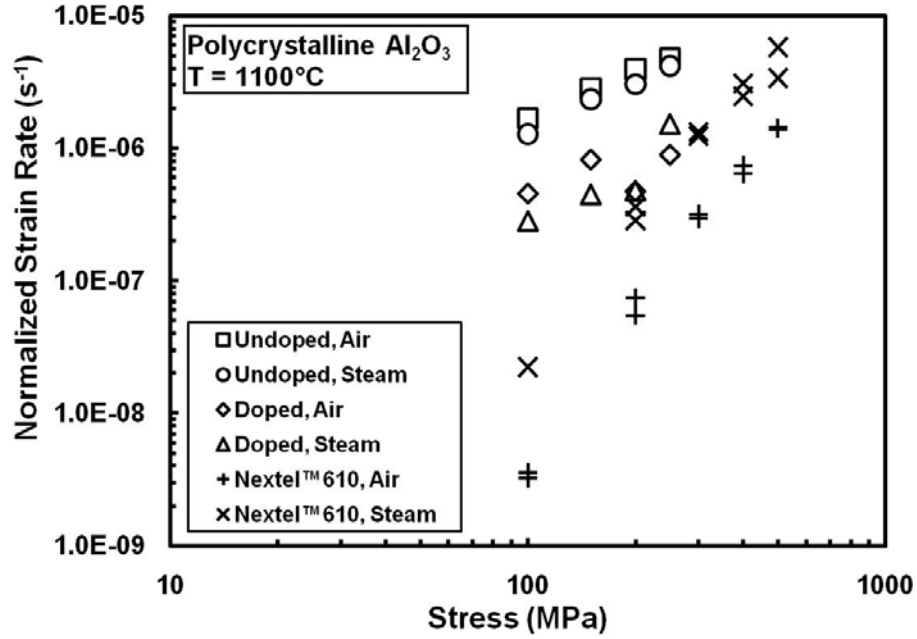


Figure 66. Normalized steady-state creep rates as functions of applied stress for polycrystalline alumina and for the Nextel™ 610 fiber tows at 1100°C in laboratory air and in steam

Results in Figure 66 reveal that the creep rates produced by the silica doped alumina are lower than the creep rates produced by the undoped alumina. The difference is slightly less than one order of magnitude. However, one must keep in mind the previous discussion of the lack of self-similar grain morphology and the fact that abnormal grain growth of the silica doped alumina is likely deviating from the $1/d^2$ relationship of Nabarro-Herring. Nevertheless, if silica doped alumina of self-similar grain morphology indeed exhibited lower rates than undoped alumina, a possible

explanation is that the silica doping is affecting the diffusion of the oxygen anions [57] and/or aluminum cations [15]. The issue of which of these ions is the rate limiting in a polycrystalline alumina is still debated.

Note that the normalized creep rates obtained for the Nextel™ 610 fiber tows are also included in Figure 66. Recall from Section 3.3 that similar creep behaviors have been observed for bulk alumina compared to alumina based fibers, and tension and compression creep comparisons of polycrystalline alumina have been reported with only minor differences. Since Nextel™ 610 fibers contain approximately 0.35 wt% of silica [139, 162], the normalized creep rates obtained for the Nextel™ 610 fiber tows are most comparable with those obtained for the silica doped alumina. However, it was pointed out earlier that significantly different stress exponents obtained for the Nextel™ 610 fiber tows ($2.9 \leq n \leq 3.4$) and for the bulk alumina ($1.2 \leq n \leq 1.6$) indicated that the underlying creep mechanisms for these two materials are also significantly different. Interface-reaction controlled creep is the creep mechanism reported for Nextel™ 610. Whereas, Nabarro Herring creep is likely the creep mechanism responsible for the bulk alumina due to the much larger grain size. This difference in creep mechanism is consistent with the large differences in grain sizes of the fiber and bulk materials.

6.4 Compressive Creep of Polycrystalline Alumina at 1300°C in Laboratory Air

Compressive creep experiments of bulk polycrystalline alumina with and without silica doping were performed at 1300°C in laboratory air. Results of the creep experiments performed on the polycrystalline alumina at 1300°C in laboratory air are

summarized in Table 23. Compressive creep curves obtained at 1300°C in air for alumina and for the silica doped alumina are presented in Figure 67 and Figure 68, respectively. In all tests, specimen failure did not occur when the test was interrupted.

Table 23. Summary of creep results for polycrystalline alumina at 1300°C in laboratory air

Specimen Number / Type	Creep Stress (MPa)	Steady-State Creep Rate (s ⁻¹)
Specimen 1 – undoped	50	8.13x10 ⁻⁷
Specimen 2 – undoped	100	3.08x10 ⁻⁶
Specimen 2 – undoped	150	4.52x10 ⁻⁶
Specimen 2 – undoped	200	5.76x10 ⁻⁶
Specimen 4 – SiO ₂ doped	50	3.43x10 ⁻⁸
Specimen 4 – SiO ₂ doped	100	2.59x10 ⁻⁸
Specimen 4 – SiO ₂ doped	150	3.86x10 ⁻⁸
Specimen 4 – SiO ₂ doped	200	5.91x10 ⁻⁸

Creep tests conducted at 1300°C in air exhibit similar trends and regimes as was reported in Section 6.1 for 1100°C in air. Furthermore, the comparison of creep for the silica doped alumina to the undoped alumina that takes into account the grain size information is presented in Section 6.6.

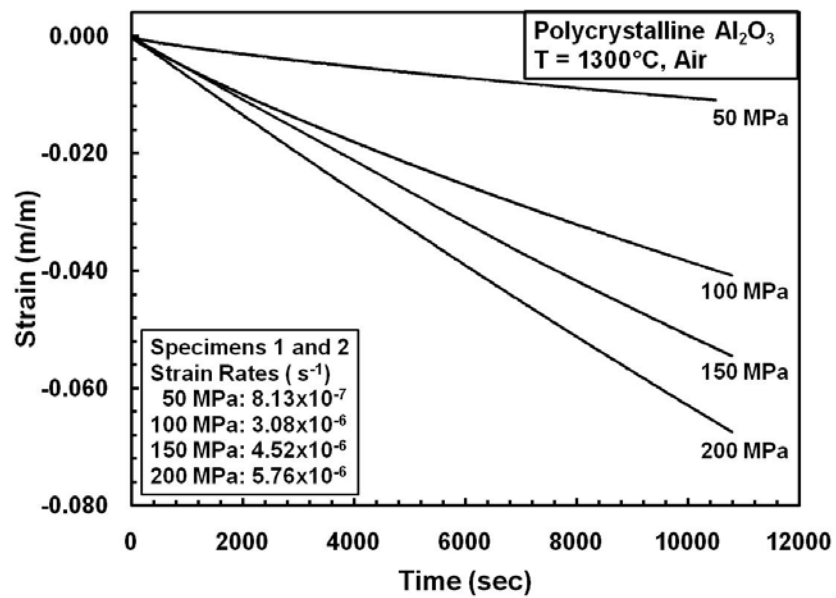


Figure 67. Creep strain vs. time curves for polycrystalline alumina at 1300°C in laboratory air

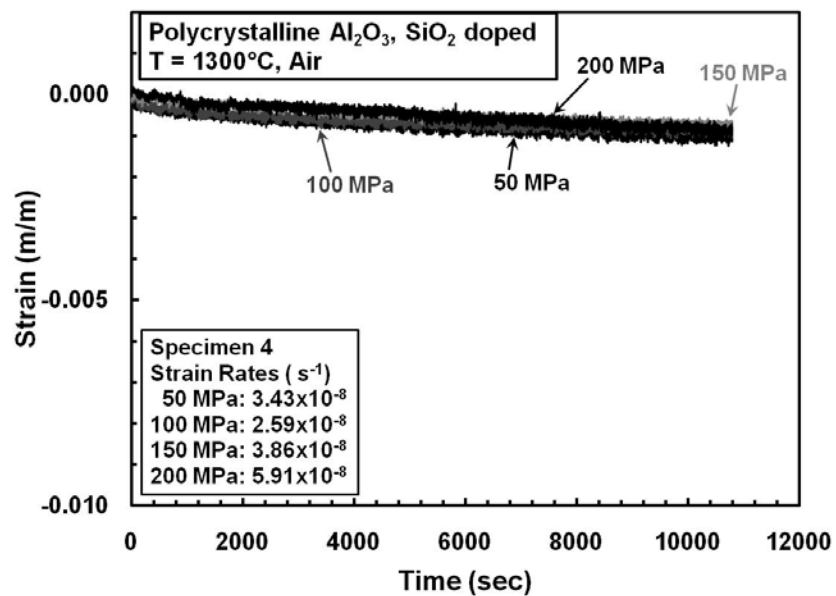


Figure 68. Creep strain vs. time curves for silica doped polycrystalline alumina at 1300°C in laboratory air

6.5 Creep of Polycrystalline Al₂O₃ at 1300°C in Steam

Compressive creep experiments of bulk polycrystalline alumina with and without silica doping were performed at 1300°C in steam. Results of the creep tests performed on the polycrystalline alumina at 1300°C in steam are summarized in Table 24.

Compressive creep curves obtained at 1300°C in steam for alumina and for the silica doped alumina are presented in Figure 69 and Figure 70, respectively. In all tests, specimen failure did not occur when the test was interrupted.

Table 24. Summary of creep results for polycrystalline alumina at 1300°C in steam

Specimen Number / Type	Creep Stress (MPa)	Steady-State Creep Rate (s ⁻¹)
Specimen 3 – undoped	50	9.53x10 ⁻⁷
Specimen 3 – undoped	100	2.43x10 ⁻⁶
Specimen 3 – undoped	150	4.08x10 ⁻⁶
Specimen 3 – undoped	200	6.09x10 ⁻⁶
Specimen 5 – SiO ₂ doped	50	1.55x10 ⁻⁸
Specimen 5 – SiO ₂ doped	100	2.75x10 ⁻⁸
Specimen 5 – SiO ₂ doped	150	3.73x10 ⁻⁸
Specimen 5 – SiO ₂ doped	200	5.98x10 ⁻⁸

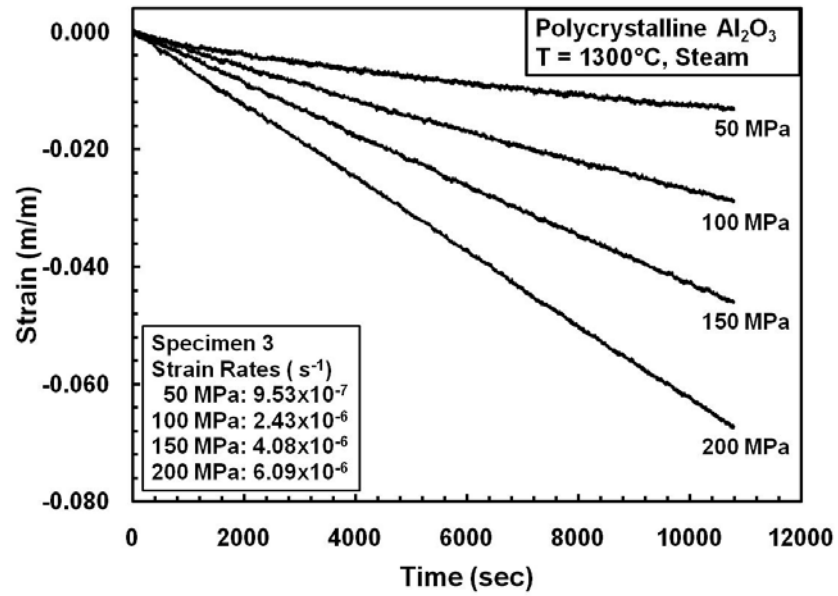


Figure 69. Creep strain vs. time curves for polycrystalline alumina at 1300°C in steam

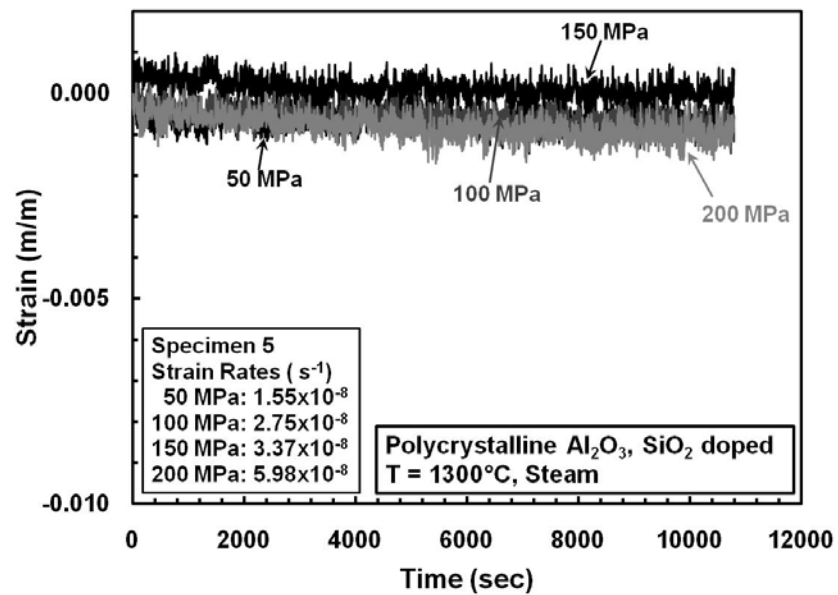


Figure 70. Creep strain vs. time curves for silica doped polycrystalline alumina at 1300°C in steam

Creep tests conducted at 1300°C in steam exhibit similar trends and regimes as was reported in Section 6.4 for 1300°C in air. Likewise, the comparison of creep for the silica doped alumina to the undoped alumina that takes into account the grain size information is presented in Section 6.6. The steady-state (minimum) creep rate was reached in all experiments and dominated the majority of the creep lifetime for all specimens. The steady-state creep rates (prior to grain size correction) as a function of applied stress are presented in Figure 71. Additionally, vacuum-hot-pressed, high-purity alumina data from Cannon et al. [15] with grain size of 1.2 μm is included for comparison.

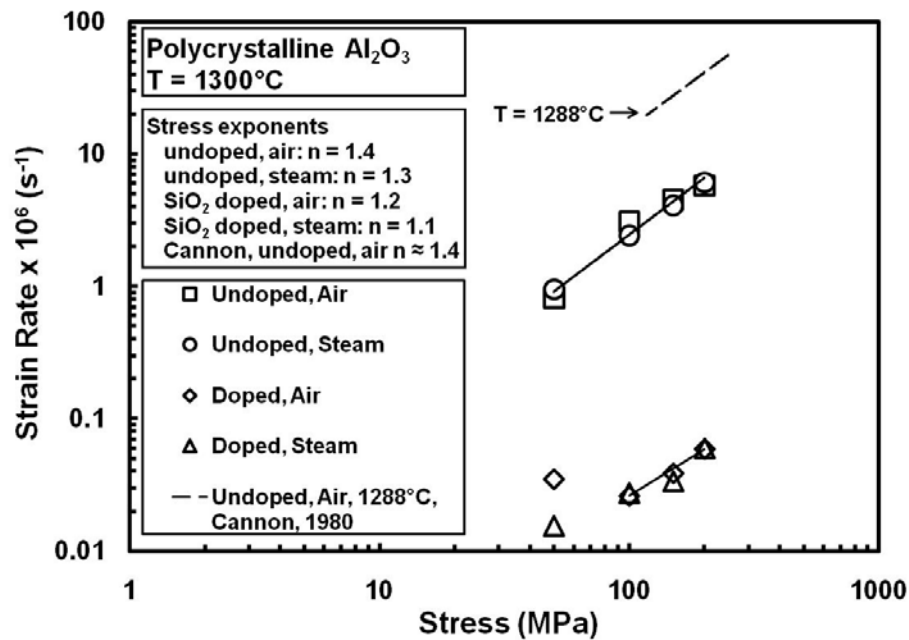


Figure 71. Steady-state creep rate as a function of applied stress for polycrystalline alumina and silica doped polycrystalline alumina at 1300°C in laboratory air and in steam

The most striking result in Figure 71 is that at 1300°C the presence of steam has little influence on creep rates of the polycrystalline alumina with or without silica doping. Results presented in Section 6.3 revealed that at 1100°C the presence of steam also had very little effect on the creep performance of the polycrystalline alumina with or without silica doping.

6.6 Effect of Silica Doping on Compressive Creep Rates of Polycrystalline Alumina at 1300°C in Air and Steam

Recall from Section 6.3 and Equation 31 that the steady-state creep rate is proportional to the applied stress, σ , raised to a stress exponent, n , and inversely proportional to the grain size, d , raised to a grain size exponent, m . Plotting the data in Figure 71 as $\log(\text{strain rate})$ vs. $\log(\text{applied stress})$, the stress exponent, n , was determined by a linear regression analysis for each data set. The stress exponent values for the undoped polycrystalline alumina were 1.4 in air and 1.3 in steam. The stress exponent values for silica doped polycrystalline alumina were 1.2 in air and 1.1 in steam. These values of n are again consistent with those reported in literature [15, 17, 164] and suggest a diffusional creep mechanism.

Also, recall from Section 6.3 the stereologically corrected average grain sizes for the undoped alumina and for the silica doped alumina used in this study were 2.0 μm for the undoped alumina specimens and 4.2 μm for the silica doped alumina specimen. In order to compare the creep rates from specimens with different grain sizes, the creep mechanism must be determined in order to choose the appropriate grain size exponent. Following the same analysis that was performed for polycrystalline alumina at 1100°C in

Section 6.3 and utilizing the Nabarro-Herring creep mechanism, the creep rates obtained for the undoped alumina and for the silica doped alumina at 1300°C in air and in steam were normalized to a 1 μm grain size. The normalized creep rates are shown as functions of applied stress in Figure 72.

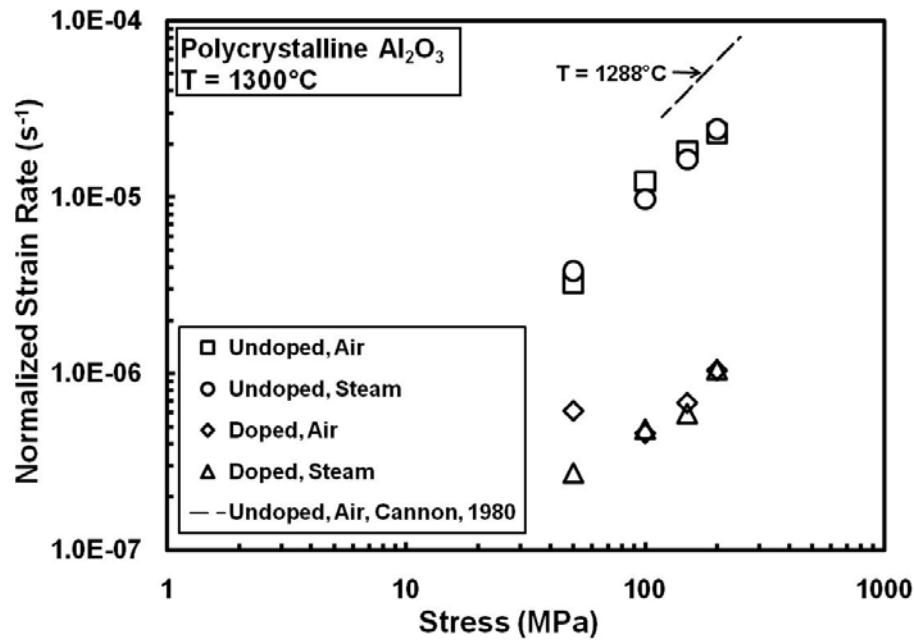


Figure 72. Normalized steady-state creep rate as a function of applied stress for polycrystalline alumina at 1300°C in laboratory air and in steam

Results in Figure 72 reveal that the normalized creep rates of undoped alumina are at least one order of magnitude higher than those of the silica doped alumina. Recall the discussion from Section 6.3 in regard of the lack of self-similar grain morphology and the complicated comparison between the silica doped alumina and undoped alumina. The same discussion applies to the comparison at 1300°C. Additionally, at a creep test temperature of 1300°C additional grain growth is highly probable, especially for the

silica doped specimens. The currently available analysis of the optical micrographs did not indicate a large difference in the post-test grain size compared with the pre-test grain size. However, it is recommended that additional TEM study of the 1300°C alumina specimens be conducted. Additional grain growth would further exacerbate the problem in comparing the rates of the silica doped alumina to the undoped alumina. (Note: additional grain growth during the 1300°C creep tests, especially in the silica doped alumina, may help explain the troubling calculation of the creep activation energies included in the Appendix.)

6.7 Summary of the Effects of Steam on the Creep Behavior of Polycrystalline Alumina at 1100 and 1200°C

In this chapter, the creep performance of bulk polycrystalline alumina with grain sizes ranging from 2.0 to 4.2 μm was not affected by the presence of steam. Based on the grain size and the stress exponents, the dominant creep mechanism was determined to be the Nabarro-Herring creep mechanism. While the effects of steam were detrimental to the interface-reaction controlled creep mechanism of the alumina based fiber tows, the effects of steam did not affect the Nabarro-Herring creep mechanism.

Additionally, an endeavor to determine the effects of silica doping on the creep rates of alumina were attempted. The results of the normalization of creep rates by the grain size utilizing the Nabarro-Herring creep mechanism demonstrated that the presence of silica retards the creep rates. However, the lack of self-similar grain morphologies of the silica doped alumina compared to the undoped alumina complicated this comparison.

The silica doped alumina contained large platelet grains as a result of abnormal grain growth, which likely cause it to deviate from the Nabarro-Herring grain size dependency.

Finally, additional grain growth in the alumina specimens, especially the silica doped specimens, is highly suspected for the 1300°C creep tests. Additional grain growth would further underestimate the creep rates. Since silica doping enhances grain growth of alumina, it is suspected that the grains of the doped specimens may have grown disproportionately compared to the undoped alumina. It is recommended that further TEM analyses be conducted on these specimens.

VII. Creep Behavior of Polycrystalline Yttrium Aluminum Garnet at 1300°C

This chapter describes the compressive creep performance of bulk polycrystalline yttrium aluminum garnet (YAG, $\text{Y}_3\text{Al}_5\text{O}_{12}$) in air and in steam environment at 1300°C. In addition to evaluating the effects of steam on creep behavior of high-purity polycrystalline YAG at 1300°C, the influence of silica (SiO_2) doping on creep performance was also examined. The results obtained for the polycrystalline YAG are compared to those obtained for the polycrystalline alumina from Chapter 6. Finally, based on the results of this research the feasibility of the development of YAG fibers is discussed.

Compressive creep experiments of bulk YAG were successfully completed at 1300°C in both laboratory air and steam environments. Details of the YAG compression specimens are provided in Section 3.1. The facility used to test the bulk YAG specimens is described in Section 3.3.

7.1 Compressive Creep of Polycrystalline Yttrium Aluminum Garnet at 1300°C in Laboratory Air

Compressive creep experiments of bulk polycrystalline YAG with and without silica doping were performed at 1300°C in laboratory air. Results of the creep experiments performed on the polycrystalline YAG at 1300°C in laboratory air are summarized in Table 25. Compressive creep curves obtained at 1300°C in air for YAG and for the silica doped YAG are presented in Figure 73 and Figure 74, respectively. In all tests, specimen failure did not occur when the test was interrupted.

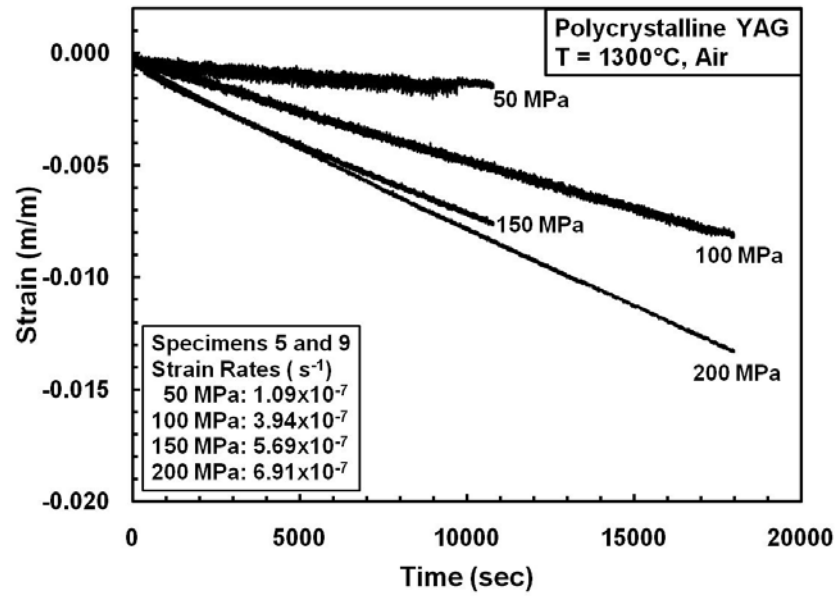


Figure 73. Creep strain vs. time curves for polycrystalline YAG at 1300°C in laboratory air

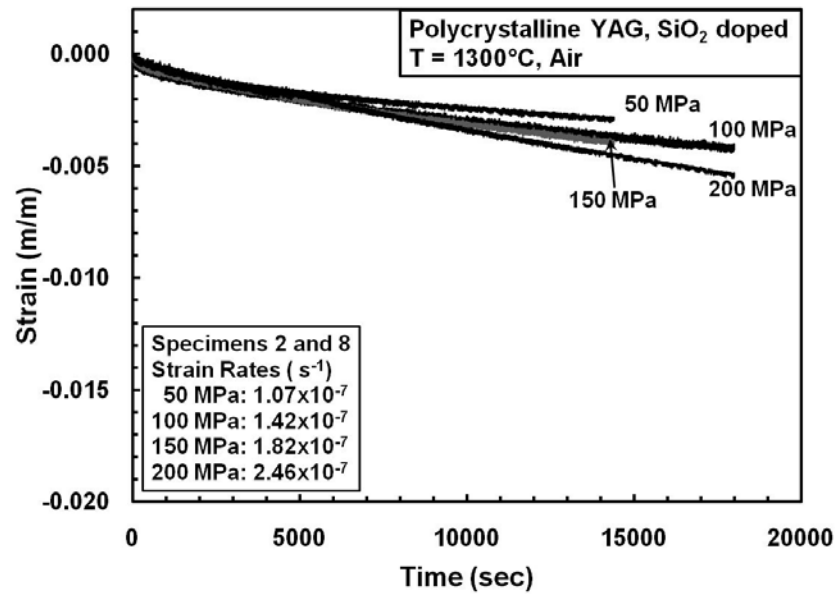


Figure 74. Creep strain vs. time curves for silica doped polycrystalline YAG at 1300°C in laboratory air

Table 25. Summary of creep results for polycrystalline YAG at 1300°C in laboratory air

Specimen Number / Type	Creep Stress (MPa)	Steady-State Creep Rate (s^{-1})
Specimen 9 – undoped	50	1.09×10^{-7}
Specimen 5 – undoped	100	3.94×10^{-7}
Specimen 9 – undoped	150	5.69×10^{-7}
Specimen 5 – undoped	200	6.91×10^{-7}
Specimen 8 – SiO ₂ doped	50	1.29×10^{-7}
Specimen 2 – SiO ₂ doped	100	5.29×10^{-7}
Specimen 8 – SiO ₂ doped	150	7.31×10^{-7}
Specimen 2 – SiO ₂ doped	200	9.46×10^{-7}

Creep curves produced in all tests conducted at 1300°C in air exhibit primary and secondary creep regimes. Transition from primary to secondary creep occurred early in the creep life. As expected, the steady-state creep rates increased with increasing creep stress magnitudes. The accumulated creep strain and strain rates obtained for silica doped YAG specimens were considerably lower than those obtained for the undoped YAG specimens. However, it should be noted that the average grain size of the polycrystalline YAG are different from that of the silica doped polycrystalline YAG. The grain sizes of the two materials are evaluated, and a comparative analysis of the compressive creep rates that takes into account the different grain sizes is discussed in detail in Section 7.3.

7.2 Compressive Creep of Polycrystalline Yttrium Aluminum Garnet at 1300°C in Steam

Compressive creep experiments of bulk polycrystalline YAG with and without silica doping were also performed at 1300°C in steam. Results of the creep experiments performed on the polycrystalline YAG at 1300°C in steam are summarized in Table 26. Compressive creep curves obtained at 1300°C in steam for YAG and for the silica doped YAG are presented in Figure 75 and Figure 76, respectively. In all tests, specimen failure did not occur when the test was interrupted.

Table 26. Summary of creep results for polycrystalline YAG at 1300°C in steam

Specimen Number / Type	Creep Stress (MPa)	Steady-State Creep Rate (s^{-1})
Specimen 7 – undoped	50	1.29×10^{-7}
Specimen 3 – undoped	100	5.29×10^{-7}
Specimen 7 – undoped	150	7.31×10^{-7}
Specimen 3 – undoped	200	9.46×10^{-7}
Specimen 10 – SiO ₂ doped	50	8.25×10^{-8}
Specimen 1 – SiO ₂ doped	100	1.39×10^{-7}
Specimen 10 – SiO ₂ doped	150	1.42×10^{-7}
Specimen 1 – SiO ₂ doped	200	2.46×10^{-7}

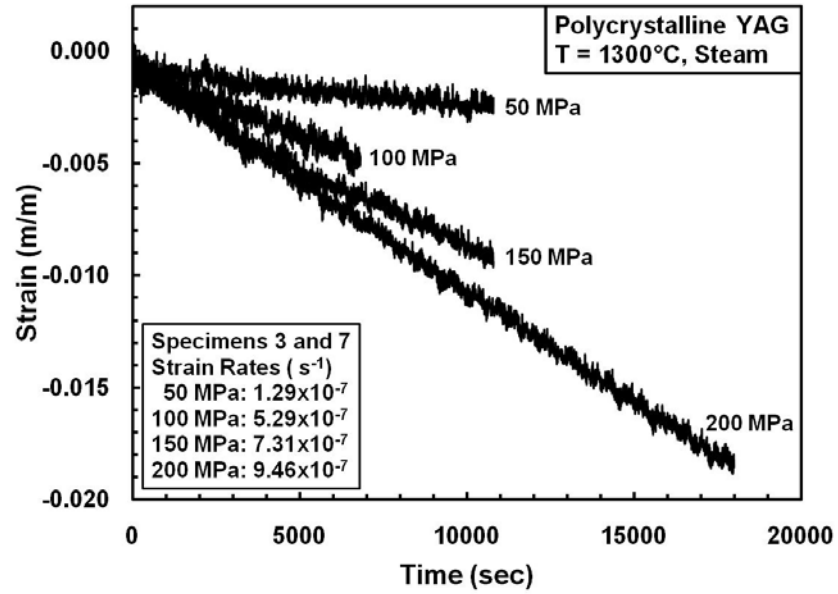


Figure 75. Creep strain vs. time curves for polycrystalline YAG at 1300°C in steam

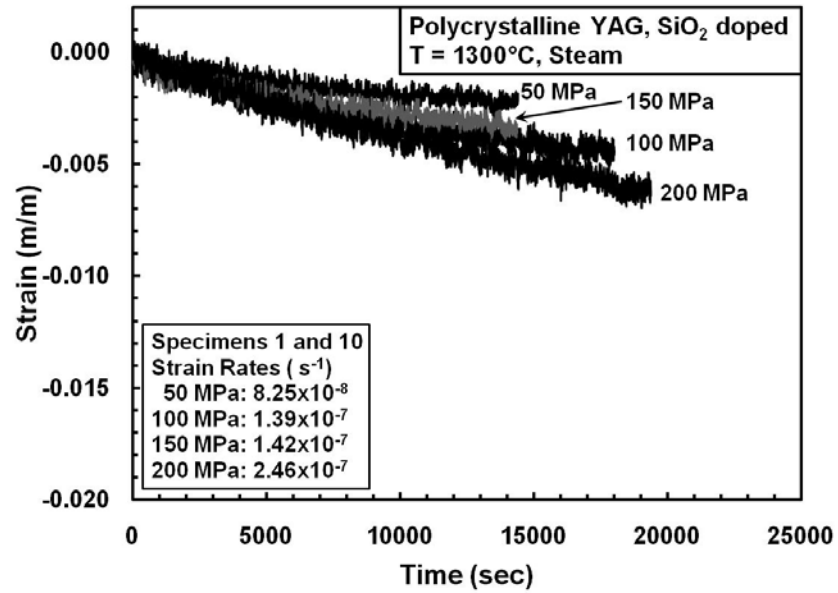


Figure 76. Creep strain vs. time curves for silica doped polycrystalline YAG at 1300°C in steam

It is seen that at 1300°C the accumulated creep strains produced by YAG specimens in steam are slightly larger than those produced in air at a given creep stress. However, the creep rates produced in steam are very close to those produced in air at a given creep stress. Apparently the presence of steam has little or no effect on compressive creep of YAG or on the compressive creep of silica doped YAG at 1300°C. The comparison of creep for the silica doped YAG to the undoped YAG that takes into account the grain size differences is presented in Section 7.3.

7.3 Effect of Silica Doping on Compressive Creep Rates of Polycrystalline YAG at 1300°C in Air and Steam

Results of creep tests obtained for the undoped polycrystalline YAG and for the silica doped polycrystalline YAG at 1300°C in air and in steam are presented in Sections 7.1 and 7.2, respectively. The steady-state (minimum) creep rate was reached in all experiments and dominated the majority of the creep lifetime for all specimens. The steady-state creep rate as a function of applied stress is presented in Figure 77, where the high-temperature creep formulation of fine-grained polycrystalline YAG obtained by Parthasarathy, et al. [115] applied at 1300°C are included for comparison. Note that Parthasarathy's formulation for creep behavior of YAG was determined from data obtained at 1400-1610°C in vacuum with an average grain size of approximately 3 μm . The effects of steam on the creep rates of either the silica doped or undoped polycrystalline YAG at 1300°C was negligible.

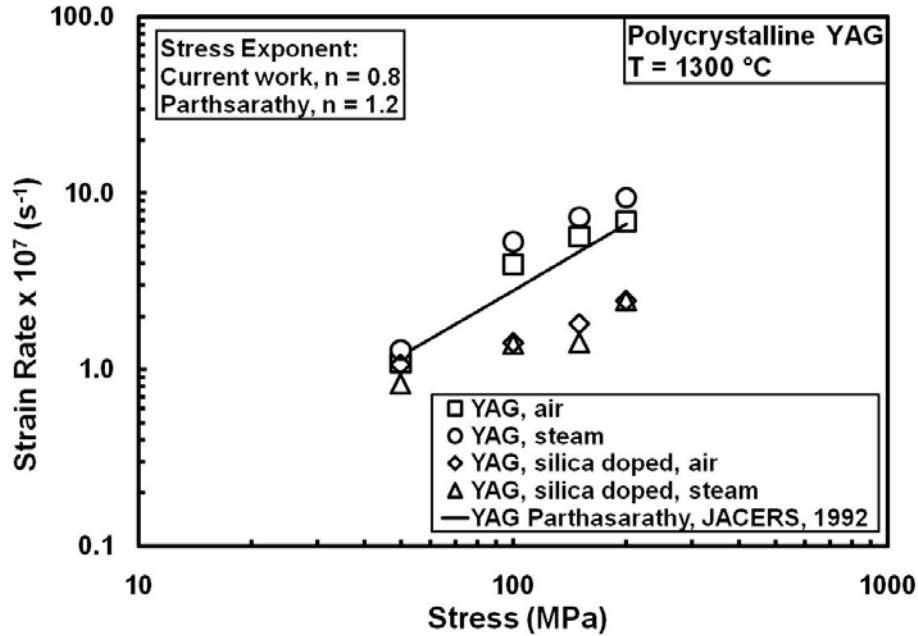


Figure 77. Steady-state creep rate as a function of applied stress for polycrystalline YAG and for silica doped polycrystalline YAG at 1300°C in laboratory air and in steam

Recall from Section 6.3 and also from Equation 1 that the steady-state creep rate is proportional to the applied stress, σ , raised to a stress exponent, n , and inversely proportional to the grain size, d , raised to a grain size exponent, m . Plotting the data in Figure 77 as log (strain rate) vs. log (applied stress), the stress exponent, n , was determined by a linear regression analysis for each data set. The stress exponent was 0.8 for all data sets obtained in the present study. Parthasarathy, et al. [115] measured a stress exponent of 1.24 and demonstrated that creep of the polycrystalline YAG obeyed the Nabarro-Herring diffusion model. Recall that the Nabarro-Herring creep mechanism, in theory, is characterized by a stress exponent $n = 1$ and grain sizes exponent of $m = 2$ as previously discussed in Section 2.4.

The grain sizes of the two YAG materials used in this study were measured before and after creep testing using both optical and transmission electron microscopy (TEM) at the Air Force Research Laboratory, Materials and Manufacturing Directorate. Typical optical micrographs of the silica doped polycrystalline YAG and of the polycrystalline YAG are shown in Figure 78 (a) and (b), respectively. Similarly, the TEM micrographs of the silica doped polycrystalline YAG and of the polycrystalline YAG are shown in Figure 79 (a) and (b), respectively.

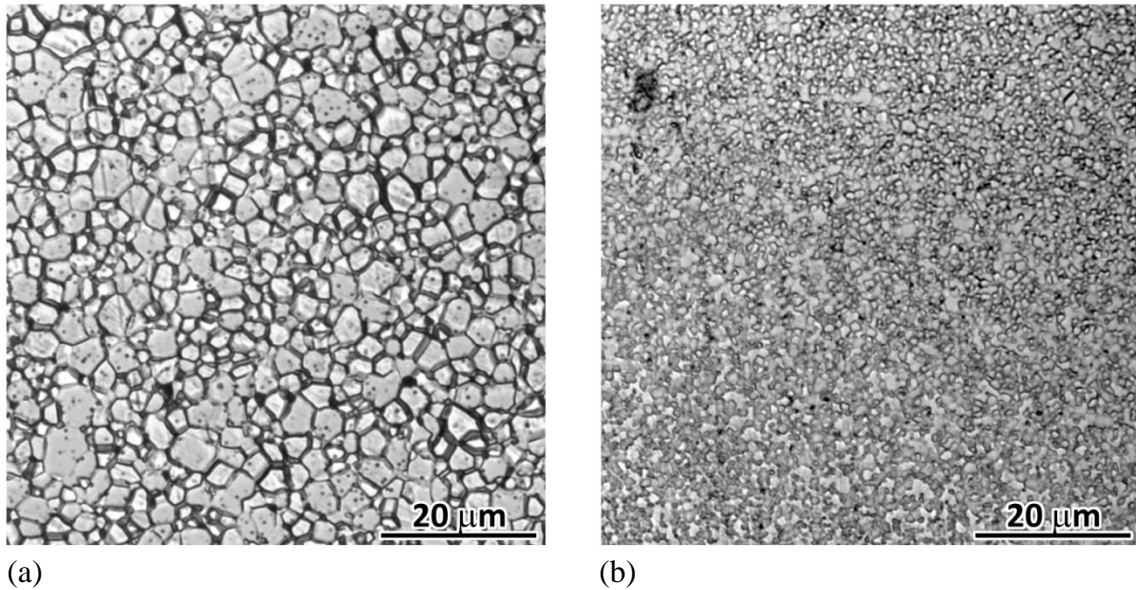


Figure 78. Optical micrographs showing the grain structure of: (a) silica doped polycrystalline YAG and (b) polycrystalline YAG.

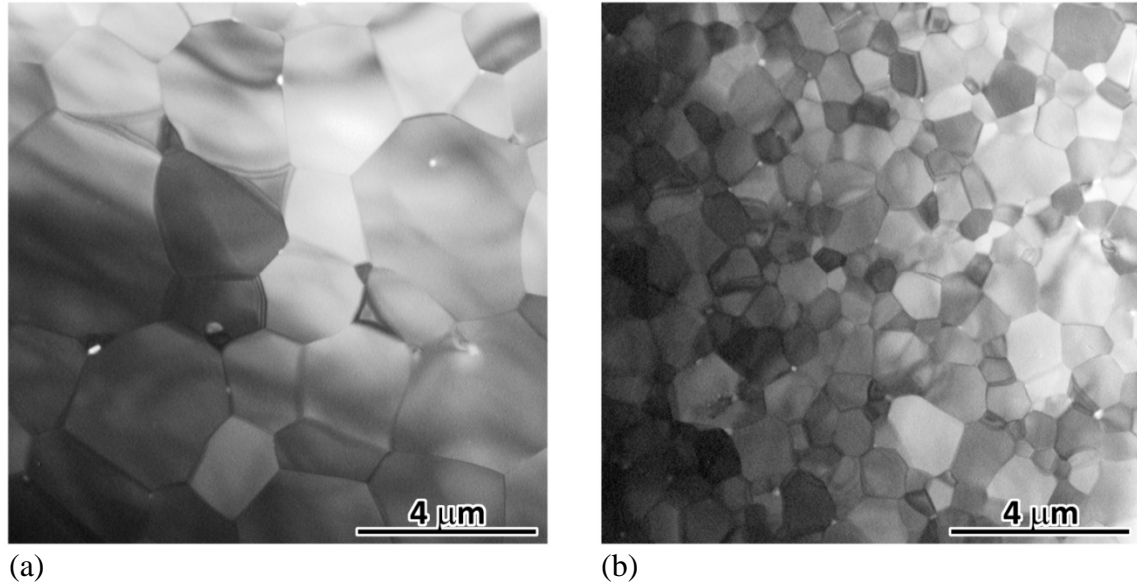


Figure 79. TEM micrographs showing the grain structure of: (a) silica doped polycrystalline YAG and (b) polycrystalline YAG

The grain size distribution analyses were performed and the grain sizes of the polycrystalline YAG and of the silica doped polycrystalline YAG were determined using a log-normal distribution of the grain sizes obtained from the TEM micrographs. Notably there were no substantial differences in the grain size of the materials analyzed before and after creep testing. The log-normal average grain size and standard deviations were $0.32 \pm 0.20 \log \mu\text{m}$ for the silica doped YAG and $-0.1 \pm 0.18 \log \mu\text{m}$ for the undoped YAG. These log-normal average grain sizes equate to the grain sizes of 2.09 μm and 0.79 μm for the silica doped and undoped YAG, respectively. Using the same stereological correction as in Section 6.3, the corrected grain size measurements resulted in average grain sizes of 2.41 μm for the silica doped YAG specimens and 0.92 μm for the undoped YAG specimens. The stereologically corrected grain sizes were used to analyze the creep rates obtained for the undoped and the silica doped specimens and to

evaluate the effect of silica doping on the compressive creep performance of polycrystalline YAG at 1300°C in air and in steam. Note that the average grain size of the material studied by Parthasarathy et al. [115] was approximately 3 μm .

In order to compare the creep rates obtained for specimens with different grain sizes, the creep mechanism must be identified and utilized. Identifying the creep mechanism with the appropriate grain size exponent will allow creep rates to be normalized to a specific grain size. Earlier in this section, the stress exponent for the polycrystalline YAG at 1300°C was calculated as 0.8 and the Nabarro-Herring diffusional creep is believed to be the dominant creep mechanism based on the stress exponent and the grain size. Using the Nabarro-Herring creep mechanism, the steady-state creep rates produced by both undoped YAG and silica doped YAG in air and in steam, as well as the steady-state creep rate formulation by Parthasarathy et al. [115] have been normalized to a 1 μm grain size in Figure 80. This normalization process was described earlier in Section 6.3 and is the same process used here.

Once the creep rates produced by the materials with various grain sizes are normalized, the normalized steady-state creep rates can be compared to reveal the effect of silica doping. Results in Figure 80 demonstrate that the creep rates of the silica doped YAG are slightly higher than the creep rates of the undoped YAG at 1300°C in air or in steam environment. This observation is opposite of the preliminary results formed based on the data in Figure 77 where the different grain sizes were not taken into account. However, this weak effect of silica doping on the creep rates is fairly small and could possibly be negligible.

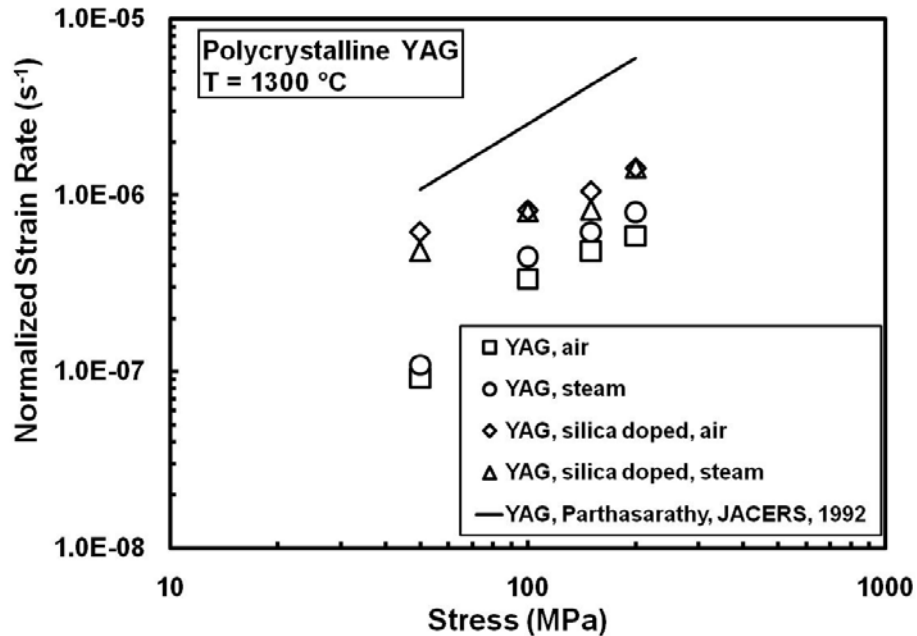


Figure 80. Normalized steady-state creep rate as a function of applied stress for fine-grained polycrystalline YAG at 1300°C in laboratory air and in steam

Intrinsically, creep of polycrystalline YAG of this grain size is dominated by lattice diffusion (the Nabarro Herring creep mechanism). Furthermore, the rate-limiting (that is, the slowest moving) species in the lattice of YAG has been reported to be the yttrium cation (Y^{3+}) [64]. Additionally, the presence of silica doping in YAG with sufficient temperature results in Si^{4+} cation in solution with YAG [144]. Stevenson et al. observed that increasing silica content increased both densification and grain growth rates, and silica content up to 0.28 wt.% forms a complete solid solution with YAG at processing temperatures between 1600 and 1750°C. The YAG specimens studied in the current work were processed near these conditions (HIP at 1500-1600°C/5-10 hours under 30 ksi argon pressure with 0.14 wt.% silica). As observed in Figure 78 and Figure 79, the effect of silica doping corresponds to the larger grain size. Therefore, the effect

of silica doping in YAG may have an increasing effect on the diffusivity of yttrium resulting in increased lattice diffusion. As a result, the slightly increased creep rates of silica doped YAG demonstrated by the normalized rates in Figure 80 are likely consistent with the recent findings by Stevenson et al.

Another important insight to be gained from the results in Figure 80 is that the steam environment has very little effect on the creep performance of either the undoped or the silica doped polycrystalline YAG at 1300°C. This conclusion is similar to that reached for the polycrystalline alumina in Chapter 6 and is attributed to a lack of environmental effect of steam on Nabarro-Herring creep.

7.4 Summary and Assessment of the Feasibility of YAG Fiber Development

In considering the possibility of developing a commercially available YAG fiber, there are many complex issues that must be addressed, like processing, mechanical performance, and manufacturing. The focus of this research has been on the mechanical performance of polycrystalline YAG at 1300°C in air and in steam environments. Therefore, processing and manufacturing issues are not addressed here. Rather, the current emphasis is on the mechanical performance and environmental durability of polycrystalline YAG as a candidate oxide fiber material for use in next-generation, high-temperature CMCs.

YAG is believed to be one of the most creep resistant oxide material [29]. Multiple studies have demonstrated that YAG has a comparative advantage in creep over other oxide fibers [67, 102, 163]. This attractive property has created much interest from the structural ceramics community.

For polycrystalline fibers, the fracture strength is dependent upon the grain size and fiber density. In order to maximize fracture strength, the grain size must be reduced and the density must be increased. However, as previously described, the steady-state creep rate is inversely proportional to the grain size raised to the grain size exponent. Therefore, as the grain size is reduced to improve strength, the creep rates increase and potentially at an even faster rate if the dominant creep mechanism changes. This physical property tradeoff is unfortunate. However, since oxide ceramic fibers have demonstrated a particular weakness in creep for most practical applications, the creep resistance exhibited by YAG makes it a promising candidate for the next generation polycrystalline ceramic oxide fiber material. Moreover, YAG also has a cubic lattice structure, which results in low residual stresses due to temperature changes (no thermal expansion anisotropy). Additionally, two studies discussed in Section 2.6, by Klemm, et al. [72] and Fritsch, et al. [44], found the corrosion resistance of YAG superior to that exhibited by alumina or mullite. All of these attributes are beneficial properties that make YAG a desirable candidate for a future oxide fiber material.

Many aerospace applications must operate in a steam-rich environment and the effect of steam on mechanical performance is important. Previous results obtained for oxide-oxide CMCs have shown surprising degradation of the creep performance at high temperatures in a steam environment. This result was surprising since oxide ceramics are considered to be inert to an oxidizing environment. However, the thermochemical stability of oxide materials does not necessarily hold at extreme operational temperatures in a steam environment under load.

In this study, the creep rates of a high-purity, fine grain polycrystalline YAG material were measured at 1300°C in air and in steam environments. The presence of steam did not affect the compressive creep performance at 1300°C of polycrystalline YAG with or without silica doping. This is an encouraging result. However, similar results were demonstrated for polycrystalline alumina in compression in Chapter 6. Yet, the alumina based fiber Nextel™ 610 (Chapter 4), as well as Nextel™ 720 (Chapter 5), were shown to have degraded creep performance in steam. This difference in the alumina based materials is believed to be the result of different underlying creep mechanisms based upon grain size. Recall, the bulk alumina had average grain sizes of 2.0 μm for the undoped specimens and 4.2 μm for the silica doped specimens. At this grain size, creep of polycrystalline alumina is controlled by Nabarro-Herring creep, and thus the steam did not affect the creep rates. Likewise, the polycrystalline YAG had grain size of 0.92 μm for the undoped YAG and 2.41 μm for the silica doped YAG. In contrast, the grain size of the Nextel™ 610 fiber is on the order of 100 nm, and the corresponding creep mechanism is that of interface-reaction controlled creep, which is affected by the presence of steam. Considering this in light of the feasibility of YAG as a future fiber material, the effect of grain size on the strength of YAG needs to be determined. If the grain size of YAG has to be reduced to the point that Coble creep or interface-reaction controlled creep dominate, then the creep rates may become susceptible to the steam environment. This remains to be determined. However, evidence exists that YAG may be able to tolerate a much larger grain size with sufficient strength for composite applications. In the previously mentioned study by Morscher [102], the experimental

fiber contained a grain size of approximately 1 μm and showed superior creep performance in a bend stress relaxation test to other available fibers.

Furthermore, if the underlying creep mechanism for a useful YAG fiber is Nabarro-Herring creep, then the creep rate is less sensitive to grain size than if it were dominated by Coble creep ($1/d^2$ instead of $1/d^3$, respectively). More importantly, if the creep mechanism for a useful YAG fiber is either of the two classical diffusion mechanisms, then the creep rate dependency on applied stress is much less sensitive (σ^1) than the currently available oxide fibers that are interface-reaction controlled (σ^3).

Results from the present study also showed a very small but slightly increasing effect of silica doping on creep rates. This may be explained by increased diffusivity due to the silicon cation in solid solution with YAG. The recent findings [144] of increased grain growth and densification with increasing silica content in polycrystalline YAG are perhaps consistent with the slight increase in creep rates in the present study due to increased mass transport effects with increased silica doping.

Further experimental investigation should focus on exploring the dependency of strength on grain size with and without silica in air and in steam. Concurrently, the creep performance as a function of grain size needs to be assessed in order to determine when the creep mechanism transitions and whether the creep mechanisms are affected by steam. Additionally, the creep performance and strength of polycrystalline YAG at temperatures exceeding 1300°C in air and in steam also needs to be explored. With its superior mechanical properties at high temperatures compared to currently available oxide fibers, YAG is potentially the ideal oxide fiber for the next-generation, high temperature composites.

VIII. Conclusions and Recommendations

8.1 Conclusions

The effects of steam on the high-temperature mechanical performance of oxide ceramic fiber materials were investigated. Monotonic tension and creep performance of Nextel™ 610 and Nextel™ 720 fiber tows at elevated temperatures in air and in steam were evaluated. In addition, compressive creep behavior of two bulk ceramic materials, namely high-purity polycrystalline yttrium aluminum garnet (YAG, $\text{Y}_3\text{Al}_5\text{O}_{12}$) and polycrystalline alumina (Al_2O_3), were studied at elevated temperatures in air and in steam.

For the Nextel™ 610 fiber tows, experimental results revealed a stress rate dependence on ultimate tensile strength at 1100°C in steam environment. Subcritical crack growth parameters were calculated from these experimental results, and a linear elastic crack growth model was used to predict the creep lifetimes from the constant stress rate test data at 1100°C in steam. Excellent agreement between predicted creep lifetimes and experimental results demonstrates that environmentally assisted subcritical crack growth is the governing failure mechanism for the Nextel™ 610 fiber tows at 1100°C in steam. Results for the Nextel™ 720 fiber tows were less conclusive but subcritical crack growth is likely a major contributor to its failure in steam. Further investigation, such as TEM, is required to gain further insight into the damage and failure mechanisms of Nextel™ 720 fiber tows.

Creep results revealed that the presence of steam had a degrading effect on the creep lifetimes and steady-state creep rates of Nextel™ 610 and Nextel™ 720 fiber tows at

elevated temperatures. At 1100°C in the presence of steam, the creep rates of the Nextel™610 fiber tows increased by one order of magnitude, while the creep lifetimes decreased by one order of magnitude. The stress exponent was determined as $n \approx 3$, indicating interface-reaction controlled creep mechanism as the responsible creep mechanism. It was demonstrated that the Monkman-Grant relationship could be employed to predict creep-rupture for the Nextel™610 fiber tows at 1100°C in air and in steam and that Monkman-Grant constants were independent of the test environment.

Creep behavior of the Nextel™720 fiber tows at 1200°C was also influenced by the presence of steam. In a lower stress region (≤ 300 MPa) at 1200°C in steam, the creep rates of Nextel™720 fiber tows increased by one order of magnitude and the creep lifetimes decreased one order of magnitude. In the lower stress region, the stress exponent was determined as $n \approx 3$, indicating interface-reaction controlled creep mechanism as the responsible creep mechanism. However, the creep behavior of Nextel™720 changed dramatically above 300 MPa. In the high stress region (> 300 MPa) at 1200°C, the steady-state creep rate becomes independent of the test environment, producing similar creep rates and similar creep lifetimes in air and in steam. This shift in behavior is due to a shift in the underlying creep mechanism from the interface-reaction controlled creep (characterized by a stress exponent $n \approx 3$) in the low stress region, to one of dislocation creep of possibly void growth (characterized by a stress exponent $n = 5$) in the high stress region. Nevertheless, the Monkman-Grant relationship could be utilized to predict creep-rupture of the Nextel™720 fiber tows at 1200°C in air and in steam regardless of the creep stress level. Additionally, the Monkman-Grant constants were found to be independent of the test environment.

The effects of steam on the creep performance of high-purity polycrystalline alumina were evaluated at 1100 and 1300°C. The presence of steam had no effect on the compressive creep rates of polycrystalline alumina with 2.0 μm grain size or of the silica doped alumina with 4.2 μm grain size at 1100 and 1300°C. The effects of silica doping on the creep rates was difficult to determine. As it appears, the silica doped alumina had lower creep rates than the undoped silica. However, abnormal grain growth of the doped silica specimens creates a lack of self-similar grain morphology for the comparison of the results of silica doped alumina compared to the undoped alumina. Based on the stress exponent of $n \approx 1$ and in accordance to alumina with similar grain sizes, the dominant creep mechanism for the polycrystalline alumina was Nabarro-Herring creep. Thus, the Nabarro-Herring creep mechanism proved to be unaffected by the steam environment. Additionally, further abnormal grain growth was suspected for the creep tests of alumina at 1300°C, especially in the silica doped specimens.

The effects of steam on the creep performance of high-purity polycrystalline YAG were also evaluated at 1300°C. Polycrystalline YAG exhibited superior compressive creep performance at 1300°C in air and in steam. The presence of steam had little effect on compressive creep rates of polycrystalline YAG or of the silica doped YAG at 1300°C. Additionally, the grain morphology between the silica doped YAG and the undoped YAG were self-similar with equiaxial shaped grains. The effect of silica doping increased the grain growth. However, silica doping slightly accelerated compressive creep of polycrystalline YAG at 1300°C. This extrinsic effect on the creep of YAG may be due to increased diffusion due to the presence of silicon cations in solution within the YAG lattice, which could increase diffusion through the lattice

structure. The Nabarro-Herring creep mechanism is believed to be the dominant creep mechanism for polycrystalline YAG with grain sizes on the order of 1-3 μm . Therefore, the Nabarro-Herring creep mechanism was unchanged by the presence of steam. The superior high temperature creep performance and invariant creep behavior in the presence of high temperature steam of polycrystalline YAG are advantageous properties for considering YAG as the next-generation, oxide ceramic fiber material.

8.2 Contributions

The present research represents the first experimental investigation of the effects of steam on creep behavior of ceramic fibers at elevated temperature. Additionally, this was the first study that involved testing of fiber tows performed in AFIT laboratories. Therefore, considerable effort went into designing and validating the experimental apparatuses and developing the experimental methods.

The effects of steam on mechanical performance and behavior of oxide-oxide CMCs at elevated temperatures had been previously reported. Subcritical crack growth of the fiber constituent was suspected. This research demonstrated that environmentally assisted subcritical crack growth is indeed the dominant failure mechanism operating in NextelTM 610 in steam environment at high temperatures.

Furthermore, the effects of steam on the creep performance of current oxide fibers had not been previously quantified independent of composite systems. The steady-state creep rates increased by one order of magnitude in steam while the creep lifetimes decreased by one order of magnitude in steam for NextelTM 610 at 1100°C and for NextelTM 720 at 1200°C and stresses ≤ 300 MPa. However, the shift in creep behavior and

change in underlying creep mechanism of Nextel™ 720 fibers above 300 MPa at 1200°C has not been previously reported. This result is important in order to prevent an unanticipated early creep limit or catastrophic failure for applications designed to operate near the high stress, high temperature region for this fiber.

Very few studies have explored the mechanical behavior of polycrystalline YAG at high temperatures. This is the first known study to investigate the creep performance of polycrystalline YAG at high temperatures in a steam environment. Additionally, this was the first study to investigate the effects of silica doping on the compressive creep performance of fine-grained polycrystalline ceramic materials (alumina and YAG) at high temperatures in air and in steam environments. Considerable effort went into designing and validating an experimental facility and into developing the experimental methods for compression creep testing of the bulk polycrystalline alumina and polycrystalline YAG specimens at high temperatures in steam environment. The creep performance of YAG at the reported grain size proved to be unaffected by the steam environment. The results of this effort advanced the rationale for further developmental work toward the production of a polycrystalline YAG fiber for application in advanced aerospace structures.

8.3 Recommendations for Future Work

Future ceramic fiber development programs should seek early environmental testing of the candidate materials at high temperatures under operationally relevant load conditions before investing substantial funds in the fiber development. Obtaining such

results prior to full rate production could help allocate the extensive capital investments required for commercial ceramic fiber processing.

One area of active research in the area of CMCs is fiber coatings that provide oxidation and corrosion resistance to ceramic fibers. The effectiveness of these coatings for fiber protection in steam at high temperatures could be evaluated by testing coated fiber tows prior to more complex testing of CMCs. This would provide helpful feedback into the design and processing of fiber coatings without the added complexity of creating a composite system.

For polycrystalline alumina, further TEM work is warranted to better characterize the grain size distribution and the grain morphology. It is suspected that the creep testing at 1300°C induced additional grain growth, in particular for the silica doped alumina specimens. Additionally, further work could be performed by way of attempts to process silica doped polycrystalline alumina with self-similar grain morphologies. A few suggestions to achieve self-similar morphology are: lower sintering temperature ($\leq 1300^{\circ}\text{C}$), reduced doping level or ultrapure processing, and codoping or alternative sintering agents, such as MgO.

The superior mechanical properties and environmental resistance of polycrystalline YAG at high temperatures makes it the top candidate material for the next-generation structural oxide fiber material. Nonetheless, tensile creep testing of polycrystalline YAG at high temperatures in a steam environment is necessary to ensure environmental resistance. This would confirm whether polycrystalline YAG is resistant to environmental effects under operationally representative conditions. Furthermore, YAG has the potential to successfully operate at temperatures $>1400^{\circ}\text{C}$. Therefore,

testing at temperatures above 1300°C is warranted. Testing at various temperatures would also aid in further characterization such as determining the creep activation energy.

Additionally, the effect of different grain sizes on the creep performance and on strength of YAG is necessary. The effect of grain size on strength should be determined. If larger grain sizes than what is required for an alumina based fiber are acceptable for adequate strength, then potential creep problems may be alleviated by maintaining the fiber in the Nabarro Herring creep regime and avoiding either Coble or interface-reaction controlled creep regimes. Simultaneously, more creep experiments in air and in steam with and without SiO₂ are essential to determining what grain size the creep mechanism transitions. These two pieces of information about grain size and strength will aid in designing an optimal YAG fiber.

Furthermore, a less dense batch of YAG could also be considered as a matrix material for CMCs. CMCs utilizing currently available fibers may perhaps be processed with a YAG matrix material and mechanically tested in steam. In this scenario, the creep performance of the CMC may be substantially improved by utilizing a matrix that has improved creep resistance over current matrix materials

Appendix

Creep Activation Energy Calculation for Polycrystalline Alumina

From the creep rates of alumina in Chapter 6 for 1100 and 1300°C, the creep activation energy, Q , from Equation 23 can be calculated by keeping the grain size and stress constant. In order to keep the grain size and stress constant, creep rates for the same material at the same stress conditions are compared. Plotting the data in Figure A1 as the natural logarithm of strain rate versus the reciprocal of temperature, the expression $-Q/R$ from Equation 23 was determined by linear regression for each set of conditions. Therefore, the creep activation energy was calculated for silica doped and undoped alumina specimens at three different stress conditions: 100, 150, and 200 MPa.

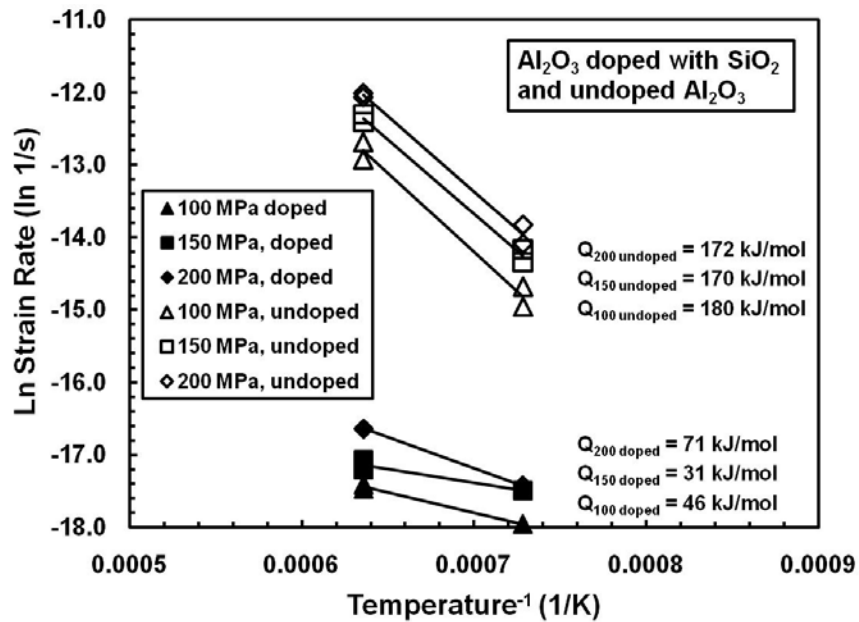


Figure A1. Natural log of strain rate vs. inverse temperature for polycrystalline alumina and silica doped polycrystalline alumina at 1100 and 1300°C

The creep activation energies calculated from Figure A1 are unreasonable low, especially for the silica doped specimens. This was the first indication that grain growth during the 1300°C creep test may have occurred. If grain growth did occur at 1300°C, then the strain rate would be lower due to the inverse relationship of strain rate and grain size, resulting in a low calculation for the creep activation energy. Furthermore, the normalized creep rates in Section 6.6 would also be biased to lower normalized strain rates since that analysis is normalizing for different grain sizes.

From the discussion in Section 6.3, abnormal grain growth for the silica doped specimens is possible at this temperature. Since the calculation of the creep activation energy requires either a constant grain size or the grain size and its dependency on creep rate to be accounted, the calculation above is suspected to be in error. Further investigation into the grain morphology of both the silica doped and undoped polycrystalline alumina is recommended.

Bibliography

1. *The Holy Bible: English Standard Version: The ESV Study Bible*. Wheaton, Ill.: Crossway Bibles, 2008.
2. "Ceramic Matrix Composites," in *Composite Materials Handbook*, , vol. 5, Department of Defense, 2002.
3. *3M ceramic textiles technical notebook*, 3M Ceramic Fibers and Textiles, St Paul MN, 2001.
4. *Standard test method for determination of slow crack growth parameters of advanced ceramics by constant stress-rate flexural testing at ambient temperature*, ASTM C1368, 2001.
5. *Standard test method for determination of slow crack growth parameters of advanced ceramics by constant stress-rate flexural testing at elevated temperatures*, ASTM C1465, 2000.
6. E. Arzt, M. F. Ashby and R. A. Verrall, "Interface controlled diffusional creep," *Acta Metallurgica*, vol. 31, (12), pp. 1977-1989, 1983.
7. S. I. Bae and S. Baik, "Determination of critical concentrations of silica and/or calcia for abnormal grain growth in alumina," *Journal of the American Ceramic Society*, vol. 76, (4), pp. 1065-1067, 1993.
8. S. I. Bae and S. Baik, "Sintering and grain growth of ultrapure alumina," *Journal of Materials Science*, vol. 28, (15), pp. 4197-4204, 1993.
9. G. K. Bansal and W. H. Duckworth, "Effects of moisture-assisted slow crack growth on ceramic strength," *Journal of Materials Science*, vol. 13, (2), pp. 239-242, 1978.
10. M. H. BERGER and A. R. BUNSELL, "Oxide Fibers," in *Comprehensive Composite Materials*, Anthony Kelly and Carl Zweben, Eds. Oxford: Pergamon, 2000.
11. G. Bernard-Granger, C. Guizard and R. Duclos, "Compressive creep behavior in air of a slightly porous as-sintered polycrystalline α -alumina material," *Journal of Materials Science*, vol. 42, (8), pp. 2807-2819, 2007.
12. A. R. Bunsell and M. H. Berger, "Fine diameter ceramic fibres," *Journal of the European Ceramic Society*, vol. 20, (13), pp. 2249-2260, 2000.

13. V. Calard and J. Lamon, "Failure of fiber bundles," *Composites Science and Technology*, vol. 64, (5), pp. 701-710, 2004.
14. C. X. Campbell, E. V. Carelli, K. L. More, P. Varghese, S. Seal and V. H. Desai, *Effect of high-temperature water vapor exposure on nextel 720 in an alumina-matrix CMC*, TP-02076, Siemens Westinghouse Library, Siemens Westinghouse Power Corporation.
15. R. M. Cannon, W. H. Rhodes and A. H. Heuer, "Plastic deformation of fine-grained alumina (Al_2O_3). I. Interface-controlled diffusional creep," *Journal of the American Ceramic Society*, vol. 63, (1), pp. 46-53, 1980.
16. W. R. Cannon and T. G. Langdon, "Creep of ceramics. II. An examination of flow mechanisms," *Journal of Materials Science*, vol. 23, (1), pp. 1-20, 1988.
17. W. R. Cannon and T. G. Langdon, "Creep of ceramics. I. Mechanical characteristics," *Journal of Materials Science*, vol. 18, (1), pp. 1-50, 1983.
18. H. C. Cao, B. J. Dalgleish, C. H. Hsueh and A. G. Evans, "High-temperature stress corrosion cracking in ceramics," *Journal of the American Ceramic Society*, vol. 70, (4), pp. 257-264, 1987.
19. J. Castaing, A. K. Kronenberg, S. H. Kirby and T. E. Mitchell, "Hydrogen defects in $\alpha\text{-Al}_2\text{O}_3$ and water weakening of sapphire and alumina ceramics between 600 and 1000°C. II. Mechanical properties," *Acta Materialia*, vol. 48, (7), pp. 1495-1504, 2000.
20. S. R. Choi and J. P. Gyekenyesi, "Fatigue strength as a function of preloading in dynamic fatigue testing of glass and ceramics," *Journal of Engineering for Gas Turbines & Power*, vol. 119, (3), pp. 493, 1997.
21. S. R. Choi, N. P. Bansal and M. J. Verrilli, "Delayed failure of ceramic matrix composites in tension at elevated temperatures," *Journal of the European Ceramic Society*, vol. 25, (9), pp. 1629-1636, 2005.
22. S. R. Choi and J. P. Gyekenyesi, "Load-rate dependency of ultimate tensile strength in ceramic matrix composites at elevated temperatures," *Int. J. Fatigue*, vol. 27, (5), pp. 503-510, 2005.
23. A. H. Chokshi, "Diffusion creep in oxide ceramics," *Journal of the European Ceramic Society*, vol. 22, (14), pp. 2469-2478, 2002.
24. A. H. Chokshi and T. G. Langdon, "Characteristics of creep deformation in ceramics," *Materials Science and Technology*, vol. 7, (7), pp. 577-584, 1991.

25. A. H. Chokshi, A. K. Mukherjee and T. G. Langdon, "Superplasticity in advanced materials," *Materials Science & Engineering R: Reports*, vol. R10, (6), pp. 237-274, 1993.
26. H. R. Clauser, "Advanced composite materials," *Scientific American*, vol. 229, (1), pp. 36-44, 1973.
27. C. G. Cofer and J. Economy, "Oxidative and hydrolytic stability of boron nitride-a new approach to improving the oxidation resistance of carbonaceous structures," *Carbon*, vol. 33, (4), pp. 389-395, 1995.
28. B. D. Coleman, "On the strength of classical fibres and fibre bundles," *Journal of the Mechanics and Physics of Solids*, vol. 7, pp. 60, 1958.
29. G. S. Corman, *Creep of oxide single crystals*, Final Technical Report No. WRDC-TR-90-4059, U.S. Air Force Contract No. F33615-87-C-5345, 1990.
30. K. G. Dassios, M. Steen and C. Filiou, "Mechanical properties of alumina Nextel™ 720 fibres at room and elevated temperatures: tensile bundle testing," *Materials Science and Engineering A*, vol. 349, (1-2), pp. 63-72, 2003.
31. J. B. Davis, J. P. A. Lofvander, A. G. Evans, E. Bischoff and M. L. Emiliani, "Fiber coating concepts for brittle-matrix composites," *Journal of the American Ceramic Society*, vol. 76, (5), pp. 1249-1257, 1993.
32. F. Deléglise, M. H. Berger and A. R. Bunsell, "Microstructural evolution under load and high temperature deformation mechanisms of a mullite/alumina fibre," *Journal of the European Ceramic Society*, vol. 22, (9-10), pp. 1501-1512, 2002.
33. F. Deléglise, M. H. Berger, D. Jeulin and A. R. Bunsell, "Microstructural stability and room temperature mechanical properties of the Nextel 720 fibre," *Journal of the European Ceramic Society*, vol. 21, (5), pp. 569-580, 2001.
34. J. A. DiCarlo, "Property goals and test methods for high temperature ceramic fibre reinforcement," *Ceramics International*, vol. 23, (4), pp. 283-289, 1997.
35. J. A. DiCarlo and H. M. Yun, "Fiber Test Development for Ceramic Composite Thermomechanical Properties," in , vol. Mechanical, Thermal, and Environmental Testing and Performance of Ceramic Composites and Components, ASTM STP 1392, M. G. Jenkins, E. Lara-Curzio and S. T. Gonczy, Eds. West Conshohocken, PA,: American Society for Testing and Materials, 2000.
36. J. A. DiCarlo and H. M. Yun, *Factors controlling stress rupture of fiber-reinforced ceramic composites*, NASA no. 20000012406, NASA Center for Aerospace Information, Hanover, Maryland, 1999.

37. T. J. Dunyak, D. R. Chang and M. L. Millard, "Thermal aging effects on oxide/oxide ceramic-matrix composites," in *Proceedings of 17th Conference on Metal Matrix, Carbon, and Ceramic Matrix Composites. NASA Conference Publication 3235, Part 2*, pp. 675, 1993.
38. A. G. Evans, "Slow crack growth in brittle materials under dynamic loading conditions," *International Journal of Fracture*, vol. 10, (2), pp. 251-259, 1974.
39. A. G. Evans and H. Johnson, "The fracture stress and its dependence on slow crack growth," *Journal of Materials Science*, vol. 10, (2), pp. 214-222, 1975.
40. A. G. Evans and F. W. Zok, "The physics and mechanics of fibre-reinforced brittle matrix composites," *Journal of Materials Science*, vol. 29, (15), pp. 3857-3896, 1994.
41. M. K. Ferber, H. T. Lin and J. Keiser, "Oxidation behavior of non-oxide ceramics in a high-pressure, high-temperature steam environment," *ASTM Spec. Tech. Publ.*, (1392), pp. 201-215, 2001.
42. M. K. Ferber and M. G. Jenkins, "Evaluation of the Strength and Creep-Fatigue Behavior of Hot Isostatically Pressed Silicon Nitride," *J Am Ceram Soc*, vol. 75, (9), pp. 2453-2462, 1992.
43. J. D. French, J. Zhao, M. P. Harmer, H. M. Chan and G. A. Miller, "Creep of duplex microstructures," *Journal of the American Ceramic Society*, vol. 77, (11), pp. 2857-2865, 1994.
44. M. Fritsch, H. Klemm, M. Herrmann and B. Schenk, "Corrosion of selected ceramic materials in hot gas environment," *Journal of the European Ceramic Society*, vol. 26, (16), pp. 3557-3565, 2006.
45. R. Gadow, "Ceramic layer composites in advanced automotive engineering and biomedical applications," *Key Engineering Materials*, vol. 333, pp. 177-194, 2007.
46. J. Goering and H. Schneider, "Creep and subcritical crack growth of Nextel 720 alumino silicate fibers as received and after heat treatment at 1300 C," *Ceram. Eng. Sci. Proc.*, vol. 18, (3), pp. 95-102, 1997.
47. D. J. Green, *An Introduction to the Mechanical Properties of Ceramics*. Cambridge University Press, 1998.
48. H. G. Halverson and W. A. Curtin, "Stress Rupture in Ceramic-Matrix Composites: Theory and Experiment," *J Am Ceram Soc*, vol. 85, (6), pp. 1350-1365, 2002.

49. V. H. Hammond, *Creep Rupture of an Oxide/Oxide Composite Fiber*. PhD Dissertation. University of Virginia, 2001.
50. V. H. Hammond and D. M. Elzey, "Comparing the creep response of alumina tows and single filaments," *Scripta Materialia*, vol. 46, (4), pp. 287-291, 2002.
51. R. S. Hay, E. E. Boakye, M. D. Petry, K. Von Lehmden and J. Welch, "Grain growth and tensile strength of 3M Nextel 720TM after thermal exposure," *Ceramic Engineering and Science Proceedings*, vol. 20, (3), pp. 153-163, 1999.
52. J. A. Haynes, M. J. Lance, K. M. Cooley, M. K. Ferber, R. A. Lowden and D. P. Stinton, "CVD mullite coatings in high-temperature, high-pressure air-H₂O," *Journal of the American Ceramic Society*, vol. 83, (3), pp. 657-659, 2000.
53. A. G. Hegedus, "Ceramic bodies of controlled porosity and process for making same," U.S. Pat. No 50177522, May 21, 1991.
54. C. T. Herakovich, *Mechanics of Fibrous Composites*. New York: John Wiley & Sons, 1998.
55. E. E. Hermes and R. J. Kerans, "Degradation of non-oxide reinforcement and oxide matrix composites," in *Materials Stability and Environmental Degradation; Proceedings of the Symposium*, 1988.
56. A. H. Heuer, "The role of MgO in the sintering of alumina," *Journal of the American Ceramic Society*, vol. 62, (5), pp. 317-318, 1979.
57. A. H. Heuer and K. P. D. Lagerlof, "Oxygen self-diffusion in corundum (alpha-Al₂O₃): a conundrum," *Philosophical Magazine Letters*, vol. 79, (8), pp. 619-627, 1999.
58. S. H. Hong and D. Y. Kim, "Effect of Liquid Content on the Abnormal Grain Growth of Alumina," *J Am Ceram Soc*, vol. 84, (7), pp. 1597, 2001.
59. Hua-Tay Lin and P. F. Becher, "Creep behavior of a SiC-whisker-reinforced alumina," *Journal of the American Ceramic Society*, vol. 73, (5), pp. 1378-1381, 1990.
60. T. Ishikawa, "Advances in Inorganic Fibers," *Polymeric and Inorganic Fibers*, vol. 178, 2005.
61. N. Jacobson, S. Farmer, A. Moore and H. Sayir, "High-temperature oxidation of boron nitride. I. Monolithic boron nitride," *Journal of the American Ceramic Society*, vol. 82, (2), pp. 393-398, 1999.

62. N. S. Jacobson, "Corrosion of silicon-based ceramics in combustion environments," *Journal of the American Ceramic Society*, vol. 76, (1), pp. 3-28, 1993.
63. N. S. Jacobson, G. N. Morscher, D. R. Bryant and R. E. Tressler, "High-temperature oxidation of boron nitride. II. Boron nitride layers in composites," *Journal of the American Ceramic Society*, vol. 82, (6), pp. 1473-1482, 1999.
64. M. Jimenez-Melendo, H. Haneda and H. Nozawa, "Ytterbium Cation Diffusion in Yttrium Aluminum Garnet (YAG)--Implications for Creep Mechanisms," *J Am Ceram Soc*, vol. 84, (10), pp. 2356, 2001.
65. F. A. Kandil, "Tensile Creep of Ceramics: the Development of a Testing Facility," *Int.J.High Technol.Ceram*, vol. 4, (2-4), pp. 243, 1988.
66. K. A. Keller, G. J. Jefferson and R. J. Kerans, "Oxide-Oxide Composites," in *Handbook of Ceramic Composites*, N. P. Bansal, Ed. Kluwer Academic Publishers, 2005.
67. K. A. Keller, T. Mah and T. A. Parthasarathy, "Processing and Mechanical Properties of Polycrystalline $Y_3Al_5O_{12}$ (Yttrium Aluminum Garnet)," *Ceram. Eng. Sci. Proc.*, vol. 11, pp. 1122-1133, 1990.
68. R. J. Kerans, R. S. Hay, N. J. Pagano and T. A. Parthasarathy, "The role of the fiber-matrix interface in ceramic composites," *American Ceramic Society Bulletin*, vol. 68, (2), pp. 429-442, 1989.
69. R. J. Kerans, R. S. Hay and T. A. Parthasarathy, "Structural ceramic composites," *Current Opinion in Solid State and Materials Science*, vol. 4, (5), pp. 445-451, 1999.
70. R. J. Kerans, R. S. Hay, T. A. Parthasarathy and M. K. Cinibulk, "Interface Design for Oxidation-Resistant Ceramic Composites," *J Am Ceram Soc*, vol. 85, (11), pp. 2599, 2002.
71. R. J. Kerans and T. A. Parthasarathy, "Crack deflection in ceramic composites and fiber coating design criteria," *Composites Part A (Applied Science and Manufacturing)*, vol. 30A, (4), pp. 521-524, 1999.
72. H. Klemm, M. Fritsch and B. Schenk, "Corrosion of ceramic materials in hot gas environment," *Ceramic Engineering and Science Proceedings*, vol. 25, (4), pp. 463-468, 2004.

73. S. L. Korinek and J. Castaing, "Slip and twinning in polycrystalline alumina (α - Al_2O_3) deformed under hydrostatic pressure between 600° and 1000°C," *Journal of the American Ceramic Society*, vol. 86, (4), pp. 566-573, 2003.
74. A. K. Kronenberg, J. Castaing, T. E. Mitchell and S. H. Kirby, "Hydrogen defects in α - Al_2O_3 and water weakening of sapphire and alumina ceramics between 600 and 1000°C. I. Infrared characterization of defects," *Acta Materialia*, vol. 48, (7), pp. 1481-1494, 2000.
75. J. J. Kruzic, R. M. Cannon and R. O. Ritchie, "Effects of moisture on grain-boundary strength, fracture, and fatigue properties of alumina," *J Am Ceram Soc*, vol. 88, (8), pp. 2236-2245, 2005.
76. F. F. Lange, W. C. Tu and A. G. Evans, "Processing of damage-tolerant, oxidation-resistant ceramic matrix composites by a precursor infiltration and pyrolysis method," *Materials Science & Engineering A (Structural Materials: Properties, Microstructure and Processing)*, vol. A195, pp. 145-150, 1995.
77. V. Lavaste, J. Besson, M. - . Berger and A. R. Bunsell, "Elastic and creep properties of alumina-based single fibers," *Journal of the American Ceramic Society*, vol. 78, (11), pp. 3081-3087, 1995.
78. B. R. Lawn, *Fracture of Brittle Solids*. 2nd ed. Cambridge University Press, 1993.
79. H. D. Lee, T. I. Mah, T. A. Parthasarathy and K. A. Keller, "YAG lasing systems and methods," US7566408, 2007.
80. H. D. Lee, T. I. Mah, T. A. Parthasarathy and K. A. Keller, "Yttrium aluminum garnet powders and processing," US7022262, 2006.
81. C. G. Levi, J. Y. Yang, B. J. Dalgleish, F. W. Zok and A. G. Evans, "Processing and performance of an all-oxide ceramic composite," *J Am Ceram Soc*, vol. 81, (8), pp. 2077-2086, 1998.
82. M. H. Lewis, M. G. Cain, P. Doleman, A. G. Razzell and J. Gent, "Development of interfaces in oxide and silicate matrix composites," in *Proceedings of the 1995 2nd International Conference on High-Temperature Ceramic-Matrix Composites*, pp. 41, 1995.
83. T. J. Lu, "Crack branching in all-oxide ceramic composites," *Journal of the American Ceramic Society*, vol. 79, (1), pp. 266-274, 1996.
84. R. Lundberg and L. Eckerbom, "Design and processing of all-oxide composites," in *Proceedings of the 1995 2nd International Conference on High-Temperature Ceramic-Matrix Composite*, pp. 95-95, 1995.

85. T. J. Mackin, J. Y. Yang, C. G. Levi and A. G. Evans, "Environmentally compatible double coating concepts for sapphire fiber-reinforced γ -TiAl," *Materials Science & Engineering A (Structural Materials: Properties, Microstructure and Processing)*, vol. A161, (2), pp. 285-293, 1993.
86. I. MacLaren, R. M. Cannon, M. A. Gülgün, R. Voytovych, N. Popescu-Pogrión, C. Scheu, U. Täffner and M. Rühle, "Abnormal Grain Growth in Alumina: Synergistic Effects of Yttria and Silica," *J Am Ceram Soc*, vol. 86, (4), pp. 650, 2003.
87. T. Mah, N. L. Hecht, D. E. McCullum, J. R. Hoenigman, H. M. Kim, A. P. Katz and H. A. Lipsitt, "Thermal stability of SiC fibres (Nicalon)," *Journal of Materials Science*, vol. 19, (4), pp. 1191-1201, 1984.
88. T. Matsuda, "Stability to moisture for chemically vapour-deposited boron nitride," *Journal of Materials Science*, vol. 24, (7), pp. 2353-2357, 1989.
89. M. A. Mattoni, J. Y. Yang, C. G. Levi, F. W. Zok and L. P. Zawada, "Effects of combustor rig exposure on a porous-matrix oxide composite," *International Journal of Applied Ceramic Technology*, vol. 2, (2), pp. 133-140, 2005.
90. J. M. Mehrman, M. B. Ruggles-Wrenn and S. S. Baek, "Influence of hold times on the elevated-temperature fatigue behavior of an oxide-oxide ceramic composite in air and in steam environment," *Composites Science & Technology*, vol. 67, (7), pp. 1425-1438, 2007.
91. M. N. Menon, H. T. Fang, D. C. Wu, M. G. Jenkins and M. K. Ferber, "Creep and Stress Rupture Behavior of an Advanced Silicon Nitride: Part III, Stress Rupture and the Monkman-Grant Relationship," *J Am Ceram Soc*, vol. 77, (5), pp. 1235-1241, 1994.
92. C. Milz, J. Goering and H. Schneider, "Mechanical and microstructural properties of NextelTM 720 relating to its suitability for high temperature application in CMCs," *Ceram. Eng. Sci. Proc.*, vol. 20, (3), pp. 191-198, 1999.
93. H. H. Moeller, "Tensile testing of ceramic fiber tows," *Ceram. Eng. Sci. Proc.*, vol. 6, pp. 558, 1985.
94. F. C. Monkman and N. J. Grant, *An empirical relationship between rupture life and minimum creep rate in creep-rupture tests*, ASTM Special Technical Publication No. 56, Philadelphia, 1956.
95. E. H. Moore, T. Mah and K. A. Keller, "3-D composite fabrication through matrix slurry pressure infiltration," *Ceram. Eng. Sci. Proc.*, vol. 15, (4), pp. 113-120, 1994.

96. K. L. More, P. F. Tortorelli, M. K. Ferber and J. R. Keiser, "Observations of accelerated silicon carbide recession by oxidation at high water-vapor pressures," *Journal of the American Ceramic Society*, vol. 83, (1), pp. 211-213, 2000.
97. K. L. More, P. F. Tortorelli, H. T. Lin, E. Lara-Curzio, R. A. Lowden, P. Y. Hou, M. J. McNallan, R. Oltra, E. J. Opila and D. A. Shores, "Degradation mechanisms of BN interfaces in SiC/SiC composites in oxygen- and water-containing environments," in *Proceedings of the Symposium on High Temperature Corrosion and Materials Chemistry*, 1998.
98. K. L. More and P. F. Tortorelli, "Exposure of Ceramics and Ceramic Matrix Composites in Simulated and Actual Combustor Environments," *Journal of Engineering for Gas Turbines & Power*, vol. 122, (2), pp. 212, 2000.
99. P. E. D. Morgan and D. B. Marshall, "Ceramic composites of monazite and alumina," *Journal of the American Ceramic Society*, vol. 78, (6), pp. 1553-1563, 1995.
100. R. M. Morrell, "A tensile creep-testing apparatus for ceramic materials using simple knife-edge universal joints," *Journal of Physics E (Scientific Instruments)*, vol. 5, (5), pp. 465-467, 1972.
101. G. N. Morscher, D. R. Bryant and R. E. Tressler, "Environmental durability of BN-based interphases (for SiC/SiC/ composites) in H₂O containing atmospheres at intermediate temperatures," *Ceram. Eng. Sci. Proc.*, vol. 18, (3), pp. 525-534, 1997.
102. G. N. Morscher, K. C. Chen and K. S. Mazdiasni, "Creep-resistance of developmental polycrystalline yttrium-aluminum garnet fibers," *Ceram. Eng. Sci. Proc.*, vol. 15, (4), pp. 181-188, 1994.
103. E. Mouchon and P. Colomban, "Oxide ceramic matrix/oxide fibre woven fabric composites exhibiting dissipative fracture behaviour," *Composites*, vol. 26, (3), pp. 175-182, 1995.
104. R. Naslain, "Design, preparation and properties of non-oxide CMCs for application in engines and nuclear reactors: an overview," *Composites Science and Technology*, vol. 64, (2), pp. 155-170, 2004.
105. R. Naslain, "Ceramic Matrix Composites," in *European White Book on Fundamental Research in Materials Science*, Max-Planck-Institut für Metallforschung, Stuttgart, Germany, 2001.
106. C. F. Nims, "Bricks Without Straw," *The Biblical Archaeologist*, vol. 13, pp. 22, 1950.

107. K. Oda and T. Yoshio, "Hydrothermal corrosion of alumina ceramics," *Journal of the American Ceramic Society*, vol. 80, (12), pp. 3233-3236, 1997.
108. L. U. Ogbuji, "Degradation of SiC/BN/SiC composite in the burner rig," *Ceram. Eng. Sci. Proc.*, vol. 19, (4), pp. 257-264, 1998.
109. L. U. Ogbuji, "Pervasive mode of oxidative degradation in a SiC-SiC composite," *J Am Ceram Soc*, vol. 81, (11), pp. 2777-2784, 1998.
110. E. J. Opila, "Variation of the oxidation rate of silicon carbide with water-vapor pressure," *Journal of the American Ceramic Society*, vol. 82, (3), pp. 625-636, 1999.
111. E. J. Opila, "Oxidation kinetics of chemically vapor-deposited silicon carbide in wet oxygen," *Journal of the American Ceramic Society*, vol. 77, (3), pp. 730-736, 1994.
112. E. J. Opila and R. E. Hann J., "Paralinear oxidation of CVD SiC in water vapor," *Journal of the American Ceramic Society*, vol. 80, (1), pp. 197-205, 1997.
113. M. Parlier and M. H. Ritti, "State of the art and perspectives for oxide/oxide composites," *Aerospace Science and Technology*, vol. 7, (3), pp. 211-221, 2003.
114. T. A. Parthasarathy, M. K. Cinibulk and L. P. Zawada, "Combined Effect of Salt Water and High-Temperature Exposure on the Strength Retention of Nextel™720 Fibers and Nextel™720-Aluminosilicate Composites," *J Am Ceram Soc*, vol. 89, (4), pp. 1373-1379, 2006.
115. T. A. Parthasarathy, T. Mah and K. A. Keller, "Creep mechanism of polycrystalline yttrium aluminum garnet," *Journal of the American Ceramic Society*, vol. 75, (7), pp. 1756-1759, 1992.
116. T. A. Parthasarathy, L. P. Zawada, R. John, M. K. Cinibulk, R. J. Kerans and J. Zelina, "Evaluation of Oxide-Oxide Composites in a Novel Combustor Wall Application," *International Journal of Applied Ceramic Technology*, 2005.
117. M. D. Petry and Tai-II Mah, "Effect of thermal exposures on the strengths of Nextel™ 550 and 720 filaments," *Journal of the American Ceramic Society*, vol. 82, (10), pp. 2801-2807, 1999.
118. J. P. Poirier, *Creep of Crystals: High-Temperature Deformation Processes in Metals, Ceramics, and Minerals*. Cambridge University Press, 1985.

119. K. M. Prewo and J. A. Batt, "The oxidative stability of carbon fibre reinforced glass-matrix composites," *Journal of Materials Science*, vol. 23, (2), pp. 523-527, 1988.
120. J. B. Pritchard, *Ancient Near Eastern Texts Relating to the Old Testament*. 3rd ed. Princeton, N.J.: Princeton University Press, 1969.
121. R. C. Pullar, M. D. Taylor and A. K. Bhattacharya, "Effect of sodium on the creep resistance of yttrium aluminium garnet (YAG) fibres," *Journal of the European Ceramic Society*, vol. 26, (9), pp. 1577-1583, 2006.
122. R. C. Pullar, M. D. Taylor and A. K. Bhattacharya, "The sintering behaviour, mechanical properties and creep resistance of aligned polycrystalline yttrium aluminium garnet (YAG) fibres, produced from an aqueous sol-Gel precursor," *Journal of the European Ceramic Society*, vol. 19, (9), pp. 1747-1758, 1999.
123. D. J. Pysher, *Creep Rupture Behavior of Alumina-Based Ceramic Fibers*. PhD Dissertation. Pennsylvania State University, 1992.
124. D. J. Pysher and R. E. Tressler, "Creep Rupture Studies of Two Alumina-Based Ceramic Fibres," *J. Mater. Sci.*, vol. 27, (2), pp. 423-428, 1992.
125. M. B. Ruggles-Wrenn and J. C. Braun, "Effects of steam environment on creep behavior of Nextel™720/alumina ceramic composite at elevated temperature," *Materials Science and Engineering: A*, vol. 497, (1-2), pp. 101-110, 2008.
126. M. B. Ruggles-Wrenn and C. L. Genelin, "Creep of Nextel™720/alumina–mullite ceramic composite at 1200 °C in air, argon, and steam," *Composites Science and Technology*, vol. 69, (5), pp. 663-669, 2009.
127. M. B. Ruggles-Wrenn, G. Hetrick and S. S. Baek, "Effects of frequency and environment on fatigue behavior of an oxide–oxide ceramic composite at 1200°C," *Int. J. Fatigue*, vol. 30, (3), pp. 502-516, 2008.
128. M. B. Ruggles-Wrenn, P. Koutsoukos and S. Baek, "Effects of environment on creep behavior of two oxide/oxide ceramic–matrix composites at 1200 °C," *J. Mater. Sci.*, vol. 43, (20), pp. 6734-6746, 2008.
129. M. B. Ruggles-Wrenn and T. Kutsal, "Effects of steam environment on creep behavior of Nextel™720/alumina–mullite ceramic composite at elevated temperature," *Compos Part A Appl Sci Manuf*, vol. 41, (12), pp. 1807-1816, 2010.

130. M. B. Ruggles-Wrenn and P. D. Laffey, "Creep behavior in interlaminar shear of Nextel™720/alumina ceramic composite at elevated temperature in air and in steam," *Composites Science and Technology*, vol. 68, (10-11), pp. 2260-2266, 2008.
131. M. B. Ruggles-Wrenn, S. Mall, C. A. Eber and L. B. Harlan, "Effects of steam environment on high-temperature mechanical behavior of Nextel™720/alumina (N720/A) continuous fiber ceramic composite," *Composites Part A: Applied Science and Manufacturing*, vol. 37, (11), pp. 2029-2040, 2006.
132. M. B. Ruggles-Wrenn, S. S. Musil, S. Mall and K. A. Keller, "Creep behavior of Nextel™610/Monazite/Alumina composite at elevated temperatures," *Composites Science and Technology*, vol. 66, (13), pp. 2089-2099, 2006.
133. M. B. Ruggles-Wrenn, A. T. Radzicki, S. S. Baek and K. A. Keller, "Effect of loading rate on the monotonic tensile behavior and tensile strength of an oxide–oxide ceramic composite at 1200 °C," *Materials Science and Engineering: A*, vol. 492, (1-2), pp. 88-94, 2008.
134. M. B. Ruggles-Wrenn, G. T. Siegert and S. S. Baek, "Creep behavior of Nextel™720/alumina ceramic composite with $\pm 45^\circ$ fiber orientation at 1200 °C," *Composites Science and Technology*, vol. 68, (6), pp. 1588-1595, 2008.
135. M. B. Ruggles-Wrenn and N. R. Szymczak, "Effects of steam environment on compressive creep behavior of Nextel™720/Alumina ceramic composite at 1200 °C," *Composites Part A: Applied Science and Manufacturing*, vol. 39, (12), pp. 1829-1837, 2008.
136. M. B. Ruggles-Wrenn, T. Yeleser, G. E. Fair and J. B. Davis, "Effects of steam environment on creep behavior of Nextel 610/monazite/alumina composite at 1,100C," *Applied Composite Materials*, vol. 16, (6), pp. 379-392, 2009.
137. M. Schmücker and P. Mechnich, "All-oxide ceramic matrix composites with porous matrices," in *Ceramic Matrix Composites*, W. Krenkel, Ed. Wiley-VCH, 2008.
138. M. Schmücker, P. Mechnich, S. Zaefferer and H. Schneider, "Water vapor corrosion of mullite: single crystals versus polycrystalline ceramics," *Journal of the European Ceramic Society*, vol. 28, (2), pp. 425-429, 2008.
139. M. Schmücker and P. Mechnich, "Microstructural coarsening of Nextel 610 fibers embedded in alumina-based matrices," *J Am Ceram Soc*, vol. 91, (4), pp. 1306-1308, 2008.

140. M. Schmücker, H. Schneider, T. Mauer and B. Clauss, "Kinetics of mullite grain growth in aluminosilicate fibers," *Journal of the American Ceramic Society*, vol. 88, (2), pp. 488-490, 2005.
141. M. Schmücker, H. Schneider, T. Mauer and B. Clauss, "Temperature-dependent evolution of grain growth in mullite fibres," *Journal of the European Ceramic Society*, vol. 25, (14), pp. 3249-3256, 2005.
142. S. M. Sim and R. J. Kerans, "Slurry Infiltration of 3-D Woven Composites," *Ceram. Eng. Sci. Proc.*, vol. 13, (9-10), pp. 632-641, 1992.
143. A. J. Spencer, *Brick Architecture in Ancient Egypt*. Warminster, Wilts, England: Aris and Phillips, 1979.
144. A. J. Stevenson, X. Li, M. A. Martinez, J. M. Anderson, D. L. Suchy, E. R. Kupp, E. C. Dickey, K. T. Mueller and G. L. Messing, "Effect of SiO₂ on Densification and Microstructure Development in Nd:YAG Transparent Ceramics," *J Am Ceram Soc*, no. doi: 10.1111/j.1551-2916.2010.04260.x.
145. D. K. Stuart, *Exodus, the New American Commentary*. , vol. 2, Nashville, Tenn.: Broadman & Holman Publishers, 2006.
146. A. Szwed, M. L. Millard and M. G. Harrison, "Fiber-reinforced ceramic-matrix composite member and method for making," U.S. Pat. No. 5 601 674, 1997.
147. W. P. Tai, T. Watanabe and N. S. Jacobson, "High-temperature stability of alumina in argon and argon/water-vapor environments," *Journal of the American Ceramic Society*, vol. 82, (1), pp. 245-248, 1999.
148. K. Tanoue, "Grain-shape parameters for high-temperature creep resistance in powder metallurgy tungsten fine wires," *Metallurgical and Materials Transactions A*, vol. 29A, (2), pp. 519-526, 1998.
149. W. C. Tu, F. E. Lange and A. G. Evans, "Concept for a damage-tolerant ceramic composite with "strong" interfaces," *Journal of the American Ceramic Society*, vol. 79, (2), pp. 417-424, 1996.
150. M. van Roode, J. Price, J. Kimmel, N. Miriyala, D. Leroux, A. Fahme and K. Smith, "Ceramic matrix composite combustor liners: a summary of field evaluations," *Transactions of the ASME. Journal of Engineering for Gas Turbines and Power*, vol. 129, (1), pp. 21-30, 2007.
151. D. J. Vaughan, "Fiberglass Reinforcement," in *Handbook of Composites*, 2nd ed. G. Lubin and S. T. Peters, Eds. London; New York: Chapman & Hall, 1998.

152. J. B. Wachtman, *Mechanical Properties of Ceramics*. Wiley, 1996.
153. S. Wannaparhun and S. Seal, "Combined Spectroscopic and Thermodynamic Investigation of Nextel-720 Fiber/Alumina Ceramic-Matrix Composite in Air and Water Vapor at 1100°C," *J Am Ceram Soc*, vol. 86, (9), pp. 1628, 2003.
154. S. M. Wiederhorn, "Subcritical crack growth in ceramics," in *Symposium on Fracture Mechanics of Ceramics. Vol. 2*, pp. 613-646, 1974.
155. S. M. Wiederhorn, "Moisture assisted crack growth in ceramics," *International Journal of Fracture Mechanics*, vol. 4, pp. 171-177, 1968.
156. S. M. Wiederhorn, "Influence of water vapor on crack propagation in soda-lime glass," *J. Am. Ceram. Soc.*, vol. 50, pp. 407, 1967.
157. S. M. Wiederhorn and L. H. Bolz, "Stress corrosion and static fatigue of glass," *Journal of the American Ceramic Society*, vol. 53, (10), pp. 543-548, 1970.
158. B. Wilshire and D. Taylor, "Rate controlling processes during creep of ceramics," in *Science of Ceramics 14*, 1988.
159. D. M. Wilson, "New High Temperature Oxide Fibers," in *High Temperature Ceramic Matrix Composites, 4th Int. Conf. on High Temperature Ceramic Matrix Composites*, W. Krenkel and et al., Eds. Wiley-VCH, 2001.
160. D. M. Wilson, "Statistical tensile strength of Nextel™ 610 and Nextel™ 720 fibres," *Journal of Materials Science*, vol. 32, (10), pp. 2535-2542, 1997.
161. D. M. Wilson, S. L. Lieder and D. C. Lueneburg, "Microstructure and high temperature properties of Nextel 720 fibers," *Ceram. Eng. Sci. Proc.*, vol. 16, (5), pp. 1005-1014, 1995.
162. D. M. Wilson, D. C. Lueneburg and S. L. Lieder, "High temperature properties of Nextel 610 and alumina-based nanocomposite fibers," *Ceram. Eng. Sci. Proc.*, vol. 14, (7-8), pp. 609-621, 1993.
163. D. M. Wilson and L. R. Visser, "High performance oxide fibers for metal and ceramic composites," *Composites Part A: Applied Science and Manufacturing*, vol. 32, (8), pp. 1143-1153, 2001.
164. A. Xu and A. A. Solomon, "Diffusional creep and cavitation strains in high-purity alumina under tension and subsequent hydrostatic compression," *Journal of the American Ceramic Society*, vol. 75, (4), pp. 985-995, 1992.

165. H. M. Yun, J. C. Goldsby and J. A. Dicarlo, "Tensile creep and stress-rupture behavior of polymer derived SiC fibers," *NASA TM-106692*, 1994.
166. L. P. Zawada and S. S. Lee, "Evaluation of the fatigue performance of five CMCs for aerospace applications," in *Proceedings of the Sixth International Fatigue Congress*, pp. 1669-1674, 1996.
167. L. P. Zawada and S. S. Lee, "Evaluation of four CMCS for aerospace turbine engine divergent flaps and seals," *Ceram. Eng. Sci. Proc.*, vol. 16, (4), pp. 337-339, 1995.
168. L. P. Zawada and S. S. Lee, "Mechanical Behavior of CMCs for Flaps and Seals," in *DARPA Ceramic Technology Insertion Program*, W. S. Coblenz, Ed. Annapolis MD: Defence Advanced Projects Agency Conference Publication, 1994.
169. L. P. Zawada, G. Ojard, E. Bouillon, P. Spriet and C. Logan, "Evaluation of ceramic matrix composite exhaust nozzle divergent seals," in *43rd AIAA/ASME/SAE/ASEE Joint Propulsion Conference, July 8 - July 11, 2007*, pp. 880-889, 2007.
170. L. P. Zawada, J. Staehler and S. Steel, "Consequence of intermittent exposure to moisture and salt fog on the high-temperature fatigue durability of several ceramic-matrix composites," *J Am Ceram Soc*, vol. 86, (8), pp. 1282-1291, 2003.
171. F. W. Zok, "Developments in oxide fiber composites," *Journal of the American Ceramic Society*, vol. 89, (11), pp. 3309-3324, 2006.
172. F. W. Zok and C. G. Levi, "Mechanical properties of porous-matrix ceramic composites," *Advanced Engineering Materials*, vol. 3, (1), pp. 15-23, 2001.
173. J. R. Zuiker, "A model for the creep response of oxide-oxide ceramic matrix composites," in *Thermal and Mechanical Test Methods and Behavior of Continuous-Fiber Ceramic Composites; Proceedings of the Symposium, Cocoa Beach, FL; 8-9 Jan. 1996*, 1997.

REPORT DOCUMENTATION PAGE				Form Approved OMB No. 074-0188	
<p>The public reporting burden for this collection of information is estimated to average 1 hour per response, including the time for reviewing instructions, searching existing data sources, gathering and maintaining the data needed, and completing and reviewing the collection of information. Send comments regarding this burden estimate or any other aspect of the collection of information, including suggestions for reducing this burden to Department of Defense, Washington Headquarters Services, Directorate for Information Operations and Reports (0704-0188), 1215 Jefferson Davis Highway, Suite 1204, Arlington, VA 22202-4302. Respondents should be aware that notwithstanding any other provision of law, no person shall be subject to a penalty for failing to comply with a collection of information if it does not display a currently valid OMB control number.</p> <p>PLEASE DO NOT RETURN YOUR FORM TO THE ABOVE ADDRESS.</p>					
1. REPORT DATE (DD-MM-YYYY) 24-03-2011		2. REPORT TYPE Doctoral Dissertation		3. DATES COVERED (From – To) Oct 2007 – Mar 2011	
4. TITLE AND SUBTITLE Creep Performance of Oxide Ceramic Fiber Materials at Elevated Temperature in Air and in Steam				5a. CONTRACT NUMBER	
				5b. GRANT NUMBER	
				5c. PROGRAM ELEMENT NUMBER	
6. AUTHOR(S) Clinton J. Armani, Maj, USAF				5d. PROJECT NUMBER	
				5e. TASK NUMBER	
				5f. WORK UNIT NUMBER	
7. PERFORMING ORGANIZATION NAMES(S) AND ADDRESS(S) Air Force Institute of Technology Graduate School of Engineering and Management 2950 Hobson Way WPAFB OH 45433-7765				8. PERFORMING ORGANIZATION REPORT NUMBER AFIT/DS/ENY/11-02	
9. SPONSORING/MONITORING AGENCY NAME(S) AND ADDRESS(ES) Air Force Research Laboratory, Materials and Manufacturing Directorate Attn: Dr. Randall S. Hay Randall.Hay@wpafb.af.mil 937-255-9825 WPAFB OH 45433				10. SPONSOR/MONITOR'S ACRONYM(S) AFRL/RXLN	
				11. SPONSOR/MONITOR'S REPORT NUMBER(S)	
12. DISTRIBUTION/AVAILABILITY STATEMENT APPROVED FOR PUBLIC RELEASE; DISTRIBUTION UNLIMITED.					
13. SUPPLEMENTARY NOTES This material is declared a work of the U.S. Government and is not subject to copyright protection in the United States.					
14. ABSTRACT The effects of steam on the creep performance for several ceramic materials were investigated at temperatures in the 1100-1300°C range. Experimental programs were designed to explore both tensile and compressive creep behaviors as well as the response in monotonic tension. Subcritical crack growth was determined to be the dominant failure mechanism in ceramic fibers at elevated temperatures in steam. The creep life prediction analysis of ceramic fiber tows was performed using linear elastic fracture mechanics and a power-law crack velocity model. Additionally, the effects of steam at 1300°C on creep performance of high-purity polycrystalline yttrium aluminum garnet (YAG) were studied. The high temperature mechanical properties of polycrystalline YAG make it the most promising candidate material oxide material for the next generation ceramic fiber.					
15. SUBJECT TERMS Ceramic, fiber, creep, steam, Nextel™ 610, Nextel™ 720, yttrium aluminum garnet (YAG), ceramic matrix composite (CMC)					
16. SECURITY CLASSIFICATION OF:			17. LIMITATION OF ABSTRACT	18. NUMBER OF PAGES	19a. NAME OF RESPONSIBLE PERSON
REPORT	ABSTRACT	c. THIS PAGE			Marina B. Ruggles-Wrenn, PhD
U	U	U	UU	232	19b. TELEPHONE NUMBER (Include area code) (937)255-3636x4641

Standard Form 298 (Rev. 8-98)
Prescribed by ANSI Std. Z39-18